

Copyright © 1988, by the author(s).
All rights reserved.

Permission to make digital or hard copies of all or part of this work for personal or classroom use is granted without fee provided that copies are not made or distributed for profit or commercial advantage and that copies bear this notice and the full citation on the first page. To copy otherwise, to republish, to post on servers or to redistribute to lists, requires prior specific permission.

**VORTEX FORMATION AND PARTICLE TRANSPORT
IN A CROSS-FIELD PLASMA SHEATH**

by

K. Theilhaber

Memorandum No. UCB/ERL M88/21

20 March 1988

COVER PAGE

**VORTEX FORMATION AND PARTICLE TRANSPORT
IN A CROSS-FIELD PLASMA SHEATH**

by

K. Theilhaber

Memorandum No. UCB/ERL M88/21

20 March 1988

ELECTRONICS RESEARCH LABORATORY

College of Engineering
University of California, Berkeley
94720

TITLE PAGE

**VORTEX FORMATION AND PARTICLE TRANSPORT
IN A CROSS-FIELD PLASMA SHEATH**

by

K. Theilhaber

Memorandum No. UCB/ERL M88/21

20 March 1988

ELECTRONICS RESEARCH LABORATORY

College of Engineering
University of California, Berkeley
94720

Abstract

The time-dependent behavior of a transversely magnetized, two-dimensional plasma-wall sheath has been studied through particle simulations, with the aim of modelling plasma behavior in the vicinity of the limiters and walls of magnetized plasma devices. The simulations have shown that the cross-field sheath between a wall and a plasma is a turbulent boundary layer, with strong potential fluctuations and anomalous particle transport. The driving mechanism for this turbulence is the Kelvin-Helmholtz instability, which arises from the sheared particle drifts created near the wall. Provided it is replenished by an internal flux of particles, the sheath maintains itself in a dynamic equilibrium, in which the linear edge instability, the nonlinear dynamics of the particles and the outward particle diffusion all balance each other. The sheath assumes an equilibrium thickness of order $l_x \sim 5 \rho_i$, and maintains large, long-lived vortices, with amplitudes $\delta\phi \sim 2T_i/e$, which drift parallel to the wall at roughly half the ion thermal velocity. The sheath also maintains a large, spatially-averaged potential drop from the wall to the plasma, with $\Delta\phi \approx -1.5T_i/e$, in sharp distinction with the unmagnetized sheath, where the plasma potential is *higher* than at the wall. Accompanying the long-wavelength vortices is a spectrum of shorter-wavelength fluctuations, which extend to $|k| \rho_i \sim 1$ and $\omega \sim \omega_{ci}$, and which induce an anomalous cross-field transport. A central result is that the anomalous transport scales like Bohm diffusion, at least when $\omega_{pi} \geq 2\omega_{ci}$. At lower densities, $\omega_{pi} < 2\omega_{ci}$, the diffusion coefficient has an additional factor, proportional to the density. These results enable us to model the cross-field sheath by a simple boundary condition, which relates the particle flux through the sheath to the edge density and which can be used as input in any model designed to obtain the bulk plasma properties.

*This work supported by U.S. Department of Energy Contract No.FG03-86ER53220, by U.S. Office of Naval Research Contract No.N14-80-C-0507, and by a MICRO grant with a gift from the Varian Corporation.

Contents

1	Introduction	4
2	Previous Work	6
3	The Simulation Model	7
4	Transient Behavior of the Sheath	11
4.1	Evolution of the Total Number of Particles	13
4.2	Evolution of the Electrostatic Potential	14
4.3	Evolution of the Fourier Modes	21
4.4	Minimum Length for a Two-Vortex Steady-State	23
4.5	Saturation Mechanisms: Climax and Coalescence	25
4.6	Behavior when $k_{\parallel} \neq 0$	28
5	Fluid Theory	30
5.1	The Nonlinear Cross-Field Equations	31
5.2	Growth-Rates of the Kelvin-Helmholtz Instability	33
6	Steady-State Structure of the Sheath	41
6.1	Simulation Results	41
6.2	Dependence of the Sheath Thickness on System Size	47
6.3	Localized Solutions for the Steady-State Vortex	50
6.4	Periodic Solution for the Steady-State Vortex	53
6.5	Power Spectra	55
6.6	Source of the Short-Wavelength Fluctuations	60
7	Transport	63
7.1	Orbits of Test Particles	65
7.2	Dynamics without Electron Gyromotion	71
7.3	Numerical Estimates of the Diffusion Coefficient	72
7.4	Estimate of Discrete-Particle Effects	74
7.5	Analytic Estimate of the Diffusion Coefficient	75
7.6	Scaling of the Diffusion Coefficient with Density	79
8	Summary	83

9	Conclusions	86
	Acknowledgments	88
A	The One-Dimensional Sheath	89
A.1	Analytic Expressions for the Electric Field	89
A.2	Comparison with one-dimensional particle simulations . . .	94
	References	96

1 Introduction

The following is a report on the results of our particle simulations of the magnetized plasma-wall sheath. This is a study of plasma transport perpendicular to a magnetic field, in a plasma bounded by a conducting wall. The objective is to model plasma behavior in the vicinity of limiters and walls of magnetized plasma devices. Our approach has been to use our two-dimensional, bounded particle simulation code ES2[1], as a tool for the investigation of edge effects, in an idealized model which retains the essential features of the edge plasma.

Our simulations have shown that the cross-field sheath between a wall and a plasma is not a static structure, but is in fact a turbulent boundary layer, with strong potential fluctuations and anomalous particle transport. The driving mechanism for this turbulence is the Kelvin-Helmholtz instability which arises from the sheared particle drifts created near the wall by the strongly non-neutral sheath. Provided it is replenished by an internal flux of particles, coming, for instance, from a central bulk plasma or from a diffuse ionization of neutrals, the sheath will maintain itself in a dynamic equilibrium, in which the linear edge instability, the nonlinear dynamics of the particles and the outward particle diffusion all balance each other. It is important to emphasize that the turbulent behavior of the sheath is a completely spontaneous phenomenon, which arises from the self-consistent plasma-wall interaction, and which does not require the imposition of external fields for its sustenance.

We have found that the cross-field sheath assumes an equilibrium thickness of order $l_x \sim 5 \rho_i$, and that it maintains large, long-lived vortices, with amplitudes $\delta\phi \sim 2T_i/e$, which drift parallel to the wall at roughly half the ion thermal velocity. The sheath also maintains a large, spatially-averaged potential *drop* from the wall to the plasma, with $\Delta\phi \approx -1.5T_i/e$, in sharp distinction with the unmagnetized sheath, where the plasma potential is *higher* than at the wall. Accompanying the long-wavelength vortices is a continuous spectrum of shorter-wavelength fluctuations, which extend to $|\mathbf{k}| \rho_i \sim 1$ and $\omega \sim \omega_{ci}$, and which induce an anomalous cross-field transport of particles. A central result of this paper is that the anomalous transport in the sheath scales very much like Bohm diffusion, at least when $\omega_{pi} \geq 2\omega_{ci}$. At lower densities, such that $\omega_{pi} < 2\omega_{ci}$, the diffusion coefficient is found to have an additional factor, proportional to the density. These results enable

us to model the entire cross-field sheath by a simple boundary condition, which relates the particle flux through the sheath to the edge density. This boundary condition, which measures the sheath impedance to particle flow, is usable for any model designed to obtain the bulk plasma properties, and in which the detailed sheath dynamics are unimportant.

As an aside, we would like to briefly describe our simulations in more general terms, by using concepts of non-equilibrium thermodynamics. The vortices, which behave as convection cells, can be considered *dissipative structures*[2], into which the plasma has rearranged itself so as to maximize heat and particle fluxes to the boundaries. The vortices have formed, of course, subject to the constraints inherent in the physical system; these are energy and momentum conservation, and the physical length and time scales available to the plasma. The source of free energy which maintains these structures resides in the temperature difference between the reservoir of hot ions and electrons, which are continuously fed into the system, and the wall, which is kept at absolute zero, insofar as it is a perfect absorber of incoming particles. Our system is analogous to the configuration leading to Rayleigh-Bénard convection[3], where convection cells and enhanced transport are also driven by a temperature gradient. However, the detailed dynamics of each system, and the physics of the media considered, are, of course, very different.

The work described in this Memorandum has also been presented in [4]. A videotape of a computer animation showing some of the dynamic features of the cross-field sheath[5], including the time evolution of potential surfaces and density profiles, can be obtained from the Plasma Theory and Simulation Group.

2 Previous Work

The properties of the cross-field sheath can be understood as arising from the combination of two physical effects, the formation of a static plasma-wall sheath, and the existence of a sheared-flow instability. These effects have previously been studied in completely distinct physical situations. As both fields of study are of relevance to the present work, we shall briefly review the work which has been done in both of these hitherto separate domains.

Let us first consider static models of the sheath. The original work on unmagnetized sheaths goes back to Tonks and Langmuir[6], but the study of magnetized sheaths is more recent. Particularly close to the situation considered in the present paper are the works of Delbege and Bein[7] and Chodura[8], in which the authors have considered the magnetized sheath which forms between a wall and a plasma. However, there are crucial differences between their work and the content of the present paper: their analysis is one-dimensional, and furthermore assumes a magnetic field which is oblique, and not strictly parallel, to the wall. In this configuration, the electron dynamics are dominant, and the magnetized sheath is indeed qualitatively similar to the unmagnetized sheath.

Let us now consider the second field of study, that of shear-flow instabilities in plasmas. There is a large literature going back to the original work of Buneman[9] on the "Diocotron" instability. Somewhat more recent work includes, for instance, that which is presented in articles of Gould[10] and Knauer[11]. The plasma Kelvin-Helmholtz instability, as opposed to the one-species Diocotron instability, has been treated by Chandrasekhar[12] as an MHD instability. In the present paper however, we have especially drawn on work by Byers[13], Miura and Pritchett[14], and Pritchett and Coroniti[15]. We have also noted the work of Horton et al.[16], in which the Kelvin-Helmholtz instability is studied in a configuration with similarities to the present one. We shall discuss these similarities, as well as basic differences between their model and ours, in the summary of Section 8.

3 The Simulation Model

The physical configuration embodied in our computer simulation is an idealized model of the tangential edge conditions which might exist in a tokamak or in a variety of plasma magnetrons. We assume that the essential plasma dynamics are two-dimensional, with all motion confined to the plane perpendicular to the magnetic field, with magnetic field lines exactly tangential to the boundary. The magnetic field is homogeneous and shear-free, and the model is restricted to electrostatic, collisionless modes. These assumptions imply that in all that follows, we shall be concentrating on the behavior of flute-like electrostatic modes, with $k_{\parallel} = 0$, driven by charge separation, and localized in the edge layer. In a real device, we are focussing on a distance much smaller than the scale-length of any magnetic shear.

By focussing on flute-like modes, we are insuring that the assumption of a magnetic field strictly parallel to the wall does not correspond to a singular configuration. Rather, we are assuming that the system self-consistently selects an instability with $k_{\parallel} \approx 0$, for which the assumption of two-dimensional geometry is automatically valid.

We modelled the two-dimensional plasma-wall system outlined above with an electrostatic particle-in-cell simulation code, the computer program ES2[1]. This two-dimensional program is of the explicit type, in that it incorporates full electron and ion dynamics, and simulates plasma behavior on the time-scale of the electron gyro-period, ω_{ce}^{-1} [17].

The simulation region is shown in Fig.(1). The particles move in the (x - y) plane, in which they are subject to the external, perpendicular magnetic field B_0 , and in which they also interact with each other, according to their self-consistent electrostatic fields. Note that both particle velocities and coordinates are restricted to two components, with $\mathbf{v} = (v_x, v_y)$ and $\mathbf{x} = (x, y)$.

The simulation region is rectangular in shape, with periodic boundary conditions on the particles and fields in the direction parallel to the wall (y), with the wall defining the left-hand boundary. The wall is taken to be a perfect conductor, imposing a constant potential at $x = 0$, and is modelled as a perfect absorber of impacting electrons and ions, with no reflection or reemission of particles. When a particle hits the wall, it is lost to the inner plasma, and its charge is immediately accounted for as distributed

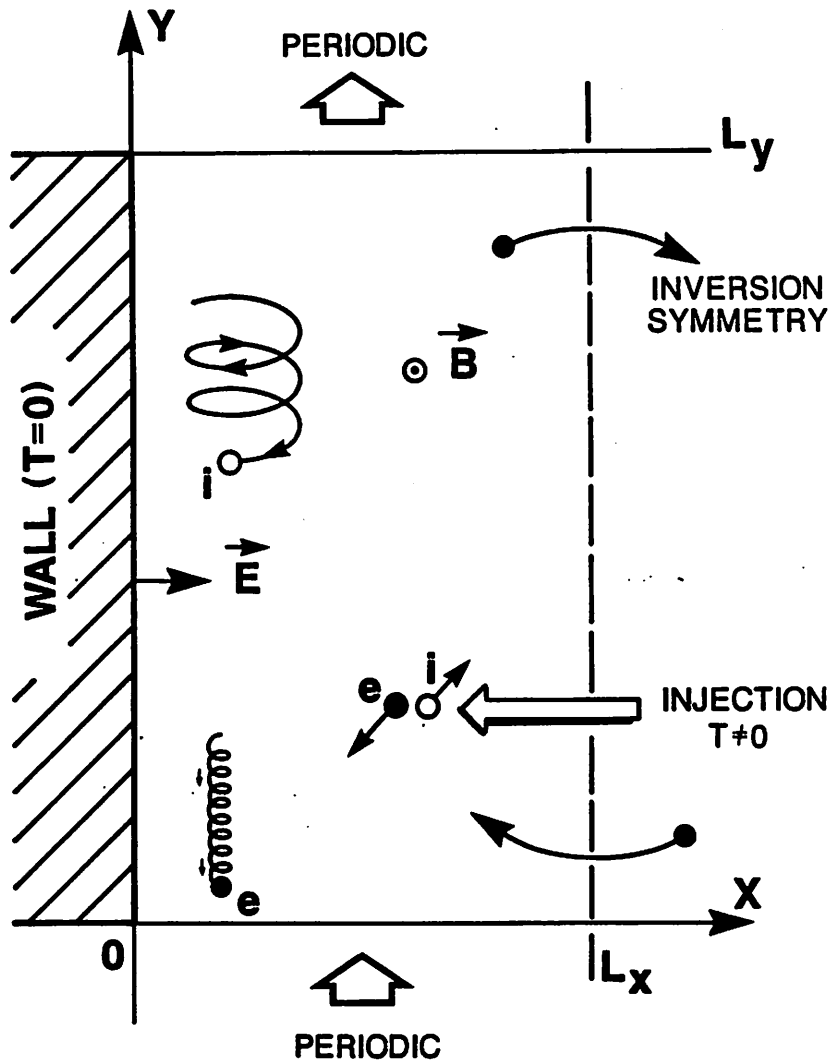


Figure 1: The ES2 simulation region.

surface charge, which in turn is a boundary source in Poisson's equation. In solving Poisson's equation, the program also automatically accounts for all charges induced on the wall by the particles moving inside the plasma. In our simulations, the wall is kept "floating"; it is not connected to an external circuit, and charge flow can occur only from the plasma to the wall.

The boundary conditions at the right-hand side of Fig.(1) are an attempt to simulate as best as possible a semi-infinite plasma in $x > L_x$. The boundary conditions are the following. For the fields, the surface at $x = L_x$ is an equipotential. For the particles, an inversion symmetry condition is imposed[18]: a particle exiting at y with velocity (v_x, v_y) is returned at $y' = L_y - y$ with inverted velocity $(-v_x, -v_y)$. Thus, the boundary at $x = L_x$ can be thought of as a very fine wire mesh which shorts-out the tangential electric fields, but which is transparent to particles. The mesh separates two plasma regions, which are exactly symmetrical through the point $(L_x, L_y/2)$, and which consist of the actual simulation plasma, and a virtual, spatially inverted "twin" plasma. This inversion-symmetry condition differs somewhat from the one outlined in [18], because the boundary at $x = L_x$ is taken to be an equipotential. We believe that this condition shields the actual simulation region from the fields in its virtual twin, and thus reduces the interference between the two regions.

In ES2, we have also modelled a distributed plasma source, with which ions and electrons are continuously created in the system. This is done by creating electron-ion pairs spatially at random, and at a constant temporal rate (a constant number of pairs is created at each time step). The electron and ion in each pair are initially created on top of each other, and are given random and uncorrelated velocities, chosen from Maxwellian distributions with $T_e = T_i$. This source of plasma can be thought of as resulting from the ionization of a uniform background of neutral atoms, and is essential in maintaining the system in a steady-state on the time-scale of the cross-field transport. Over shorter time-scales, an initial loading of warm electrons and ions with no further pair creation, is sufficient to produce the turbulent cross-field sheath, with a slow net diffusion of particles to the wall.

In Fig.(1), we have suggested the presence of an underlying heat engine, which drives the processes in the edge layer. We have done this by indicating temperatures for the wall and for the plasma source: the wall, which absorbs all incoming particles and emits none, can be thought of

as a heat sink at absolute zero; the plasma source on the other hand, is an infinite reservoir, maintained at a constant temperature $T \neq 0$. In our fictitious "heat engine", it is this temperature differential between wall and the plasma source which provides the free energy necessary for maintaining turbulent behavior in the edge layer.

Run 1: Parameters for the Initial Conditions.					
m_i/m_e	40	v_{te}	1	Δx	1
s^*	1.005	v_{ti}	0.158	Δy	1
ω_{ce}	1	ρ_e	1	Δt	1
$\bar{\omega}_{pe}$	0.2	ρ_i	6.32	N_x	33
$\bar{\omega}_{pi}$	0.032	L_x/ρ_i	5.06	N_y	256
ω_{ci}	0.025	L_y/ρ_i	40.5	$\omega_{ci}t_{max}$	~ 1500
$\bar{\omega}_{pi}/\omega_{ci}$	1.15	$\lambda_{de} = \lambda_{di}$	5	$N_e(t=0)$	15000
$\bar{\omega}_{pe}/\omega_{ce}$	0.182	$\pi\lambda_d^2$	56	$N_i(t=0)$	15000

Table 1: Parameters for Run 1.

4 Transient Behavior of the Sheath

We shall now consider the results of an ES2 particle simulation, with parameters given in Table 1. This computer run, which we shall refer to as Run 1, is the central example to be discussed in this paper. We initialized the system with a plasma uniform up to the wall, and ran the simulation with a constant creation of particles. After a fairly lengthy transient phase, the system settled into a quasi-steady-state, in which the outward transport of particles balanced the influx from the source, and in which the qualitative structure of the electrostatic fields remained the same. In the present and following sections, we shall discuss the transient phase of evolution of the plasma-wall sheath, and examine the growth and saturation of the electrostatic fields. In particular, we shall present analytic results for the linear growth of the Kelvin-Helmholtz instability, and we shall qualitatively describe the mechanisms underlying the subsequent nonlinear evolution of the system. A discussion of the steady-state, as characterized by its fields, spectra, and particle transport, is deferred to Section 5 and to the following sections.

Let us examine the conditions implied by the parameters displayed in Table 1. In Run 1, the plasma region was initially filled with $N = 15000$ particles of each species, uniformly distributed in space and initialized with Maxwellian velocity distributions with equal temperatures, $T_i = T_e$. The ion-electron mass ratio used in the simulation was $m_i/m_e = 40$. With the normalizations assumed in ES2 ($\epsilon_0 \equiv 1$, $m_e = e$), and with $e = m_e = 0.018$ and $B_0 = 1$, we have in the units of ES2 $\omega_{ce} = 1$, $\omega_{ci} = 0.025$, $v_{te} = (T_e/m_e)^{1/2} = 1$, and $v_{ti} = (T_i/m_i)^{1/2} = 0.158$. The initial particle densities were $\bar{n}_e = \bar{n}_i = N/L_x L_y = 1.83$, such that $\omega_{pe} = 0.182$ and $\omega_{pi} = 0.0287$, giving the dimensionless ratios $\omega_{pe}/\omega_{ce} = 0.182$ and $\omega_{pi}/\omega_{ci} = 1.15$. We also have the values for the gyroradii and the Debye lengths, $\rho_e = 1$, $\rho_i = 6.32$, and $\lambda_{de} = \lambda_{di} = 5.5$, so that the physical lengths satisfy $\rho_e \ll \lambda_{de} = \lambda_{di} < \rho_i$. The dimensions of individual cells on the mesh were $\Delta x = \Delta y = 1$, so that we could resolve wavelengths down to, but not including, the electron gyroradius. Our choice of the initial number of particles was such as to ensure a large number of particles per Debye square, with $\bar{n}\lambda_{de,i}^2 = 55$. This large value of the plasma parameter was needed to keep the thermal fluctuations of the system small compared to the amplitudes of the collective modes.

In Run 1, our choice of a fairly low particle density, with $\omega_{pi}/\omega_{ci} = 1.15$, enabled us to run ES2 for very long times at a reasonable computational cost, and thus to accumulate a large amount of simulation data. In Section 7.6 we shall discuss the results from simulations with higher densities, but shorter running times. However, Run 1 exhibits all the basic features of the cross-field sheath, and we use it as our central example.

The overall system size was $L_x = 32$ and $L_y = 256$, with a grid $N_x \times N_y = 33 \times 256$. Thus the system was elongated parallel to the wall, with $L_y/\rho_i = 40.5$ and $L_x/\rho_i = 5.06$. Our choice of $L_y > L_x$ was dictated by our desire to accommodate several unstable wavelengths of the initially dominant Kelvin-Helmholtz mode.

The simulation was run with a constant background creation of electron-ion pairs, at an average rate of $s_{inj} = 1.005$ pairs injected into the system per time step ($\Delta t = 1$). We can better appreciate the injection rate s_{inj} if we define a characteristic “filling-up” time, $\tau_{fill} = N/s_{inj}$: this is the time in which, without outward loss, the number of particles in the system would double. Thus, we find that for Run 1 $\omega_{ci}\tau_{fill} = 373$. In fact, the choice of s_{inj} was such that in the steady-state, the total number of

particles in the system would remain close to the initial value, a choice which was not fortuitous, but based on numerical experimentation with shorter computer runs.

4.1 Evolution of the Total Number of Particles

A global indication of the behavior of Run 1, as it evolved through the transient phase and into a quasi-steady-state, is to be seen in the time histories of the total electron and ion populations, $N_e(t)$ and $N_i(t)$. In Fig.(2), we plot $N_e(t)$ and $N_i(t)$ over the time interval $0 \leq \omega_{ci}t \leq 1500$. In this figure, a first feature to be noted is that both curves show a sudden initial drop. This sudden loss of particles results from the scrape-off of electrons and ions over a layer near the wall, comparable in thickness to the gyro-radius of each species. The electron loss ($\Delta N_e \approx -500$) occurs almost instantaneously, over a few time steps, while the more important ion loss ($\Delta N_i \approx -3500$) takes place over the longer time-span corresponding to an ion rotation, $\omega_{ci}t \approx 2\pi$. The ratio of the numbers of particles lost is roughly proportional to the depth of the scrape-off layer, with $\Delta N_i/\Delta N_e \approx \rho_i/\rho_e = 6.32$.

Immediately after this initial loss due to scrape-off, both particle populations begin to increase in response to the external source. Note that in the absence of any outward transport, the total number of particles of either species would increase roughly five-fold during the time-span of the simulation, since the filling-up time for adding 15000 particles is $\tau_{fill} = 373\omega_{ci}^{-1}$. However, this is not the case. First, the initial rates of increase of the populations are lower than the rate of injection from the source. Thus, from Fig.(2) we find that $dN_e(t \approx 0)/dt \approx dN_i(t \approx 0)/dt = 0.67$, smaller than $s_{inj} = 1.005$. Furthermore, both dN_e/dt and dN_i/dt decrease with time, with a noticeable "bend" occurring in the population curves at $\omega_{ci}t \approx 100$. After a fairly long ($0 \leq \omega_{ci}t \sim 1000$), but not very pronounced transient, the system settles into a fluctuating steady-state, with the time-averaged values of dN_e/dt and dN_i/dt near zero. In the steady-state, we have $N_e \approx 16500$ and $N_i \approx 14000$, for which the spatially-averaged densities are such that $\bar{\omega}_{pi}/\omega_{ci} \approx 1.11$ and $\bar{\omega}_{pe}/\omega_{ce} \approx 0.19$. The existence of the near steady-state in the presence of a constant source of particles is a clear indication of the existence of an equal and compensating outward transport of particles,

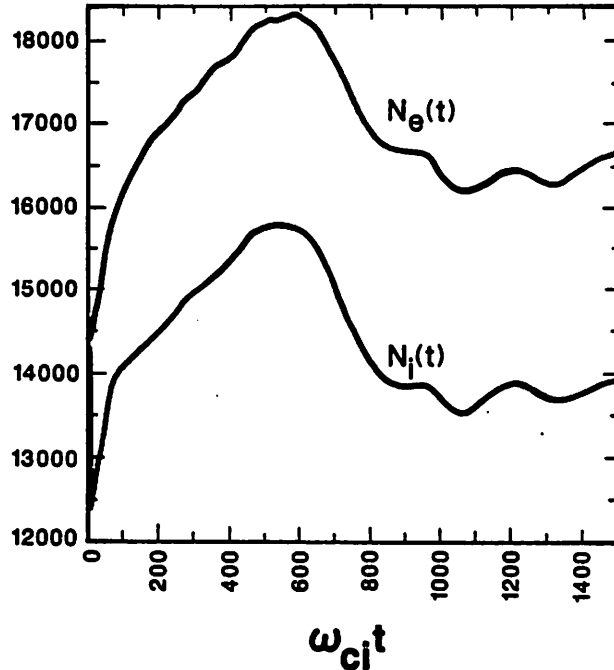


Figure 2: Evolution of the total electron and ion populations in Run 1; the initial values are $N_e(0) = N_i(0) = 15000$. The initial scrape-off of particles, where N_e drops to 14500 and N_i to 12500, occurs for $\omega_{ci}t \leq 2\pi$ and appears instantaneous on the time-scale of the figure.

from the plasma to the wall.

4.2 Evolution of the Electrostatic Potential

In this subsection, we shall discuss the evolution of the electrostatic potential over the time interval $0 \leq \omega_{ci}t \sim 1000$. This interval roughly corresponds to the transient phase of Run 1 as seen in Fig.(2).

In Figs.(3), we have displayed a series of snapshots of $\phi(x, y, t)$ taken at successive moments in time. Fig.(3a), taken at $\omega_{ci}t = 15$, shows the essentially y -uniform sheath which has formed at the beginning of the evolution of the system, after $21/2$ rotations of the ions. This sheath is due to the initial loss of ions which have impacted into the wall, resulting in a layer of depletion of positive charge over a depth of about $2 \times \rho_i \sim 12$, and a net positive charge on the wall. The result is a large potential drop from the wall into the plasma, which in Fig.(3a) is approximately $e\Delta\phi/T_i \approx -1.1$. The occurrence of a potential *drop* from wall to plasma is in sharp contrast to the situation in the unmagnetized sheath. In the latter, the equilibrium

configuration is dominated by the electron flow to the walls, and this results in a potential *rise* from the wall into the plasma.

The sheath shown in Fig.(3a) contains a non-uniform electric field $E_x(x)$ pointing into the plasma, with maximum intensity at the wall. Because of the presence of the external magnetic field, this electric field induces a downward $\mathbf{E} \times \mathbf{B}$ drift of electrons and ions parallel to the wall, with a maximum drift velocity which is very close to the ion thermal speed, $v_y(x=0) = -E_x(x=0)/B_0 \approx -v_{ti}$. Because the electric field is nonuniform, the resulting flow is strongly sheared in velocity, with a shear length of order $2 \times \rho_i$. As sheared flow is in general unstable, it might be expected that the initial structure shown in Fig.(3a) will not persist, with the flow vulnerable to the Kelvin-Helmholtz instability. This is precisely what is observed in the subsequent evolution of the potential: y -dependent ripples (which were already visible in Fig.(3a)) grow into larger perturbations, which are both amplified and convected by the $\mathbf{E} \times \mathbf{B}$ flow. This process appears to occur over a time-scale (e-folding time) which is of order $t \sim 20\omega_{ci}^{-1}$. In Fig.(3b), at $\omega_{ci}t = 62.5$, we see a state with two large and two or three smaller perturbations of the electrostatic potential, with a wavelength which we estimate to be $\lambda_y \approx 60$. A measure of the amplitudes of the perturbations is the potential drop in the cross-sections of $\phi(x,y)$ taken at $x = L_x/2$, which range from $e\delta\phi/T_i \sim -0.08$ to $e\delta\phi/T_i \sim -0.2$.

As the amplitudes of the potential perturbations seen in Fig.(3b) grow, they undergo a first saturation by forming small vortices with the same characteristic length, $\lambda_y \approx 60$. These vortices, generated in the time-span $60 \leq \omega_{ci}t \sim 200$, are short-lived because they rapidly coalesce with each other, forming a smaller number of vortices with $\lambda_y \approx 120$. There is also simultaneous competition from the mode with $\lambda_y \approx 120$, which, as we shall see in the next section, has a linear growth rate comparable to that of the $\lambda_y \approx 60$ mode. The overall effect is to favor the longer wavelength. As a result, Fig.(3c), taken at $\omega_{ci}t = 125$, shows a mixed state, in which two (coalescing) small vortices ($\lambda_y \approx 60$) coexist with a large vortex ($\lambda_y \approx 120$).

Thus, the dynamics of the system favor long wavelengths for further amplification. By $\omega_{ci}t = 250$, Fig.(3d), only two large vortices, each with $e\delta\phi/T_i \approx -1$ and $\lambda_y \approx 120$, have survived. These vortices drift parallel to the wall, in accordance with the local $\mathbf{E} \times \mathbf{B}$ drift, and can be considered quasi-stable, because they maintain a constant amplitude and survive

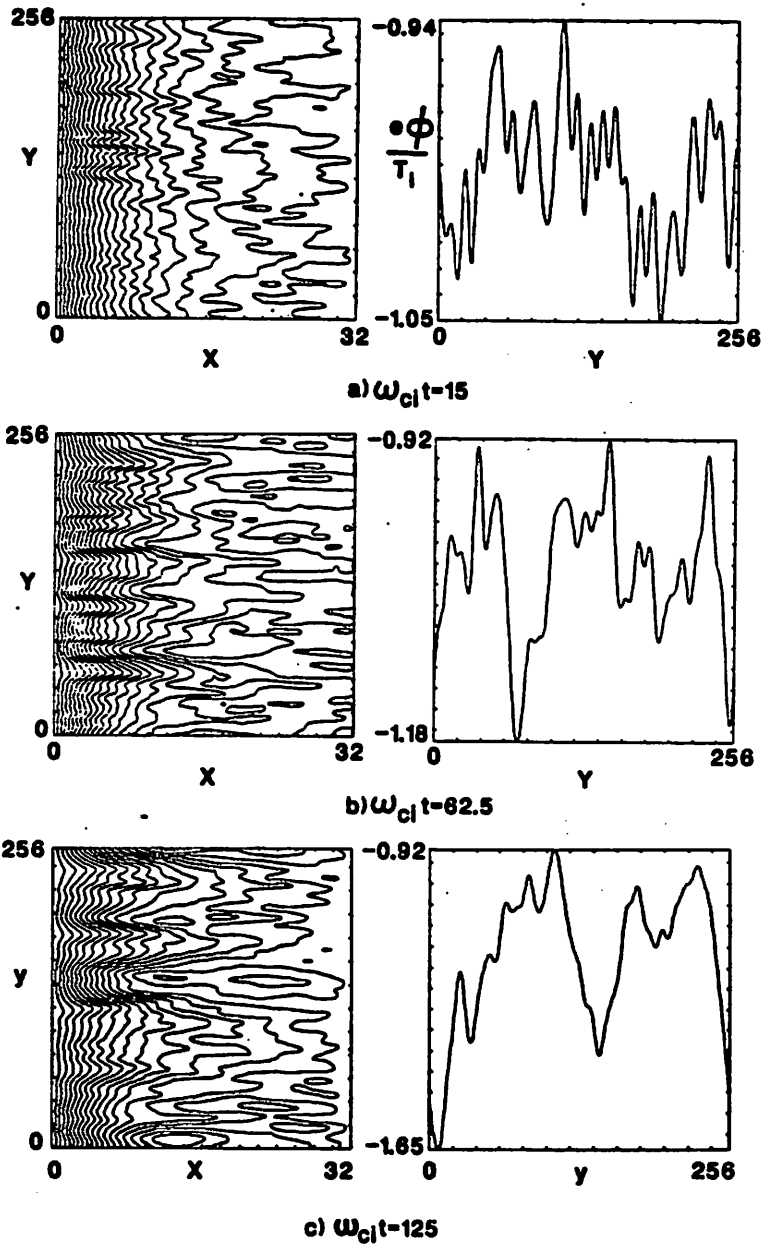


Figure 3: Snapshots of the electrostatic potential in Run 1, $0 \leq \omega_{ci}t \leq 437.5$. *Left:* contour plots of $\phi(x,y)$; *Right:* sections of $\phi(x,y)$ for constant $x = 16 = L_x/2$. Note that in the contour plots, the vertical scale is highly compressed: without the compression, the vortices will appear approximately circular (*continued on the next page*).

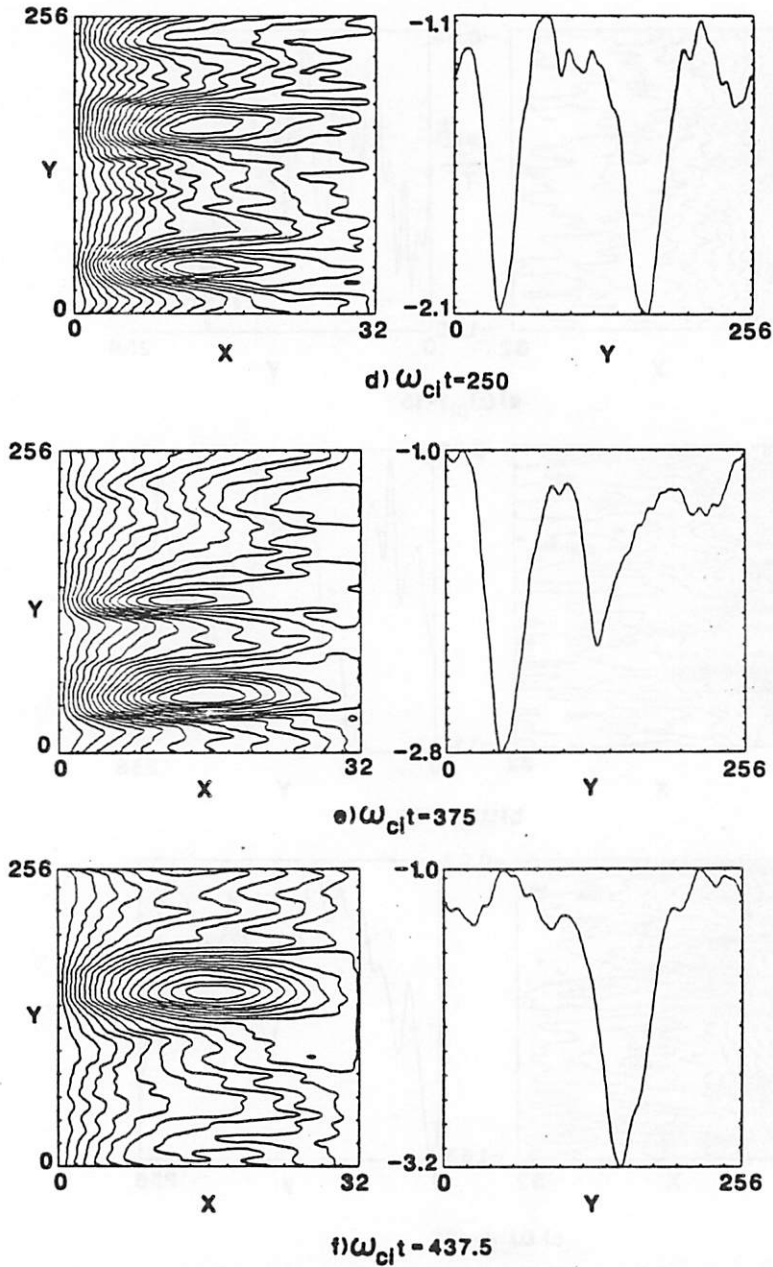


Figure 3: (continued from the previous page) Snapshots of the electrostatic potential in Run 1, $0 \leq \omega_{ci}t \leq 437.5$. *Left:* contour plots of $\phi(x, y)$; *Right:* sections of $\phi(x, y)$ for constant $x = 16 = L_x/2$. Note that in the contour plots, the vertical scale is highly compressed: without the compression, the vortices will appear approximately circular.

through several transits across the system.

Let us clarify the connection between the potential structures which we have called “vortices”, and the particle motion. If we neglect finite gyroradii, and assume that the particles move only according to the $\mathbf{E} \times \mathbf{B}$ drift of their guiding centers, with $\mathbf{v} = \mathbf{E} \times \mathbf{B}/B^2 = \hat{z} \times \nabla\phi/B$, then the electrostatic potential is strictly equivalent to a two-dimensional stream function for the particle flows (this assumption is better for the electrons, because of their small gyroradius, and approximate for the ions, because their gyroradius is a sizeable fraction of the sheath thickness). Thus, the closed contours of the potential wells tend to correspond to flows with nonzero circulation, and it is appropriate to refer to these structures as “vortices”.

The two-vortex state of Fig.(3c) is in fact only quasi-stable, and does not last beyond $\omega_{ci}t \approx 400$, because the vortices are vulnerable to the same coalescence instability which engulfed their smaller precursors. Figs.(3d,e,f) ($\omega_{ci}t = 250, 375$ and 437.5) show the progression from the state with two medium-amplitude vortices ($e\delta\phi/T_i \approx -1$) to a state with a single, large-amplitude vortex ($e\delta\phi/T_i \approx -2.2$). The process appears to occur with one vortex growing larger than the other, with the vortices then attracting each other (Fig.(3e)), and finally, with the smaller vortex merging into the larger one (Fig.(3f)).

Fig.(4), provides a more detailed view of vortex formation and coalescence than is available from the individual snapshots of Figs.(3). We have produced a time-series of cross-sections of the electrostatic potential $\phi(x, y, t)$, taken along the midplane of the simulation region, at a fixed $x = L_x/2 = 16$. These cross-sections are identical to those shown in the right-hand column of Figs.(3) and were produced by sampling the potential every 100 time steps, up to $\omega_{ci}t = 1045$. The resulting information is the two-dimensional function $\phi_{sec}(y, t)$ (x being fixed and ignorable) and in Fig.(4), we have displayed a contour plot of this function. In this form, the vortices of Figs.(3) immediately appear as valleys in the contour map of $\phi_{sec}(y, t)$. Note that as the system is periodic in y , perturbations exiting at $y = 0$ immediately reappear at $y = 256$. The structure of oblique bands in the plot make clear the steady negative drift velocity of the vortices.

In Fig.(4), the potential profile $\phi(y)$ can be determined at any one time by drawing a horizontal line through the plot. For instance, a horizontal

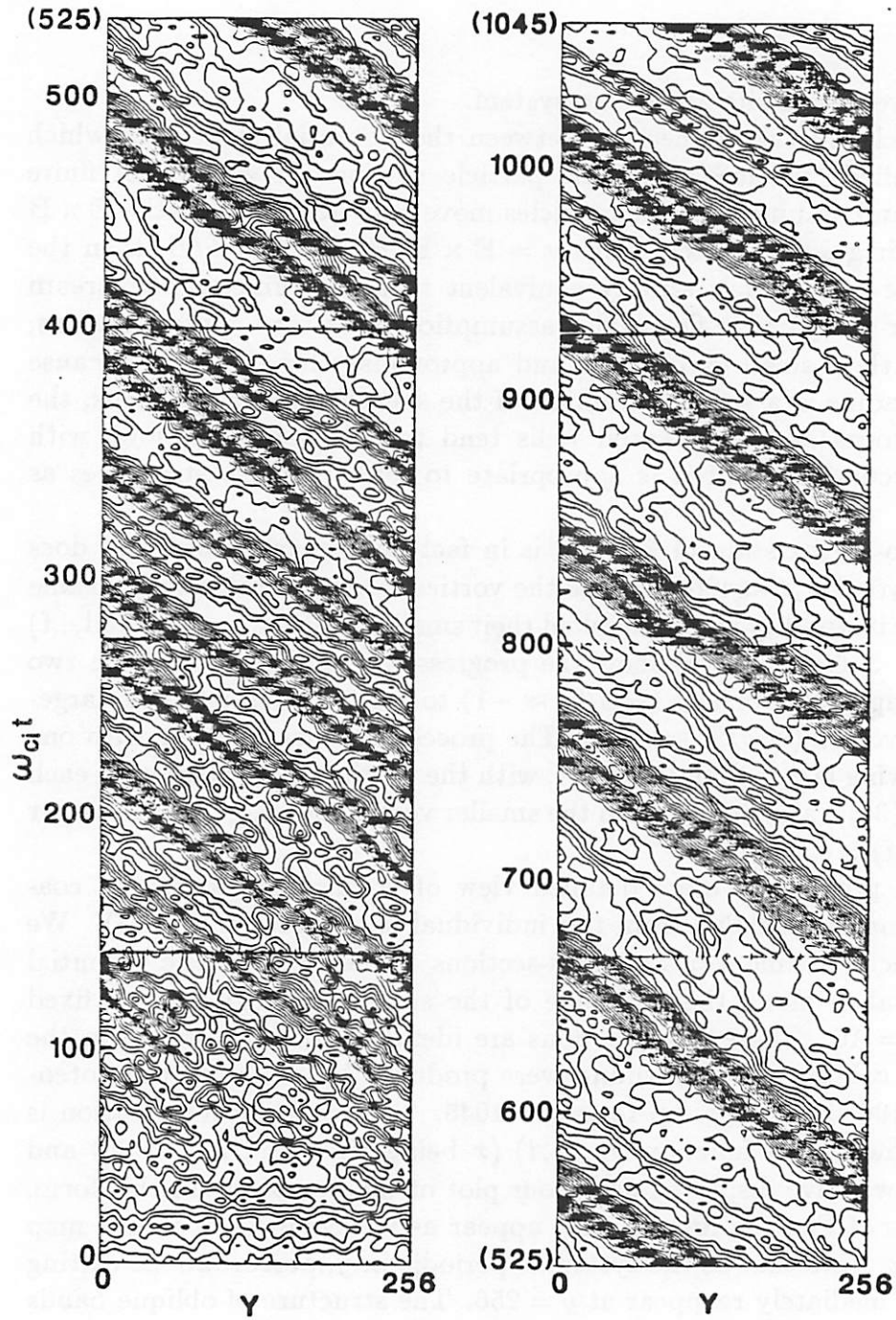


Figure 4: Contours in (y, t) space of cross-sections of $\phi_{sec}(y, t)$ of the electrostatic potentials of Figs.(3). The cross-sections are evaluated at fixed $x = L_x/2 = 16$.

line drawn at $\omega_{ci}t = 250$ intersects the tracks of two vortices, in agreement with the picture of Fig.(3d). If we now sweep this horizontal line upward, we can follow in detail the coalescence process which was only outlined in Figs.(3d-f). Near $\omega_{ci}t = 330$, the left-hand and larger vortex undergoes a slight deceleration (its y -directed velocity becomes less negative); somewhat later, at $\omega_{ci}t = 355$, the right-hand and smaller vortex undergoes a more sizeable acceleration (its y -directed velocity becomes more negative). There follows a period of “coasting”, $375 \leq \omega_{ci}t \leq 425$, where the two vortices are in close proximity. Finally, by $\omega_{ci}t = 425$, the two vortices merge together, a process in which, because of the disparity in sizes, the larger vortex appears to engulf the smaller one.

Fig.(4) provides quantitative information on the drift velocities of the vortices, the instantaneous drift velocity being equal to the reciprocal of the slope of the vortex trajectory in (y, t) space. A notable feature of these velocities is that the average vortex speed (averaged over one transit of the system) is almost constant. For instance, at $\omega_{ci}t = 150$, when the vortex amplitudes are of order $e\delta\phi/T_i \approx -0.5$, we find a vortex drift velocity $v_y = -0.069$ ($|v_y|/v_{ti} = 0.44$). At $\omega_{ci}t = 1000$, when the vortex amplitude is $e\delta\phi/T_i \approx -2$, we find a comparable drift velocity, $v_y = -0.075$ ($|v_y|/v_{ti} = 0.47$).

We also note in connection with Fig.(4) that in the final quasi-steady state, $\omega_{ci}t \geq 400$, the shear layer is still locally unstable and is capable of amplifying perturbations at some distance from the main vortex. Thus, smaller “satellite” vortices are produced. For instance, in Fig.(4) we see the appearance at $\omega_{ci}t \approx 950$ of a small vortex at a distance $l_y \approx 90$ to the left of the main vortex. At $\omega_{ci}t \approx 1020$, the satellite vortex reaches a maximum depth of $e\delta\phi/T_i \approx -0.6$, or about 1/3 the depth of the main vortex. It is eventually absorbed by the main vortex, by $\omega_{ci}t = 1050$.

Finally, we note that as the vortices grow and coalesce, the shear layer undergoes a concomitant broadening. In Figs.(5a,b), we show the profiles for the y -averaged electric field $\bar{E}_x(x)$, and for the y -averaged charge density, $\bar{\rho}(x) = \partial\bar{E}_x(x)/\partial x$, at three successive times, $\omega_{ci}t = 15, 250, 1075$. Since $v_y = -E_x/B$, Fig.(5a) is also a plot of the profile of velocity in the shear layer. Fig.(5b) shows that the inflection point x_0 of the velocity profile ($v_y''(x_0) = -\frac{1}{B}\partial\rho(x_0)/\partial x \equiv 0$) moves outward, and that the overall profiles broaden. Note that at all times the average shear profile is linearly unstable, with the inflection point and regions of opposite curvature needed

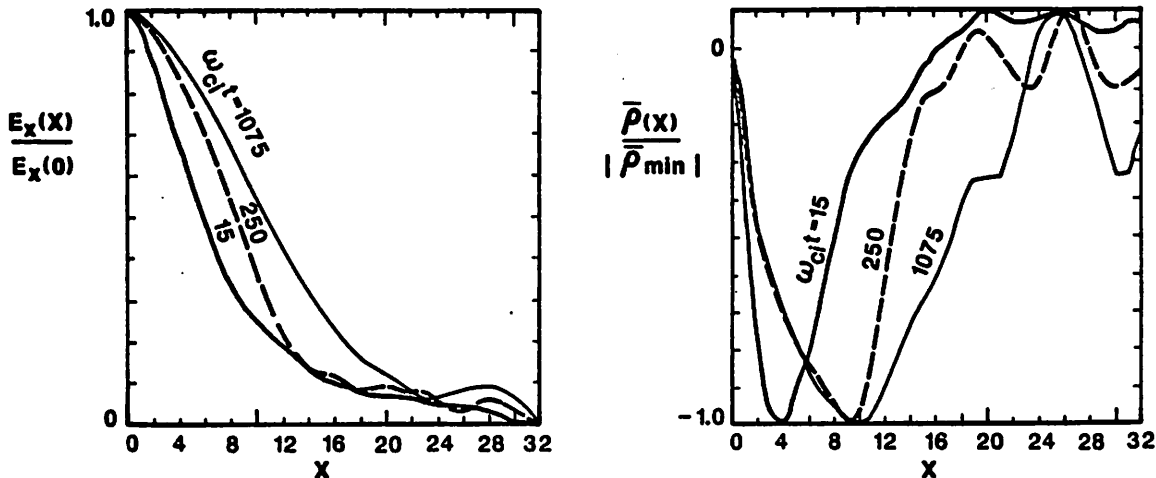


Figure 5: Cross-sections of the sheath in Run 1, for $\omega_{ci}t = 15, 250$ and 1075 ; (a) y -averaged electric field $\bar{E}_x(x)$; (b) y -averaged charge density $\bar{\rho}(x)$.

for the Kelvin-Helmholtz instability. This feature shows that the saturation mechanism is not quasilinear (relaxation of the space-averaged shear profile), but indeed strongly nonlinear.

4.3 Evolution of the Fourier Modes

We now complement the observations of the previous paragraphs, in which we identified potential structures in real (x, y) space, with a discussion of the evolution of the Fourier transform of the potential, $\tilde{\phi}(x, k_y, t)$. In Figs.(6), we show the temporal behavior of the first four Fourier modes with $k_y \neq 0$, with the Fourier transforms taken along the midplane of the system, at a fixed $x = L_x/2 = 16$. We have plotted both real and imaginary parts of $\tilde{\phi}(x, k_y, t)$. The time interval is identical to that of Fig.(4), $0 \leq \omega_{ci}t \leq 1050$.

A first salient feature of Figs.(6) is that the phase of exponential growth of any one mode is quite limited in time. A magnification of the beginning of Figs.(6) shows that, starting from noise, the exponential growth of the modes does not extend beyond roughly two e-foldings. Thus, the progression of the system toward the steady-state occurs for the most part with what appears to be algebraic growth. This behavior is consistent with the

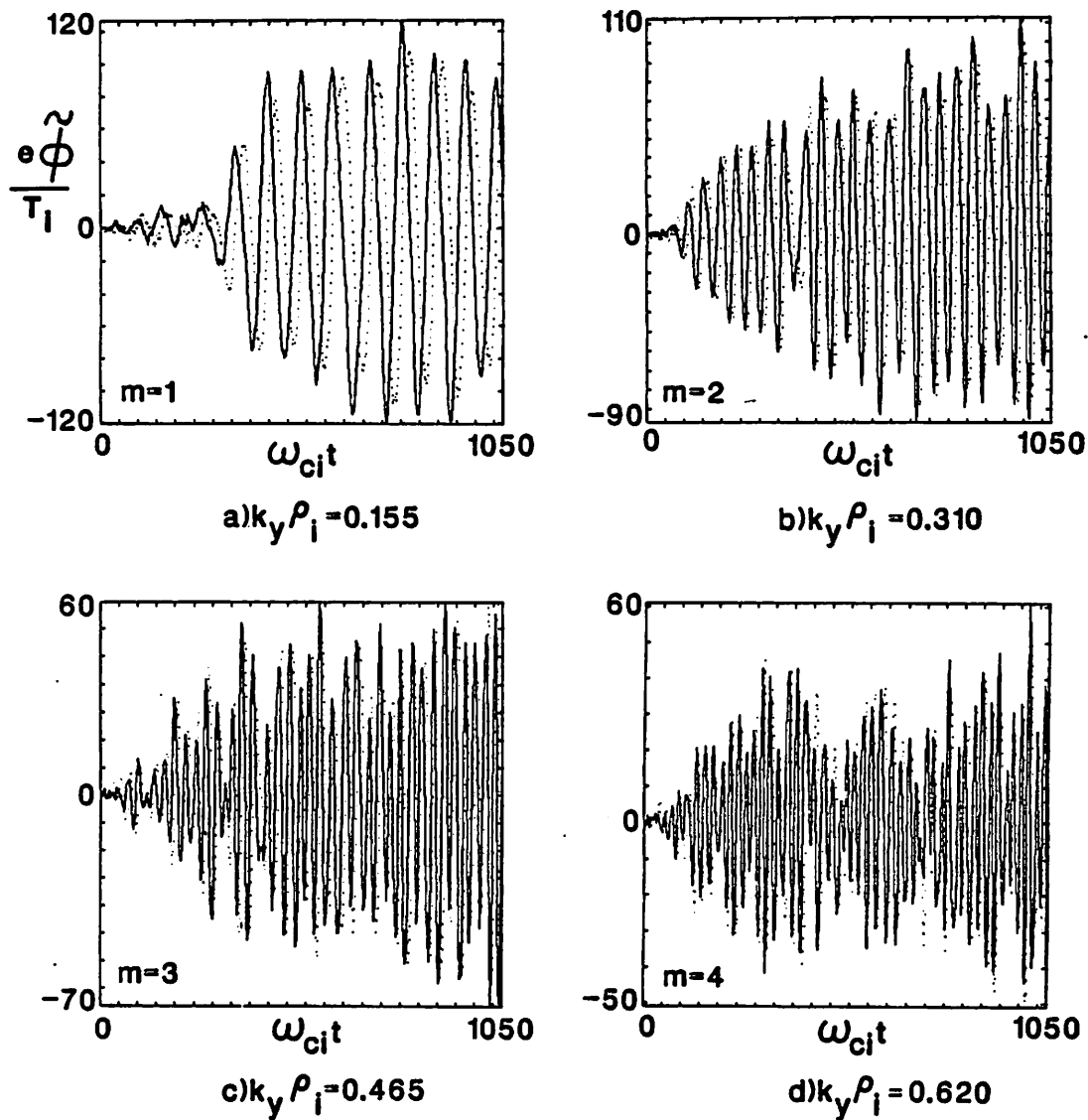


Figure 6: Temporal dependence of the Fourier modes in Run 1, modes $m = 1, 2, 3$ and 4 . The Fourier transform is taken along the midplane of the system, at a fixed $x = L_x/2 = 16$. *Solid lines*: real part; *dashed lines*: imaginary part.

description of the evolution of $\phi(x, y, t)$ given in the previous section, in which we saw that a first nonlinear state, with formation of small vortices, occurred as early as $\omega_{ci}t \approx 100$ (Fig.(3c). Beyond this point in time, the dominant mechanisms for the evolution of the instability are nonlinear, consisting of the continued, nonlinear growth of individual vortices, and of their pairwise coalescence. A qualitative analogy which comes to mind, is the nonlinear evolution of MHD tearing-modes, in which the algebraic growth and the coalescence of magnetic islands bear some resemblance to the behavior of our electrostatic vortices[19].

The coalescence of the smaller vortices into larger ones is a process indicative, in wavenumber space, of an inverse cascade. In Figs.(6a,b), we have a clear indication of the two-to-one vortex coalescence which was seen to occur in real space in the time-interval $250 \leq \omega_{ci}t \leq 437$ (Figs.(3d-f)), the two-vortex state corresponding to the $m = 2$ mode, and the one-vortex state to the $m = 1$ mode. The process begins with the sudden excitation of the fundamental mode $m = 1$, at about $\omega_{ci}t = 330$, coinciding with the beginning of spatial convergence of the two vortices which was seen in Fig.(4). The actual coalescence process, in which one vortex engulfs the other, occurs at $\omega_{ci}t \approx 400$, and is signaled by a sizeable perturbation of the $m = 2$ mode.

In Fig.(7) we show the relative amplitudes of the Fourier modes at $\omega_{ci}t = 1050$, at which time the modes have essentially settled into a quasi-steady-state. This figure shows that the first 5 or 6 modes are dominant, with the overall Fourier spectrum strongly cutoff beyond $k_y\rho_i = 1$. Finally, let us note that the short-wavelength modes not only have smaller amplitudes, but are also more strongly fluctuating, as can be seen by a casual inspection of Fig.(6). This visual impression is confirmed in the analysis of the steady-state power spectra $P(\omega, k_y)$, which we present in Section 6.5.

4.4 Minimum Length for a Two-Vortex Steady-State

In the present simulation, we did not determine the minimum length in y required for the existence, in the steady-state, of more than one large vortex. Furthermore, limitations on computational resources did not permit us to explore longer systems in which such a state might appear. We would like to argue however, using qualitative arguments, that a minimum length for a

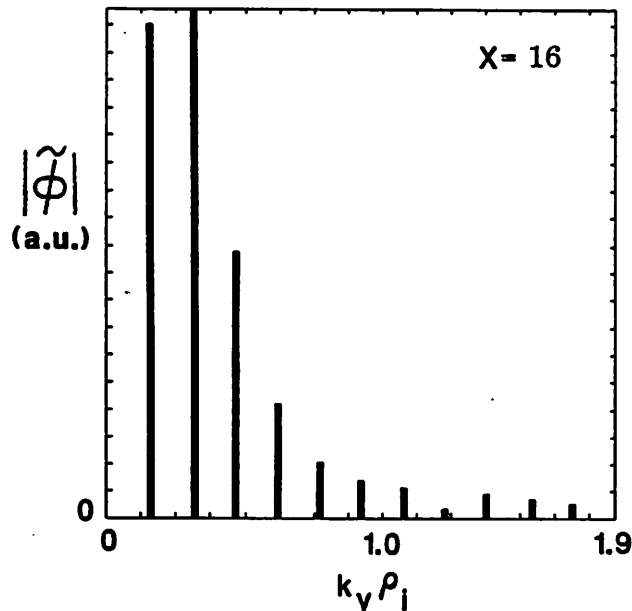


Figure 7: Relative amplitudes of the Fourier modes $|\tilde{\phi}(k_y, x, t)|$ at $\omega_{ci}t = 1050$, Run 1, for $x = L_x/2 = 16$.

two-vortex steady-state must exist. In other words, we are suggesting that it is physically reasonable to suppose that vortex coalescence can go not on indefinitely, and that the final state of any sufficiently long system will consist of more than one large-amplitude vortex. To support our assertion, let us consider a scenario where such a single-vortex state might initially prevail. We then argue that it may nonetheless result in a many-vortex state, provided that the system is long enough.

Let us assume that the single, final vortex is roughly circular, and occupies at any one time a limited extent in y , comparable to the sheath thickness in x , that is a few ion gyroradii. Then, we cannot overrule the possibility that in a very long system the shear layer may produce satellite vortices at some distance from the main vortex, as was seen in Fig.(4) at $\omega_{ci}t \approx 1000$. Provided that the system is long enough, and that the secondary vortices are appearing far enough from the main vortex, these satellite vortices should have the time to develop large amplitudes of their own, even if they eventually merge with other vortices in the system. Thus, in the steady-state the system may contain many vortices. In connection with this scenario, we would also like to argue that the oldest and largest vortices may not grow indefinitely by engulfing the satellite vortices. Pre-

sumably, very large amplitude vortices with $|e\delta\phi/T_i| \gg 1$ are unstable, and can shed energy either by interaction with the wall, or perhaps emission of waves. The final result will be a self-limiting state consisting of many large (but not indefinitely large) amplitude vortices, in constant interaction with each other.

The qualitative arguments outlined above are clearly insufficient, and should be supported by future numerical simulation of longer systems.

4.5 Saturation Mechanisms: Climax and Coalescence

We shall now make a comparison between the transient plasma behavior observed in Run 1, and the transient behavior of the fluid Kelvin-Helmholtz instability, as observed in purely hydrodynamic fluid simulations. Our aim is to provide, through this analogy, qualitative explanations of the saturation and coalescence phenomena seen in Run 1. The basis of the analogy is the close similarity, in the fluid approximation, of the plasma cross-field equations, to be derived in Section 5, with the hydrodynamic, Navier-Stokes equation (21).

We note here that a rigorous, analytic solution of the Navier-Stokes equations for the nonlinear evolution of the fluid Kelvin-Helmholtz instability is so far lacking. Though a variety of special steady-state solutions can be found (periodic, soliton-like, localized), there is no rigorous procedure to predict the appearance of a given kind of nonlinear structure from arbitrary initial conditions (as can be done, say, in the case of the Korteweg-deVries equation). Because of this state of affairs, we expect that a description of the nonlinear dynamics of our system, even in the fluid approximation, must remain at best semi-quantitative.

As we saw, the general trend in Run 1 was the following: after a few e-folding times the linear instability saturated into a state consisting of several quasi-stable vortices, which eventually coalesced into larger structures, leading to a final unique and stable vortex. This evolution is quite similar to that observed in numerical simulations of two-dimensional, sheared fluid flows. For the purpose of the present analogy, we shall especially refer to the work of Corcos[20,21,22].

Corcos[20,21,22] has presented a qualitative model for the saturation of single vortices in the fluid Kelvin-Helmholtz instability, starting from small amplitudes. The saturated state has been termed the *climax* state. We

believe that this model is qualitatively valid for the plasma instability as well, and we shall sketch its outlines. Let us first emphasize the connection between vorticity and charge density in the plasma fluid. If the plasma flows are given by $\mathbf{v} = \mathbf{E} \times \mathbf{B}/B$, then the vorticity is simply:

$$\omega_z = (\nabla \times \mathbf{v})_z = -\rho/B\epsilon_0 \quad (1)$$

where ρ is the local charge density. Thus, at any time we can identify vorticity with (minus) the charge density.

The Corcos model for the evolution to the "climax" state depends on the reciprocal interaction of the vorticity and the fluid flow, with the vorticity driving the flow through Ampère's law, and being itself advected by the flow through the continuity equation. The model proceeds as follows: as the initially small-amplitude fields grow, they divide the fluid into free and trapped flows, the trapped flows corresponding to the growing vortices. Now, the Kelvin-Helmholtz instability grows by extracting vorticity from the free-flowing shear layer. This vorticity is convected into the trapped regions, where, once trapped, it becomes unavailable as a source of free-energy. The convection of vorticity from free to trapped regions proceeds in two steps; first, the vorticity, which is initially diffuse throughout the shear layer, is concentrated by the large-amplitude flows into a narrow band along the vortex separatrix; this band of vorticity is then advected into the vortex core at a point roughly at the end of the separatrix (at the point of maximum excursion into the shear layer), by a combination of stretching and rolling of the stream-line defining the separatrix. Because the total supply of vorticity is constant in this inviscid flow, the instability will cease to grow when all of the vorticity has been extracted from the shear layer and concentrated inside the vortices (because of the uncertainties of the model, in fact it only requires that an appreciable fraction of the total vorticity be trapped).

Let Q_{vor} denote the net charge trapped inside the vortex, and Q_0 the initial, net charge in one wavelength of the Kelvin-Helmholtz instability. Then, on account of Eq.(1), the climax condition for the saturation of the individual vortices can also be expressed as:

$$Q_{vor} \approx Q_0 \quad (2)$$

In other words, the vortex saturates when it has trapped most of the net

charge resident in the shear layer. This occurs when the separatrix width becomes comparable to the width of the shear layer, and is indeed what is observed in Figs.(3). Another, semi-quantitative consequence of Corcos' model is that the growth of the vortex should proceed at an algebraic rate throughout the finite-amplitude part of its evolution, a feature which was observed in the graphs of Figs.(6).

Let us now comment on the process of vortex coalescence, a process which is also a generic feature of the hydrodynamic simulations, and which immediately follows the climax of individual vortices. The vortices coalesce as a result of a nonlinear instability, the so-called *pairing instability* first derived by Lamb for point vortices[23]. This instability has since then been analysed for more realistic vortex configurations[24].

For a row of two-dimensional point-vortices, initially equally spaced at a distance b , and each with net circulation $\Gamma_{vor} \equiv \int \omega_z dx dy$, one finds that the arrangement is unstable, with a maximum linear growth rate corresponding to a motion in which the vortices converge in pairs, the pairing instability. The growth rate for this mode is[23]:

$$\gamma_{pair} = \frac{\Gamma_{vor}}{2b^2} \quad (3)$$

In Section 5.2, we shall see that for a shear layer of width b , with characteristic velocity V_0 , the maximum linear growth rate scales as:

$$\gamma_L \sim \frac{V_0}{b} \quad \text{for } \lambda_y \sim b \quad (4)$$

where we have ignored all numerical factors. To compare Eqs.(3) and (4), we note that the total circulation Γ_0 in one wavelength of the initial shear layer is:

$$\Gamma_0 = bV_0 \quad (5)$$

Using Eqs.(3), (4) and (5), we find that:

$$\gamma_{pair} \sim \gamma_L \frac{\Gamma_{vor}}{\Gamma_0} \quad (6)$$

Now in Corcos' model, the vortices saturate precisely when $\Gamma_{vor}/\Gamma_0 \sim 1$. This implies that as soon as the vortices saturate, the pairing instability will immediately set in, with a growth rate of order $\gamma_{pair} \sim \gamma_L$. In agreement

with Figs.(3), this precludes a long-lived many-vortex state, at least in the early phases of evolution, when the vortices are closely packed in a periodic or near-periodic fashion.

4.6 Behavior when $k_{\parallel} \neq 0$

We briefly explored the behavior of the sheath when $k_{\parallel} \neq 0$. In our two-dimensional simulations, this was done by tilting the magnetic field at a finite angle to the z -axis. We considered a system half as large as in Run 1, with $L_y = 128$ and with half the particle injection rate, but with otherwise identical parameters.

In a first configuration, we tilted the magnetic field in the direction of the y -axis, by setting $\mathbf{B} = (0, B \sin \alpha, B \cos \alpha)$, with an angle $\alpha = \frac{1}{2}(m_e/m_i)^{1/2} = 4.53^\circ$. In this configuration the magnetic field remained parallel to the wall, but allowed particle flow along the field lines in the y direction, with a parallel velocity of order $v_{\parallel} \sim v_t \sin \alpha$, where v_t is the thermal velocity.

We expected important changes in the sheath dynamics to occur when the electrons could flow at a parallel velocity comparable to their $\mathbf{E} \times \mathbf{B}$ drift velocity. Since, as we shall see, the $\mathbf{E} \times \mathbf{B}$ velocities in the sheath are of order $v_D \sim v_{ti}$, we expected the transition to occur when $v_{e\parallel} \sim v_{ti}$, or at a "critical" angle $\alpha \approx (m_e/m_i)^{1/2}$. In fact, even the smaller angle $\alpha = \frac{1}{2}(m_e/m_i)^{1/2}$ was sufficient to greatly modify the course of the simulation, by completely suppressing the formation of vortices and edge turbulence. While the system generated a one-dimensional sheath almost identical to the one-dimensional sheath generated in the early phases of Run 1 (with potential drop $e\Delta\phi/T_i = -1.4$), this one-dimensional sheath remained absolutely stable in time, and did not induce particle transport (most particles injected into the system remained confined). We suspect that this stability is a consequence of the parallel electron motion, which stabilizes the Kelvin-Helmholtz instability by short-circuiting potential perturbations which might arise in the shear layer.

In a second configuration, we tilted the magnetic field in the direction of the x axis, thereby making the field lines impinge onto the walls. This was done by setting $\mathbf{B} = (B \sin \beta, 0, B \cos \beta)$, with $\beta = (m_e/m_i)^{1/2}/8 = 1.13^\circ$. Despite the small value of the tilting angle, this configuration resulted in a completely different type of sheath, in which the electron flow dominated

the sheath dynamics. The wall took on a negative surface charge, and the electrostatic potential now exhibited a *rise* going from the wall to the plasma, of order $e\Delta\phi/T \sim 0.3$. Thus, in this configuration, the cross-field sheath was suddenly made to resemble the unmagnetized sheath, and we can regard the introduction of the tilting angle β as a “singular” perturbation. We did not perform a systematic study of the sheath with $\beta \neq 0$; however we expect that it is well described by the work of Chodura[8].

The results of the two cases outlined above emphasize that the sheath model that we are studying in this paper applies strictly to flute-like modes, with a very small k_{\parallel} . For our $k_{\parallel} = 0$ model to be approximately valid when $k_{\parallel} \neq 0$, requires that in the characteristic time needed for the Kelvin-Helmholtz instability to develop, the electrons sample only a fraction of a parallel wavelength $\lambda_{\parallel} = 2\pi/k_{\parallel}$. This imposes the condition $\lambda_{\parallel}/v_{te} \gg \gamma_{KH}^{-1}$, where γ_{KH} is the growth-rate of the Kelvin-Helmholtz instability. As we shall see in Section 5.2, $\gamma_{KH}^{-1} \geq 20\omega_{ci}^{-1}$ (Fig.(12)). The result is the condition:

$$\lambda_{\parallel} > 20 \left(\frac{m_i}{m_e} \right)^{1/2} \rho_i \quad (7)$$

or in terms of parallel wavenumber:

$$k_{\parallel}\rho_i < \frac{1}{20} \left(\frac{m_i}{m_e} \right)^{1/2} \quad (8)$$

5 Fluid Theory

In this section, we derive the fluid equations for the cross-field dynamics of the electrons and ions. Our aim is twofold: in the present section we use the cross-field equations in linearized form, and predict the initial growth rates for the Kelvin-Helmholtz instability. In Section 6 we shall then consider nonlinear solutions of these equations, and attempt to fit these solutions to the final steady-state observed in Run 1. Our approach is similar to that taken by several authors[16,25].

The cross-field equations are two coupled, nonlinear evolution equations, linking the electrostatic potential to the particle density. As we shall see, there is a close analogy between these plasma equations and the two-dimensional, inviscid Navier-Stokes equation[26]. This analogy was the basis for the discussion of Section 4.5, in which we compared the evolution of the plasma simulation to that of hydrodynamic simulations.

Following a general derivation of the fluid equations, we derive the linearized form of the cross-field equations, assuming that the equilibrium conditions at the edge are known. To determine these equilibrium conditions, we fit analytic ($\tanh(x)$) profiles to the initial velocity and density profiles measured in Run 1. We then solve numerically the linearized fluid equations, and obtain estimates for the growth rates and frequencies, and the eigenfunctions of the unstable Kelvin-Helmholtz modes. This linear analysis, which assumes a nonuniform density profile and the presence of a finite conducting boundary, is considerably more general than the usual analysis of the Kelvin-Helmholtz instability[12], which is done for a constant density profile and boundary conditions at infinity. The results of our linear analysis are then compared to the numerical results of the two-dimensional simulations, with the aim of confirming that the instabilities seen in the simulations can indeed be ascribed to the Kelvin-Helmholtz instability of the edge shear layer. We find reasonable agreement for the long-wavelength modes, but a sharper cutoff for the shorter wavelength modes, indicating strong finite-larmor-radius effects not accounted for in the fluid theory.

The fluid theory assumes that we are modelling low-frequency, long-wavelength phenomena, with $|\omega| \ll \omega_{ci}$ and $|\mathbf{k}| \rho_i \ll 1$. Fortunately, inspection of the self-consistent simulation results shows that these conditions are indeed approximately satisfied. Fig.(7) showed that the dominant Fourier modes were those with $|k_y| \rho_i < 1$, and an examination of the power spec-

tra $P(\omega, k_y)$ (Fig.(20), to be discussed in Section 6.5) shows that for the long-wavelength modes, power is concentrated at frequencies $|\omega| \ll \omega_{ci}$.

As an aside, we note that the dominance of low-frequency, long-wavelength modes over short-wavelength, high-frequency fluctuations can be readily seen in a computer animation of the potential surface $\phi(x, y, t)$, which we generated from data produced in a simulation with parameters similar to those of Run 1[5].

Thus, the fluid theory correctly describes the dominant, long-wavelength, low-frequency features of the cross-field dynamics (the linear instability, the formation of vortices, vortex coalescence and vortex structure), but will not account for the small-amplitude, fluctuating behavior of the fields at short wavelengths, $k_y \rho_i \sim 1$. Presumably, the short-wavelength phenomena are correctly described only by the full kinetic equations, the solution of which is a topic for future research.

5.1 The Nonlinear Cross-Field Equations

Our derivation is similar to the one presented by Horton et al.[16]. In the regime $\omega \ll \omega_{ci}$, we simplify the electron and ion momentum equations by approximating the electron motion by the $\mathbf{E} \times \mathbf{B}$ drift, and the ion motion by the $\mathbf{E} \times \mathbf{B}$ and polarization drifts:

$$\mathbf{v}_e = \frac{1}{B}(\mathbf{E} \times \hat{z}) \equiv \mathbf{v}_E \quad (9)$$

$$\mathbf{v}_i = \frac{1}{B}(\mathbf{E} \times \hat{z}) + \frac{1}{B\omega_{ci}} \frac{d}{dt} \mathbf{E} \equiv \mathbf{v}_E + \mathbf{v}_P \quad (10)$$

In Eq.(10), d/dt is the total derivative,

$$\frac{d}{dt} = \frac{\partial}{\partial t} + \mathbf{v}_E \cdot \nabla \quad (11)$$

With the electron and ion flows given by Eqs.(9,10), the densities must satisfy the continuity equations:

$$\frac{\partial}{\partial t} n_e + \nabla \cdot (\mathbf{v}_E n_e) = 0 \quad (12)$$

$$\frac{\partial}{\partial t} n_i + \nabla \cdot ((\mathbf{v}_E + \mathbf{v}_P) n_e) = 0 \quad (13)$$

Subtracting Eq.(12) from Eq.(13), we obtain a transport equation for the net charge separation:

$$\frac{\partial}{\partial t}(n_i - n_e) + \nabla \cdot (\mathbf{v}_E(n_i - n_e) + \mathbf{v}_P n_i) = 0 \quad (14)$$

Using $\nabla \cdot \mathbf{v}_E = 0$, Eq.(14) can be written:

$$\frac{d}{dt}(n_i - n_e) + \frac{1}{B\omega_{ci}} \nabla \cdot \left(n_i \frac{d}{dt} \mathbf{E} \right) = 0 \quad (15)$$

If we now use Poisson's equation:

$$\nabla^2 \phi = -\frac{e}{\epsilon_0}(n_i - n_e) \quad (16)$$

and substitute for $n_i - n_e$ in Eq.(15), we obtain a single equation tying the electrostatic potential to the ion density. To this equation, we append the electron continuity equation (12). Using the quasineutrality condition, $n_e \approx n_i \equiv n$, we obtain the coupled nonlinear equations:

$$\frac{m_i \epsilon_0 \omega_{ci}^2}{e^2} \frac{d}{dt} \nabla^2 \phi + \nabla \cdot \left(n \frac{d}{dt} \nabla \phi \right) = 0 \quad (17)$$

$$\frac{d}{dt} n = 0 \quad (18)$$

This set of equations is similar to the cross-field equations of Horton et al.[27], differing by the addition of the first term in Eq.(17), which allows for a finite value of ω_{ci}/ω_{pi} . Eqs.(17,18) have some simpler limiting forms. If $\omega_{pi}^2 \gg \omega_{ci}^2$, then we can neglect the first term in Eq.(17) and obtain:

$$\nabla \cdot \left(n \frac{d}{dt} \nabla \phi \right) = 0 \quad (19)$$

$$\frac{d}{dt} n = 0 \quad (20)$$

If we further assume that n is everywhere constant, so that the transport equation (20) is trivially satisfied, we obtain a single nonlinear equation for ϕ :

$$\left(\frac{\partial}{\partial t} + \frac{1}{B} (\hat{z} \times \nabla \phi) \cdot \nabla \right) \nabla^2 \phi = 0 \quad (21)$$

Eq.(21) is identical to the two-dimensional Navier-Stokes equation, with stream-function ϕ . We note that to derive Eq.(21) from Eq.(17) does not require the assumption of $\omega_{pi}^2 \gg \omega_{ci}^2$, but only that of constant density. Finally, if $\omega_{pi}^2 \ll \omega_{ci}^2$, Eq.(17) once again implies Eq.(21), this time irrespective of any assumptions on the behavior of the density profile. Thus Eqs.(17,18) are close in nature to the two-dimensional Navier-Stokes equation, Eq.(21), in a manner that is not very sensitive to the value of $\omega_{pi}^2/\omega_{ci}^2$.

5.2 Growth-Rates of the Kelvin-Helmholtz Instability

We shall now estimate the growth rates predicted by Eqs.(17,18) in the presence of specified zero-order velocity and density profiles. In what follows, we did not use the exact, numerical profiles obtained in Run 1, but rather, we fitted approximate analytic forms to these profiles: this procedure leads to a fully analytic treatment of the instability, and avoids the problems associated with finite noise in the numerical results.

In Fig.(8), we show a snapshot of the “exact”, zero-order profiles as they were obtained from the self-consistent, two-dimensional calculation of Run 1. The snapshot is taken at an early time in the evolution of the system, $\omega_{ci}t = 15$, at which time the sheath is still uniform in y . To predict the growth rates, we model these numerical velocity and density profiles by analytic expressions of the form:

$$v_0(x) = V_0 \hat{v}_0(x) \quad (22)$$

$$n_0(x) = N_0 \hat{n}_0(x) \quad (23)$$

where we have defined $v_{0y}(x) \equiv v_0(x)$. In Eqs.(22,23) V_0 and N_0 are convenient reference velocities and densities. We have chosen the functional dependences:

$$\hat{v}_0(x) = \tanh(x/a - 1) - 1 \quad (24)$$

$$\hat{n}_0(x) = \tanh(x/d) \quad (25)$$

With Eqs.(22-25), the equilibrium density far from the wall is given by N_0 , the drift velocity at the wall is given by $-(1 + \tanh(1)) = -1.761V_0$, d is the scale length for the density gradient, and finally, a locates the position of the inflection point in the velocity profile ($\rho'(a) \equiv 0$). Fitting to the simulation curves of Fig.(8), we find the values (in the units of ES2):

$$V_0 = 0.0812 \quad a = 4.0 \quad (26)$$

$$d = 8.0 \quad \omega_{ci}^2/\omega_{pi}^2(n = N_0) = 0.73 \quad (27)$$

or, in physical parameters:

$$V_0/v_{ti} = 0.514 \quad a/\rho_i = 0.63 \quad (28)$$

$$d/\rho_i = 1.26 \quad (29)$$

The analytic profiles which result from this choice of parameters are shown in Fig.(9). It is convenient to introduce the parameter σ , defined as:

$$\sigma \equiv \frac{\omega_{ci}^2}{\omega_{pi}^2(n = N_0)} \quad (30)$$

Let us now linearize Eqs.(17,18), with the equilibrium given by Eqs.(22,23). Writing $\phi = \phi_0(x) + \phi_1(x, y, t)$ and $n = n_0(x) + n_1(x, y, t)$, we find after some algebra:

$$\begin{aligned} & \left(\frac{\partial}{\partial t} + v_0(x) \frac{\partial}{\partial y} \right) \left(\nabla^2 \phi_1 + \frac{\hat{n}'_0(x)}{\sigma + \hat{n}_0(x)} \frac{\partial}{\partial x} \phi_1 \right) \\ & - \left(v_0''(x) + \frac{\hat{n}'_0(x)}{\sigma + \hat{n}_0(x)} v_0'(x) \right) \frac{\partial}{\partial y} \phi_1 = 0 \end{aligned} \quad (31)$$

In this equation, we have not yet factored-out V_0 from $v_0(x)$. A simplification occurs in deriving Eq.(31), in that n_1 does not appear in Eq.(17). Thus, to first order Eqs.(17) and (18) are decoupled, and one need linearize only Eq.(17) to obtain a single equation for ϕ_1 , as we have done in (31).

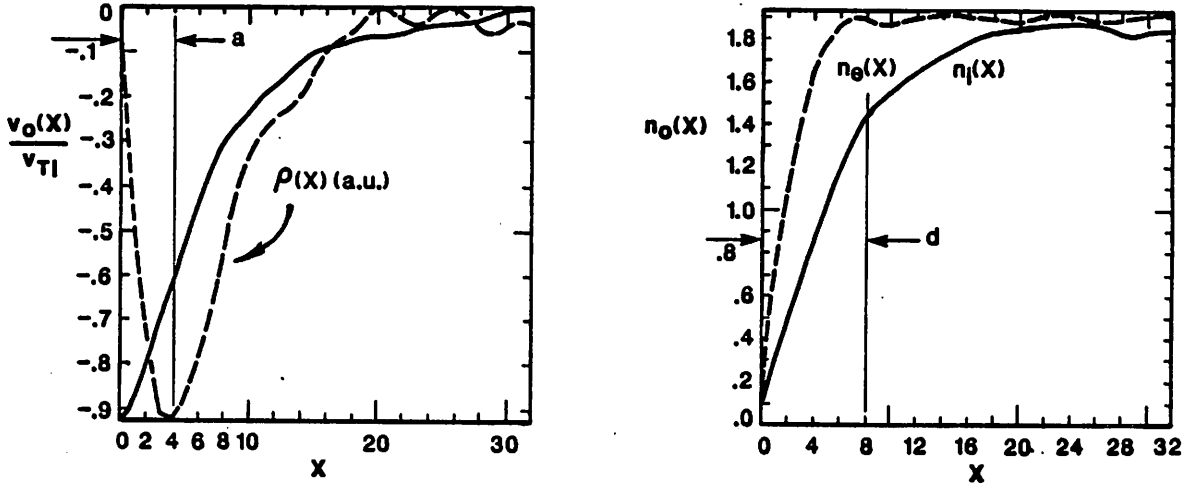


Figure 8: Velocity and density profiles for Run 1, at $\omega_{ci}t = 15$; (a) y -averaged velocity $\bar{v}_y(x) = v_0(x)$ and charge-density profiles (full and dashed lines respectively); note that the minimum of $\bar{\rho}(x)$, at $x \equiv a$, determines the inflection point $\bar{v}_y'' = 0$; (b) density profiles for electrons and ions; the zero-order density in Eq.(23) is $n_0(x) \equiv n_i(x)$, and d is the scale length in Eq.(25).

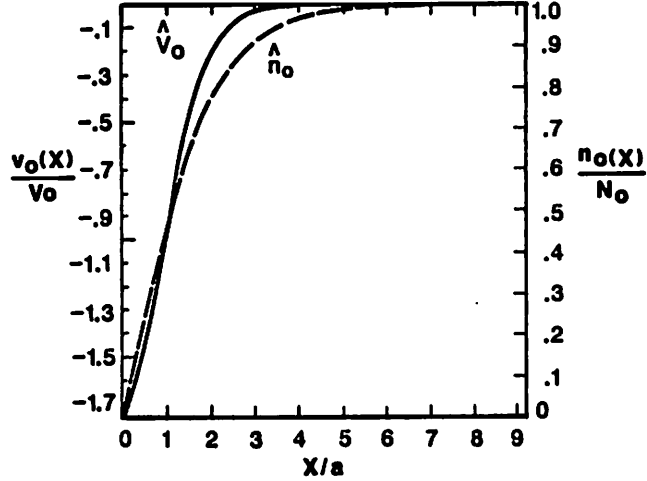


Figure 9: Shapes of the analytic velocity and density profiles used in predicting the growth-rates of the Kelvin-Helmholtz instability.

A rather lengthy eigenvalue equation is obtained by assuming an $\exp(i(k_y y - \omega t))$ dependence for the normal modes:

$$\frac{\partial^2}{\partial x^2} \phi_1 + \frac{\hat{n}'_0(x)}{\sigma + \hat{n}_0(x)} \frac{\partial}{\partial x} \phi_1 + \left(\frac{k_y}{\omega - k_y v_0(x)} \left(v_0''(x) + \frac{\hat{n}'_0(x) v_0'(x)}{\sigma + \hat{n}_0(x)} \right) - k_y^2 \right) \phi_1 = 0 \quad (32)$$

Eq.(32) can be made to appear more familiar, if we realize that for a constant density profile, $\hat{n}'_0(x) = 0$, or in the limit of low peak densities, $\sigma \rightarrow \infty$, Eq.(32) reduces to the well-known Rayleigh stability equation[28,29]. The new terms in Eq.(32) are those proportional to the density gradient $\hat{n}'_0(x)$.

We now consider the numerical solution of Eq.(32), for arbitrary density profiles. To find the frequencies and growth rates of the unstable modes, it is convenient to solve Eq.(32) not as an eigenvalue problem, but directly in the time-dependent form (31), as an initial-value problem[15]. In this approach, we introduce an intermediate quantity ψ_1 , defined as the term in Eq.(31) that is operated upon by the convective derivative $(\partial_t + v_0(x)\partial_y)$. Eq.(31) is then re-written as a coupled system:

$$\left(\frac{\partial}{\partial t} + ik_y V_0 \hat{v}_0(x)\right) \psi_1 = ik_y V_0 \left(\hat{v}_0''(x) + \frac{\hat{n}_0'(x)}{\sigma + \hat{n}_0(x)} \hat{v}_0'(x)\right) \phi_1 \quad (33)$$

$$\left(\frac{\partial^2}{\partial x^2} + \frac{\hat{n}_0'(x)}{\sigma + \hat{n}_0(x)} \frac{\partial}{\partial x} - k_y^2\right) \phi_1 = \psi_1 \quad (34)$$

Eqs.(33) describes the convection of ψ_1 , which is driven by a source term proportional to ϕ_1 . Eq.(34) describes the reaction of ψ_1 on ϕ_1 , which occurs via a modified Poisson's equation. In the limit of a constant density, ψ_1 is simply proportional to the linearized charge density, and Eqs.(33,34) have a clear physical interpretation, the transport of charge and its subsequent modification of the potential, which is somewhat obscured by the presence of the density-gradient dependent terms.

We solve Eqs.(33,34) for the unstable modes with the largest growth-rates by integrating numerically from random-noise initial conditions; we then measure the growth-rate of the mode which emerges out of the noise. The numerical method is straightforward; Eq.(33) is solved by a predictor-corrector scheme, with ϕ_1 obtained from Eq.(34) through a tridiagonal matrix solution. Throughout, we impose the conducting-wall boundary condition, $\phi_1(x = 0) = 0$, and a far-field condition $\phi_1(x = L) = 0$, where $L \gg a, d$. The overall method is, of course, limited to determining the eigenvalues of the unstable, fastest-growing modes; but this is all we require for comparison with the simulation results.

In Fig.(10) we show the results of our numerical integration of Eqs.(33,34) with the parameters of Eqs.(26,27). We have plotted the the real and imaginary parts of the frequency $\omega = \omega_R + i\gamma$ as functions of $k_y a$. From Eq.(32) one can establish the general functional dependence of the eigenfrequencies:

$$\omega = \frac{V_0}{a} \Omega(k_y a, k_y d, \sigma) \quad (35)$$

where Ω is obtained from a normalized form of Eq.(32), which depends only on the dimensionless parameters $k_y a$, $k_y d$ and σ . Furthermore, the roots occur in pairs such that $\Omega(-k_y) = -\Omega^*(k_y)$. Thus, for a given choice of d/a and σ , one needs to compute numerically the dependence of Ω on only *one* free parameter, $|k_y| a$, and for only positive k_y , a simplification which

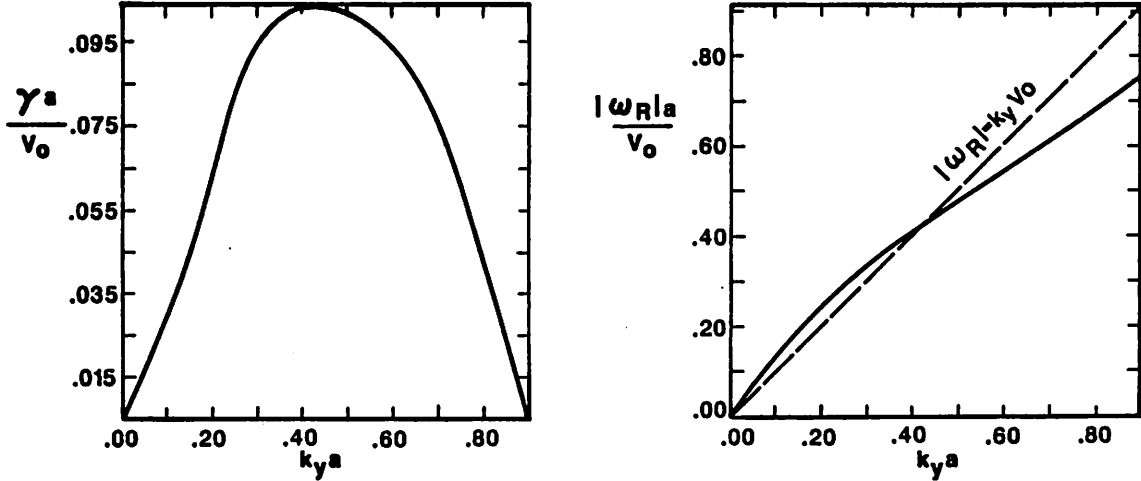


Figure 10: Growth-rates and frequencies for the Kelvin-Helmholtz instability, with the equilibrium profiles of Eqs.(22-25); $d/a = 2$, $\sigma = 0.73$.

reduces the numerical work. Fig.(10) is established with the parameters of Eqs.(26,27), with $d/a = 2$ and $\sigma = 0.73$.

The curve for the growth rate $\gamma(k_y)$ is shown in Fig.(10a). Its shape is roughly parabolic, with cutoffs at $k_y a = 0$ and $k_y a = 0.9$, and predicts a maximum growth rate of $\gamma = 0.099V_0/a$, which occurs at $k_y a = 0.43$. The curve for the real part of the frequency is plotted in Fig.(10b). This figure shows that the dispersion relation is approximated by the linear relation $\omega_R(k_y) = -k_y V_0$. This result is not surprising: the unstable Kelvin-Helmholtz modes can be thought of as resulting from the interaction of two counter-streaming surface waves, moving symmetrically with respect to the drift velocity at the inflection point in the velocity profile[11]. In the frame co-moving with the inflection point, the interaction leads to an almost purely-growing mode. Now, with the profile of Eq.(24), the velocity of the inflexion point is precisely $-V_0$, and this results, in the lab frame, in the linear dispersion relation noted above. The fastest-growing mode is indeed exactly purely-growing in the co-moving frame, and results in the real frequency $\omega_R = -0.43V_0/a$.

In Fig.(11) we plot the eigenfunction $\phi_1(x)$ corresponding to the maximum growth rate. In this plot, we can see that while the peak of the

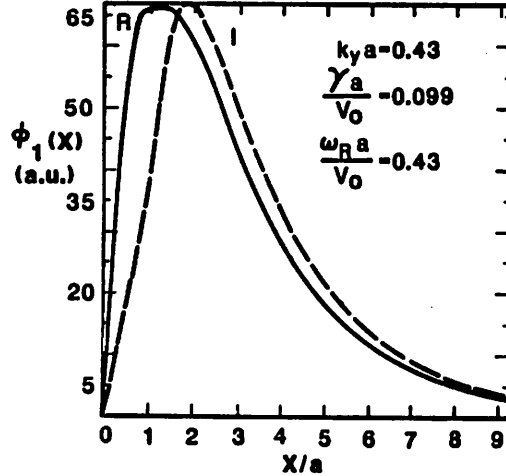


Figure 11: Eigenmode structure for the fastest-growing Kelvin-Helmholtz mode of Eq.(32).

eigenfunction occurs at $x = 1.5a$, that is, right at the edge of the shear layer, the eigenfunction also embodies a long exponential tail which penetrates deep into the plasma, up to a distance $x \sim 10a$.

In Figs.(12), we have reproduced Figs.(10), but have normalized all variables to the physical parameters. Note that the fluid results do not incorporate any finite-gyro-radius effects, despite what might be inferred from the presence of the $k_y \rho_i$ term. In Figs.(12), we have also plotted the data for the growth rates and the real parts of the frequencies as directly obtained from Run 1. The comparison shows that the analytic predictions for the real part of the frequency agree reasonably well with the simulation results. On the other hand, while the growth-rates for the long-wavelength modes ($m = 1, 2$) are in good agreement, fluid and simulation results diverge as we go to the shorter wavelengths ($m = 3, 4, 5, 6$): while the fluid model predicts in this case a cutoff at $k_y \rho_i = 1.4$, the simulation results exhibit a lower cutoff, at $k_y \rho_i = 0.9$, with a smaller maximum growth rate. Let $\gamma_F(k_y)$ denotes the growth-rate predicted by the fluid theory, and $\gamma_N(k_y)$ the numerical result of Run 1. We have found the approximate, empirical relation:

$$\gamma_N(k_y) \approx \gamma_F(k_y) - 0.1 \omega_{ci} (k_y^2 \rho_i^2) \quad (36)$$

It is reasonable to think that the “correction” term in Eq.(36) accounts for finite-larmor radius effects not present in the fluid theory, and we can qualitatively account for the quadratic dependence of this term by the following derivation. We first naively add the orbit-averaged contribution:

$$\mathbf{v}_{FLR} = \frac{1}{4} \rho_i^2 \nabla^2 \left(\frac{\mathbf{E} \times \hat{z}}{B} \right) \quad (37)$$

to the ion velocity in the continuity equation, Eq.(13). This yields, in the limit where the Navier-Stokes equation is valid, the following equation:

$$\frac{\partial}{\partial t} \nabla^2 \phi + \frac{1}{B} [\phi, \nabla^2 \phi] - \frac{1}{4} \omega_{ci} \rho_i^2 \nabla^4 \phi = 0 \quad (38)$$

In other words, there is now a diffusive term in the vorticity equation. This term leads to an additional damping ν which has the dependence:

$$\nu \sim -\omega_{ci} (k_x^2 + k_y^2) \rho_i^2 \quad (39)$$

and we note that the quadratic dependence of this term is at least compatible with that of the correction term in Eq.(36).

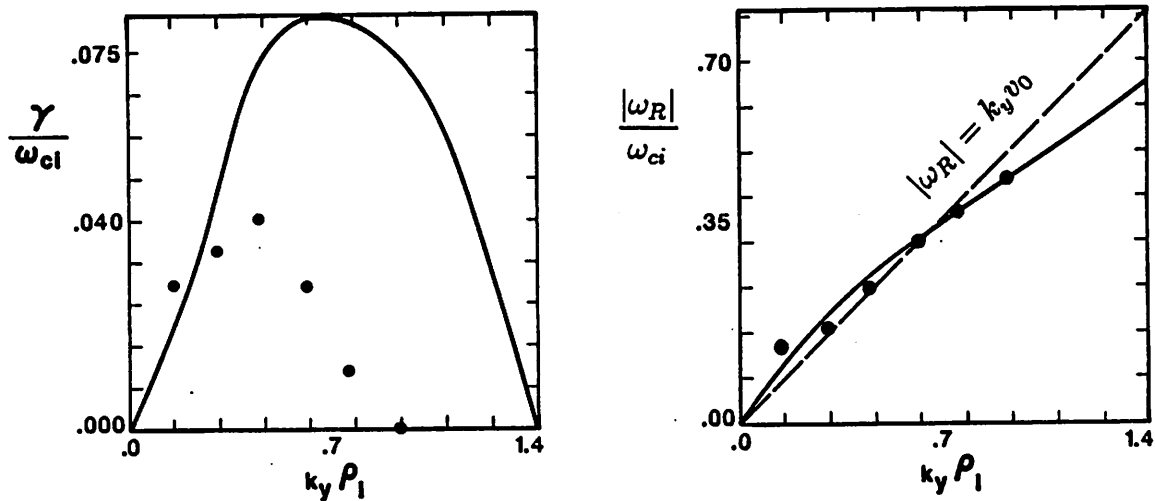


Figure 12: Comparison of the analytic results for the Kelvin-Helmholtz instability with the simulation results of Run 1; (a) growth rates; (b) frequencies.

6 Steady-State Structure of the Sheath

In the previous sections we discussed the transient behavior of the sheath; we shall now examine its steady-state structure. We shall first present the numerical results of Run 1, and discuss the structure of the fields and of the particle densities. We shall then make a connection with the fluid theory of Section 5, by fitting a solution of the fluid equations to the observed potential structures. The aim of this procedure is to make explicit the fluid nature of the vortices. We shall close this section with a discussion of the power spectra, which, in particular, provide information on the short-wavelength turbulence which complements the long-wavelength vortices.

6.1 Simulation Results

As we saw in Figs.(4), after $\omega_{ci}t \approx 500$ the sheath settles into a steady-state, in which a single large vortex uniformly drifts along the wall. This large vortex is occasionally accompanied by smaller “satellites”, which reside in the system for intervals of order $\omega_{ci}T \sim 100$. The average drift velocity

v_{0y} of the principal vortex can be computed from the slopes of the tracks in Fig.(4) and was found to be essentially constant. At $\omega_{ci}t = 700$, it was found to be $|v_{0y}|/v_{ti} = 0.44$ (or $v_{0y} = -0.065$ in the units of ES2).

A three-dimensional perspective plot of the electrostatic potential $\phi(x, y)$ at $\omega_{ci}t = 700$ is shown in Fig.(13). This figure clearly shows that the vortex produces a very sizeable perturbation of the edge potentials. In Figs.(14) we display more detailed information on the potential of Fig.(13), in the form of a contour plot and cross-sectional plots. The maximum potential drop in the vortex center, relative to the y -averaged potential profile (Fig.(14c)), is found to be $e\delta\phi/T_i = -2.4$, while the total drop of the y -averaged potential, from the wall into the plasma, is $e\Delta\phi/T_i = -1.9$. The dimensions of the separatrix of the vortex can be measured from Fig.(14a) and are found to be $l_y \approx 96$ ($l_y/\rho_i \approx 15$), and $l_x \approx 32$ ($l_x/\rho_i \approx 5$). Thus, if defined by its separatrix, the vortex has the shape of an ellipse elongated in the y -direction (this shape is distorted by the choice of scales in Fig.(14a)). However, the funnel of the vortex flares out more rapidly in the y -direction, and when considered say, half-way down the potential well, the shape of the vortex is more nearly circular.

In Fig.(14d) we have shown the y -averaged, x -directed electric field $E_x(x)$, which induces the drift $v_y(x) = -E_x(x)/B_0$. Fig.(14d) shows that the y -averaged velocity profile remains strongly sheared, even in the steady-state. At the wall, the drift velocity is $v_y(0)/v_{ti} = 1.25$, or roughly the ion thermal speed. The shear layer extends to about three ion gyro-radii inward, to $x \approx 20$.

In Fig.(15), we show the profiles of the y -averaged particle densities, $\bar{n}_e(x)$ and $\bar{n}_i(x)$. There is a region of large charge separation, in which $\bar{n}_e(x) > \bar{n}_i(x)$, extending to $x \approx 20$; this region corresponds to the electric field shown in Fig.(14d), and can be said to define the width of the y -averaged sheath. Beyond this region, for $20 \leq x \leq 32$, there is a narrow quasineutral region, in which $\bar{n}_e(x) \approx \bar{n}_i(x)$.

In Figs.(16a,b), we have displayed the "scatter plots" of the particle positions at $\omega_{ci}t = 700$. A striking feature of these scatter plots is the existence of a large region on the underside of the vortex, which is almost evacuated of particles. We shall discuss this feature in Section 7, in connection with our discussion of particle transport. Cross-sections of the local (unaveraged) electron and ion densities at $\omega_{ci}t = 700$ are shown

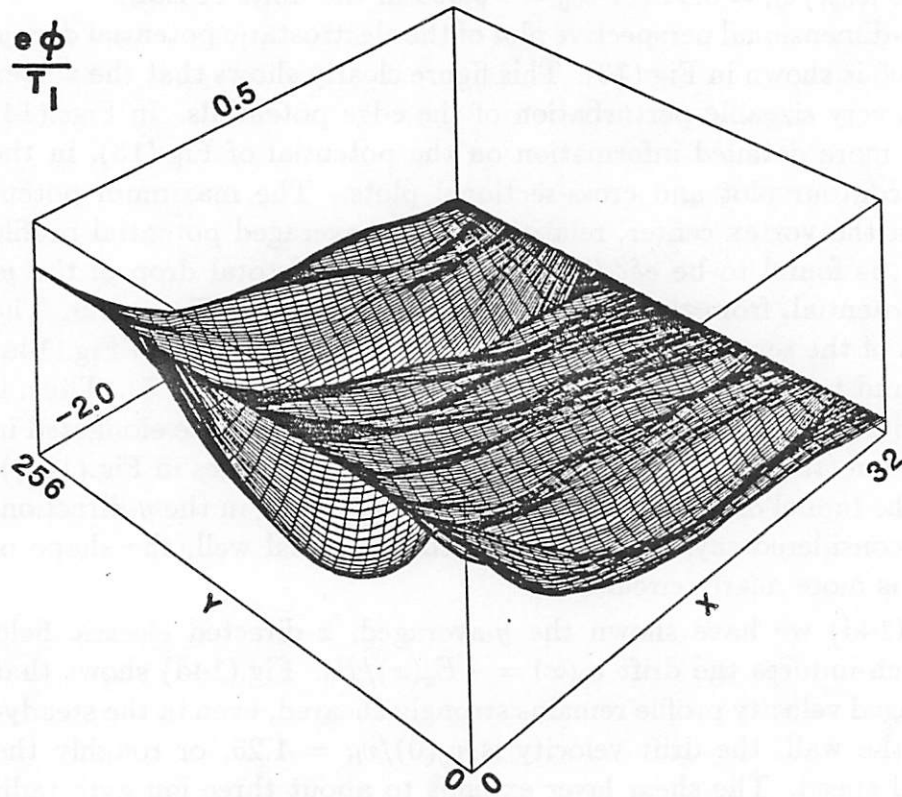


Figure 13: Perspective plot of the potential surface $\phi(x, y)$ at $\omega_{ci}t = 700$, Run 1. In this figure, the potential well of the vortex is drifting “southeasterly” from left to right.

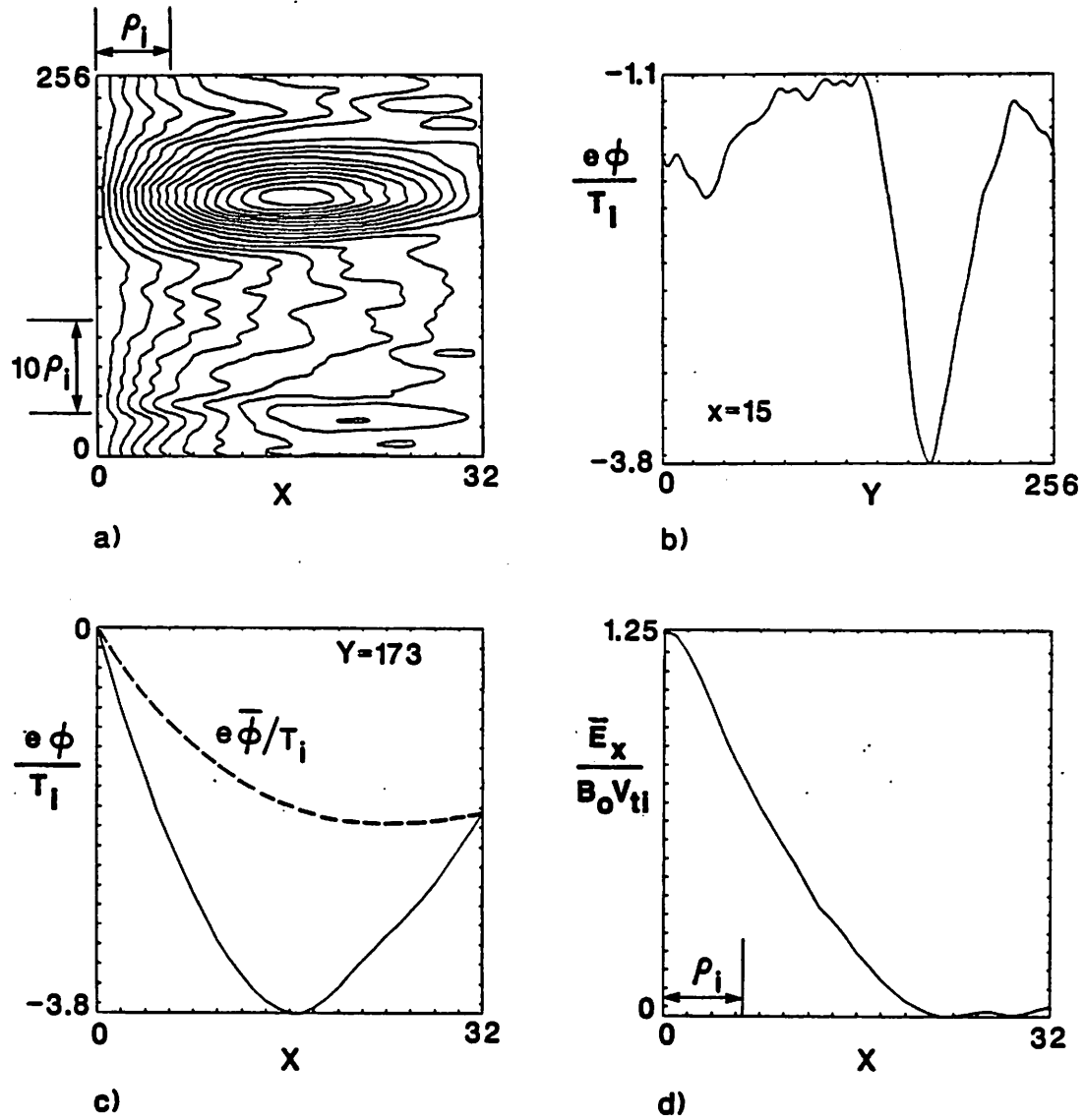


Figure 14: Details of the potential structure of Fig.(13), $\omega_{ci}t = 700$, Run 1; (a) contour plot of $\phi(x, y)$; (b) y cross-section of Fig.(a) along $x = 15$, passing through the vortex center; (c) x cross-section of Fig.(a) along $y = 173$, passing through the vortex center; (d) profile of the y -averaged electric field $\bar{E}_x(x)$.

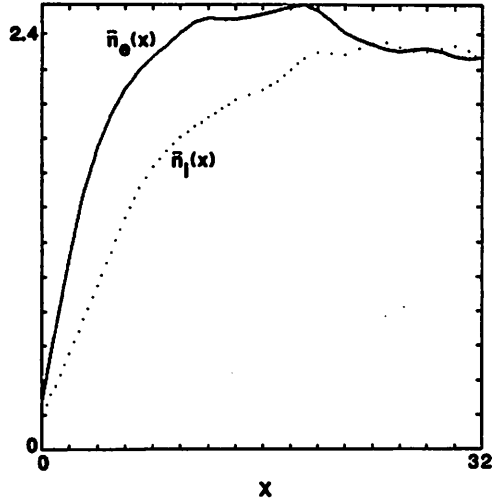


Figure 15: Profiles of the y -averaged electron and ion densities at $\omega_{ci}t = 700$, Run 1.

in Figs.(16c,d), onto which we have superposed the potential profile of Fig.(14b). Let us note the presence of a large electron density at the core of the vortex (Fig.(16c)). As can be seen, there is no corresponding peak in the ion density (Fig.(16d)). A large, net negative charge at the center is of course necessary to support the large potential drop in the vortex; Figs.(16c,d) provide the additional information that this charge is provided almost entirely by trapped electrons.

In Figs.(17) we look at the structure of the vortex at $\omega_{ci}t = 700$, in a reference frame *co-moving* with the vortex, at a (negative) velocity $v_{0y} = -0.065$. The potential as seen in this reference frame is found by adding to the potential in the lab frame a linear potential $\phi_c(x) = -v_{y0}B_0x$, corresponding to the electric field induced by the uniform motion across the background magnetic field. Fig.(17c) shows that E_x has an approximately linear dependence along the x -section of the vortex, with maxima $E_x/B_0 \approx \pm 1.5v_{ti}$. The field component E_y , when measured along the y -section of the vortex, is perhaps better approximated by a cosine, with maxima $E_y/B_0 \approx 0.6v_{ti}$. These values of the fields give us an estimate of the circulation time or “bounce time” of a particle around the potential well of the vortex. Estimating the circumference of the vortex as being

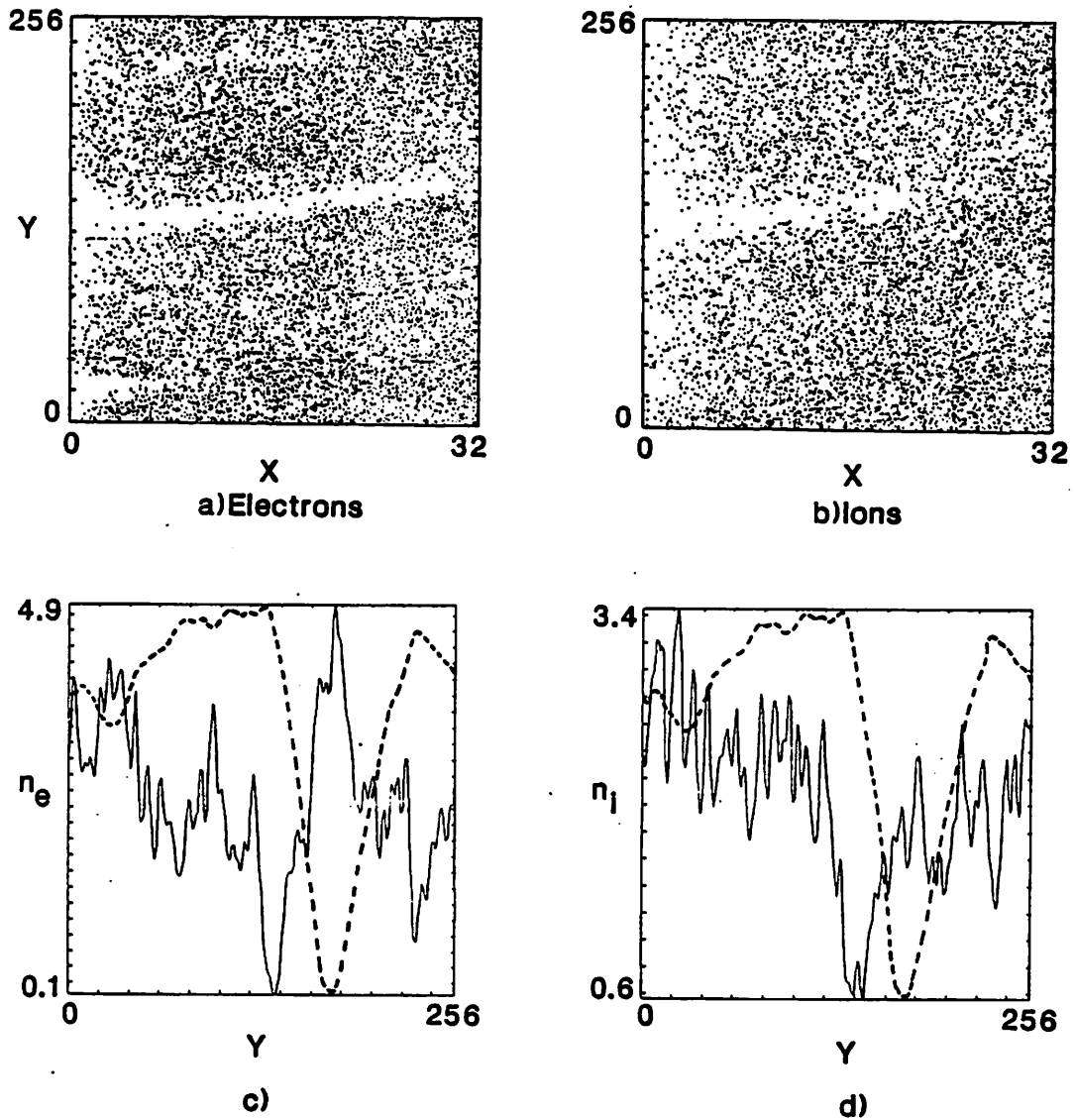


Figure 16: Distribution of particles at $\omega_{ci}t = 700$, Run 1; (a) electron scatter plot; (b) ion scatter plot; (c) y cross-section of the electron density $n_e(x, y)$ along $x = 15$, passing through the vortex center, with $e\phi(x, y)/T_e$ superimposed (dashed line); (d) identical to (c), but for the ion density $n_i(x, y)$.

$2 \times (l_y/2) \approx 15\rho_i$ (we are estimating the circumference half-way down the potential well), and taking the mean drift velocity to be $v_d \approx 0.6v_{ti}$, we find that particles will have a bounce period τ_B given by $\omega_{ci}\tau_B \approx 25$. This indicates that the bounce frequency ω_{B1} of the electrons is of order:

$$\omega_{B1} = 0.25 \omega_{ci} \quad (40)$$

where the estimate is for electrons roughly half-way up the potential well of the vortex.

6.2 Dependence of the Sheath Thickness on System Size

In Run 1, the vortex grew so as to occupy the entire width in x of the simulation region, and the nonneutral sheath also extended across the entire region (Fig.(15)). Thus, the question arises whether the sheath has a “natural”, self-limiting width in x , or whether it can grow indefinitely, provided the system is large enough to accommodate it. To answer this question, we ran a simulation in which L_x was 2.5 times larger than in Run 1. In Figs.(18) we show the results of this simulation, otherwise identical to Run 1, but with $L_x/\rho_i = 13$, $L_y/\rho_i = 20$, and an injection rate $s = 2.51$. Figs.(18) clearly show that in the larger system, the sheath remains localized near the wall. The vortex is seen to extend out to a distance $l_x \approx 5\rho_i$, beyond which the fields are nonzero, but rapidly decreasing. In Fig.(18c) we have shown the y -averaged electric field $\bar{E}_x(x)$. This figure shows that the shear layer is more localized than the vortex fields, a characteristic which was already illustrated in Fig.(11), where we saw that the eigenfunctions of the Kelvin-Helmholtz instability extend well beyond the region of nonzero shear. In Fig.(18d) we show the profiles of the steady-state electron and ion densities. This plot shows that in agreement with Fig.(18c), the region of charge nonneutrality is confined to the edge layer, $0 \leq x \leq 5\rho_i$. Beyond this edge region stretches a quasineutral plasma, which has a density profile that is roughly parabolic.

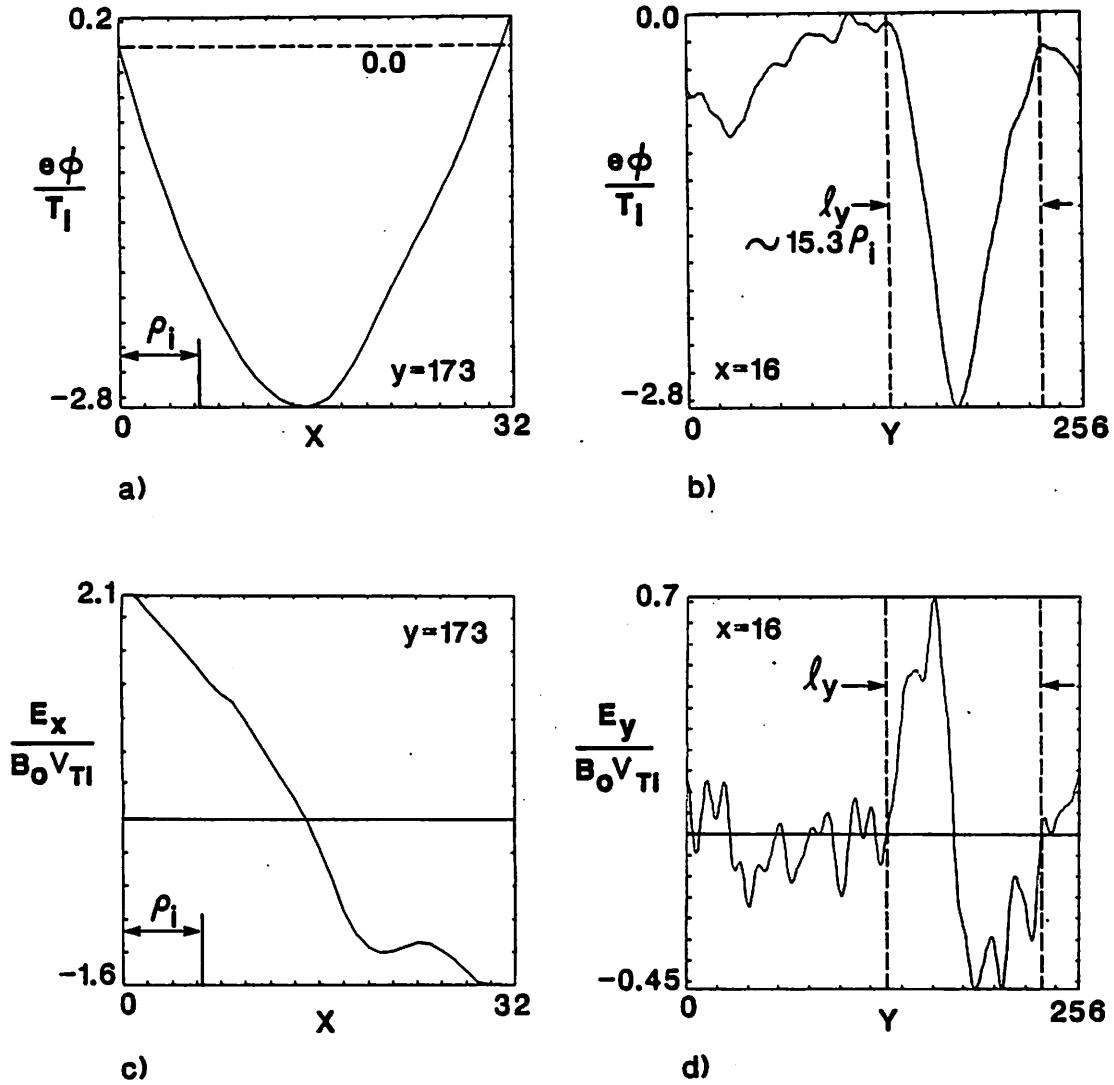


Figure 17: Cross-sections of the fields at $\omega_{ci}t = 700$, Run 1, in a frame co-moving with the vortex at a velocity $v_y = -0.44v_{ti}$.

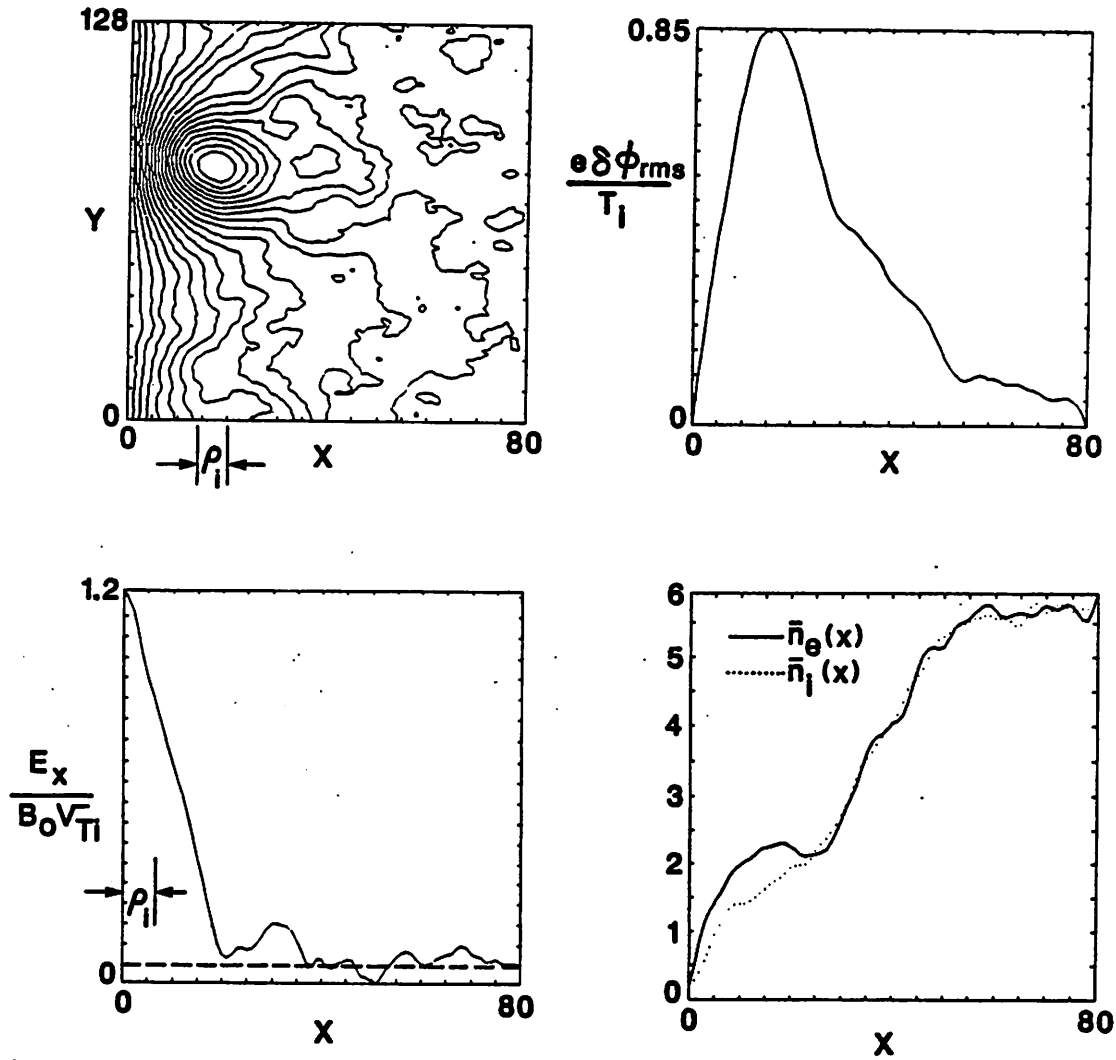


Figure 18: Steady-state results for a variation of Run 1: the system is 2.5 times broader in x , and half as long in y ; $L_x/\rho_i = 13$, $L_y/\rho_i = 20$, $s = 2.51$.

6.3 Localized Solutions for the Steady-State Vortex

The characteristics of the dominant vortex in the final steady state were illustrated in Figs.(14). We are now faced with the problem of providing an analytic solution for the vortex potential, consistent with the simulation results and with the cross-field equations (17,18). Our discussion will remain qualitative; in particular we shall assume that in our situation the Navier-Stokes equation (21) is an acceptable approximation to the full cross-field equations (17,18). This is equivalent to assuming that the effect of density variations can be ignored, by taking $n \approx \text{constant}$. While there are in fact strong density variations in the sheath (Fig.(16)), we are adopting this assumption because it greatly simplifies our quest for solutions of the cross-field equations: the literature on the Navier-Stokes equation is large, and many analytical solutions are available.

The solutions of the Navier-Stokes equation which are available in the literature are essentially of two types: the first type consists of localized, soliton-like solutions (“modons”)[30]; the second of periodic solutions, formed with trains of nonlinear waves. We shall examine these in turn.

The extent of the vortex of Fig.(14a) is small compared the system length L_y , and this suggests that we find a localized solution of the Navier-Stokes equation to fit to the observed vortex structure. This is the approach adopted by Horton et al.[16], who derive a solution for the asymptotic state of a symmetric shear layer, using a matching technique first used by Sagdeev et al.[25]. However, we have not had much success with this approach: this is because the resulting analytic solutions simply do not reproduce the large-amplitude vortex seen in our simulations. Below, we shall first review the method of Sagdeev et al.[25]. We shall then argue that a more general class of solutions than the ones used by Horton et al. must be considered, if we are to approximate the steady-state vortex of the sheath. We shall finally describe a simpler, periodic solution (Stuart’s solution), which at least provides a rough fit to the observed vortex parameters, leaving to future research a more detailed exploration of analytic solutions for the asymptotic states.

We now review the general procedure for obtaining localized solutions of the Navier-Stokes equation[31]. The first step is to assume a structure stationary in a reference frame moving with constant velocity $v_y = u$. To make the contact with Section 6.1, we write $u = -v_0$, where $-v_0$ is the

drift velocity of the vortex as seen in the simulations. Then, defining the transformed potential ψ through:

$$\phi(x, y, t) = -v_0x + \psi(x, y + v_0t) \quad (41)$$

we find that Eq.(21) reduces to the stationary form:

$$[\psi, \nabla^2\psi] = 0 \quad (42)$$

where the Poisson brackets denote the operator $[f, g] \equiv \partial_x f \partial_y g - \partial_y f \partial_x g$ [27]. To solve Eq.(42), one can then select a class of solutions for which:

$$\nabla^2\psi = f(\psi) \quad (43)$$

where $f(\psi)$ is a given function of ψ . If anything, Eq.(43) suffers from too much latitude in the possible choices of the function $f(\psi)$, which is essentially arbitrary in the form given above. To reduce the indeterminacy of Eq.(43), one can proceed by imposing additional constraints. The first simplification is to assume that $f(\psi)$ is linear, in the form:

$$f(\psi) = d + c\psi \quad (44)$$

where d and c are constants. This has the advantage of leading to an equation which is analytically solvable. The second constraint is to assume (43) valid only in a restricted region of the plane, say in a circle of radius $r = a$, and require that the solutions of (43) match to a prescribed laminar flow outside the region. Because of these constraints, many, if not all of the arbitrary constants in the solution of the interior region are then determined.

We have applied the method outlined in the preceding paragraph in two ways. In the first, we attempted to model the edge region by a monopolar vortex, symmetric about the inflection point of the shear layer. In the second, we attempted to fit a dipolar vortex[32] to the edge region, with the wall as symmetry plane between the two vortices in the dipole, and with one of the vortices a virtual image of the other one, resident in the plasma. In each case, the interior region of the vortex was modelled by Eq.(44) with $d = 0$ and $c = -k^2$, resulting in the Helmholtz equation:

$$\nabla^2\psi + k^2\psi = 0 \quad (45)$$

The matching condition at the boundary between the vortex interior and the unperturbed exterior flow then results in a “modon dispersion relation” for the internal wavevector k .

These approaches unfortunately failed, in that the solutions predicted vortices with small amplitudes, $e|\delta\phi|/T_i \ll 1$, in contradiction with the observed $e|\delta\phi|/T_i \sim 2$. The weakness of the vortices obtained in the analytic solutions was linked to our choice of the smallest root of the dispersion relation for k , this choice leading to a flow which closely approximates the external, unperturbed flow. By choosing the next, larger root, one does obtain a large-amplitude vortex, with $e|\delta\phi|/T_i \sim O(1)$. However, this choice also leads to strongly reversed flows[16], which do not resemble the circular flows seen in the simulation vortices.

We suspect that the failure of the method is tied to the choice of a linear function for $f(\psi)$, because such a choice does not produce solutions which are sufficiently “self-binding”. As an alternative, one might consider an exponential dependence in the function $f(\psi)$, with the *ansatz*:

$$f(\psi) \sim a \exp(b\psi) \quad (46)$$

For values of ψ of order unity, the exponential can provide the necessary curvature in the solution to ψ so that within a localized region, ψ can match to some external flow.

We have not attempted to solve Eq.(43) with the exponential dependence $f(\psi) \sim a \exp(b\psi)$ for a strictly localized solution. Rather, we have fallen back onto a periodic solution existing in the literature, which does satisfy Poisson’s equation with this form of $f(\psi)$. This is Stuart’s solution, which can be written:

$$\psi = \frac{v_0}{k} \log [\cosh(kx) + A \cos(ky)] \quad (47)$$

In Eq.(47), the wavenumber k is adjustable and determines the periodicity of the solution, with wavelength $\lambda = 2\pi/k$. The parameter A is also adjustable, with $A < 1$, and determines the maximum depth of the potential well. One can verify that the function ψ of Eq.(47) satisfies:

$$\nabla^2\psi = kv_0 \exp(-2k\psi/v_0) \quad (48)$$

This corresponds to a charge density with a strong dependence on the potential:

$$\rho(\psi) = -kv_0 \exp(-2k\psi/v_0) \quad (49)$$

Note that if we normalize x and ψ in Eq.(48) according to $\xi = kx$ and $\zeta = k\psi/v_0$, then Eq.(48) reduces to the simple, general form:

$$\nabla_{\xi}^2 \zeta = \exp(-2\zeta) \quad (50)$$

While Stuart's solution is an exact stationary solution of the Navier-Stokes equation, its choice is a rough physical guess insofar as it is not the exact consequence of the time-dependent problem. Keeping this spirit of approximation in mind, we shall now determine the free parameters in Stuart's solution by matching to the observed simulation results.

6.4 Periodic Solution for the Steady-State Vortex

Using Eq.(41), we transform the potential ψ of Eq.(47) back to the potential ϕ in the stationary laboratory frame:

$$\phi(x, y) = -v_0 x + \frac{v_0}{k} \log(\cosh(k(x-b)) + A \cos(k(y-v_0 t))) \quad (51)$$

In this equation, we have also chosen a new line of symmetry in x , by shifting the vortex centers to $x = b$. Note that Eq.(51) predicts $v_y(x) \rightarrow 0$ for $k(x-b) \gg 1$, and very roughly $v_y(x=0) \approx -2v_0$ at the wall. By inspection of Fig.(14), we find that the vortex center lies at $b = 16$ ($b/\rho_i = 2.5$). For the wavelength k , we have $k = 2\pi/L_y = 0.0245$ ($k\rho_i = 0.155$). The vortex velocity v_0 was already noted in Section 6.1, where it was found to be $v_0/v_{ti} = 0.44$.

To determine the remaining adjustable parameter A , we consider the maximum depth of the potential well along the line of symmetry, $x = b$. In physical units, this is:

$$\frac{e\delta\phi}{T_i} = -\frac{v_0/v_{ti}}{k\rho_i} \log\left(\frac{1}{1-A}\right) \quad (52)$$

or, solving Eq.(52):

$$A = 1 - \exp\left(-\frac{k\rho_i}{v_0/v_{ti}} \frac{e\delta\phi}{T_i}\right) \quad (53)$$

With the values derived above and $e|\delta\phi|/T_i \approx 2.4$, we find $A \approx 0.57$. To summarize, we have found that Eq.(51) gives a rough estimate for the steady-state vortex with the parameters:

$$v_0/v_i = 0.44 \quad k\rho_i = 0.155 \quad (54)$$

$$b/\rho_i = 2.5 \quad A = 0.57 \quad (55)$$

Let us examine some properties of Stuart's solution with these parameters. With $k|x-b| \gg 1$, Eq.(51) predicts the potential:

$$\phi(x, y) = -v_0x + \frac{v_0}{k} \log(\cosh(k(x-b))) \quad (56)$$

and hence the flow:

$$v_y(x) = \frac{\partial}{\partial y} \phi(x, y) = v_0 (\tanh(k(x-b)) - 1) \quad (57)$$

The analytic form of this flow is identical to that which we assumed for the initial conditions of the linear stability analysis of Section 5.2:

$$v_{0y}(x) = V_0 (\tanh(x/a) - 1) \quad (58)$$

provided we take $V_0 = v_0$. However, the final value of k observed in the simulation imposes a much broader scale length than the initial gradient length a , as we have $1/k = 6.5\rho_i$, which is much larger than $a = 0.4\rho_i$. From Eq.(51) we can obtain the total width in x of the separatrix. This is given by:

$$h = \frac{2}{k} \cosh^{-1}(1 + 2A) \quad (59)$$

We find that $h \approx 8\rho_i$, which is somewhat larger than the observed vortex diameter $l_x \approx 5\rho_i$. If we find this discrepancy disturbing, we should perhaps instead link the vortex size not to the extent of its separatrix, but to the scale-length of its y -averaged flow, which is somewhat sharper. Averaging over the y coordinate at any fixed x , we find that:

$$\bar{v}_y(x) = -v_0 - v_0 \frac{\sinh(k(x-b))}{(\cosh^2(k(x-b)) - A^2)^{1/2}} \quad (60)$$

With $A = 0.57$, we find that $\bar{v}_y(x)$ achieves 3/4 of its maximum value at a distance $l = 1.3\rho_i$ from the plane of symmetry. We shall now decree that this is the new scale-length for the shear layer, and that the line of symmetry has shifted in such a way as to accomodate it, by defining $b \equiv l \approx 1.3\rho_i$. For the parameters of Simulation 1, this yields $b \approx 8.1$, which is close to the observed value of the coordinate of the inflection point.

The value of A which we found above, $A = 0.57$, is comparable to that found when one fits the model of Eq.(51) to the simulation results of Corcos[20,21,22]. In a simulation of the Kelvin-Helmholtz instability, with a tanh profile for the shear layer similar to the one above, Corcos initially excited the mode with $ka = 0.45$. The saturated vortex which developed from the initial perturbation was seen to have a separatrix width satisfying $kh = 10.0$, which from Eq.(59) corresponds to $A = 0.45$.

Finally, to measure the vorticity extracted by the instability from the shear layer, we consider the circulation $\Gamma \equiv \int \omega dx dy$. The ratio of the total circulation in the model vortex of Eq.(51) to the initial circulation Γ_0 in a wavelength $2\pi/k$, is given by:

$$\frac{\Gamma_{vor}}{\Gamma_0} = \frac{4}{\pi} \tan^{-1} \sqrt{A} = 0.82 \quad (61)$$

so that the simulation results, and the analytic model for the vortices, are compatible with a situation in which most of the vorticity (and hence most of the net charge density in the shear layer) resides within the vortex separatrix.

6.5 Power Spectra

We shall now discuss the frequency and wavenumber dependence of the power spectra. As in Section 4.3 we consider the transforms of the potential $\phi(x, y, t)$ at a fixed x , located in the midplane of the simulation region, $x = L_x/2$, but we now transform in time as well as in y . More precisely, for each wavenumber k_y , the power spectrum $P(k_y, \omega)$ is defined as the Fourier transform in time of the autocorrelation function of the mode:

$$P(k_y, \omega) \equiv \int_{-\infty}^{\infty} d\tau e^{i\omega\tau} \langle \tilde{\phi}(k_y, t) \tilde{\phi}^*(k_y, t + \tau) \rangle \quad (62)$$

In Eq.(62) the average $\langle \dots \rangle$ is obtained by performing a time-average on the simulation data from the time-interval $0 \leq \omega_{ci}t \leq 1075$. The resulting autocorrelation function is also passed through a lag window[33], resulting in a smoothed spectrum.

Let us first consider the total spectral energy for each Fourier mode $\tilde{\phi}(k_y, t)$. This is simply:

$$\langle |\phi(\tilde{k}_y, t)|^2 \rangle = \int_{-\infty}^{\infty} \frac{d\omega}{2\pi} P(k_y, \omega) \quad (63)$$

In Fig.(19) we plot $\langle |\tilde{\phi}(k_y, t)|^2 \rangle$ and compare its values to $\langle |\tilde{\phi}(k_y, t)|^2 \rangle^{th}$, the distribution of energy in thermal equilibrium. The theoretical expression for the spectrum in thermal equilibrium is given by:

$$\langle |\tilde{\phi}(k_y, t)|^2 \rangle^{th} = \frac{T}{2\epsilon_0} \frac{k_{Di} L_y}{k_y^2} \left(1 - (1 + (k_y \lambda_{Di})^2)^{-1/2} \right) \quad (64)$$

which is obtained from the fluctuation-dissipation theorem, assuming an infinite, homogeneous plasma[34]. While Eq.(64) does not account for all numerical discreteness effects, nor for the boundedness of the system, we believe that it provides a qualitative estimate for the level of thermal fluctuations. The first notable feature of Fig.(19) is that the spectrum is peaked at low wavenumbers, and is strongly cutoff beyond $k_y \rho_i = 1$, a feature already observed in Fig.(7), where we showed a snapshot of modal amplitudes. The second distinctive feature of Fig.(19) is that the values of the power spectrum are quite larger than those of the thermal spectrum over a large range of wavenumbers, up to $k_y \rho_i \approx 3$. This latter feature indicates that despite their smaller amplitudes (as compared to the $e\phi/T_i \sim 1$ vortices), the short wavelength-modes are also collective plasma oscillations, and cannot be assimilated with the thermal fluctuations.

We shall now consider the power spectra in more detail, as a function of frequency ω . In Figs.(20) we have plotted the spectra $P(k_y, \omega)$ for the first 7 wavenumbers (omitting $k_y = 0$), covering the range $0.155 \leq k_y \rho_i \leq 1.085$. A first feature of these figures is that in each graph, the spectrum peaks at a different value of ω , $\omega \equiv \omega_P$, suggesting a dispersion relation of the form $\omega_P = \omega(k_y)$. Now, if the modes are simply static structures, carried along at the vortex speed $v_y = -v_0$, then we should have the dispersion relation:

$$\omega = -k_y v_0 \quad (65)$$

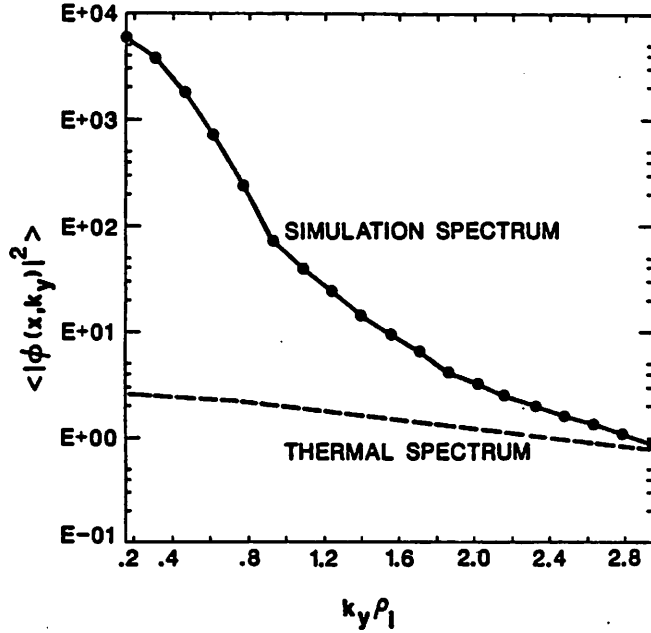


Figure 19: Power spectrum for Run 1, time-averaged over $0 \leq \omega_{ci}t \leq 1500$ (full line). We have also plotted the estimated thermal spectrum (dashed line). All data is taken along the y cross-section at $x = L_x/2 = 16$.

In Fig.(21), we compare this dispersion relation to the values of $\omega_P(k_y)$: we can see that the agreement is reasonably good. Let us note a second, qualitative feature of Fig.(21), which we believe reveals a fundamental aspect of the edge turbulence: this is the progressive broadening of the spectra as we move to larger $k_y \rho_i$. While the modes with $k_y \rho_i \ll 1$ have a spectrum which is both narrow and confined to $|\omega| \ll \omega_{ci}$, the modes with $k_y \rho_i \sim 1$ have a broad spectrum, with peak near ω_{ci} and with width $|\Delta\omega| \sim \omega_{ci}$. There is also more structure in the short-wavelength modes, with the amplitude of many sidebands comparable to that of the main peak.

These qualitative observations on the structure of the spectra suggest that the edge fields can be partitioned into two physically distinct components, which can be described as follows:

1. There is a “coherent” component of the fields, with $|k_y| \rho_i \ll 1$ and $|\omega| \ll \omega_{ci}$, corresponding to the large and stable structures seen in the plasma – the vortices. This component arises out of the inverse cascade of wavenumbers which occurs during the transient build-up of the system.

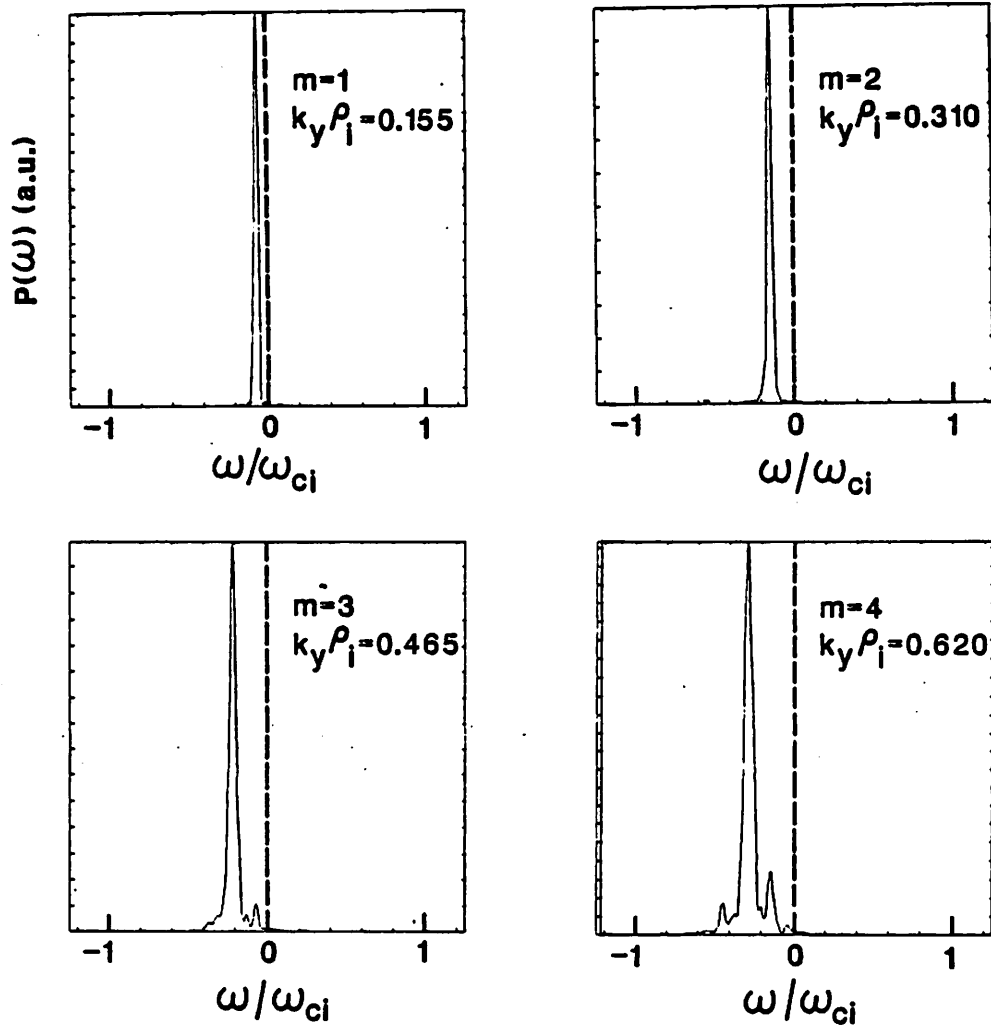


Figure 20: Power spectra in Run 1, time-averaged over $0 \leq \omega_{ci}t \leq 1500$, for Fourier modes $m = 1$ to 4; all data is taken along the y cross-section at $x = L_x/2 = 16$ (continued on the next page).

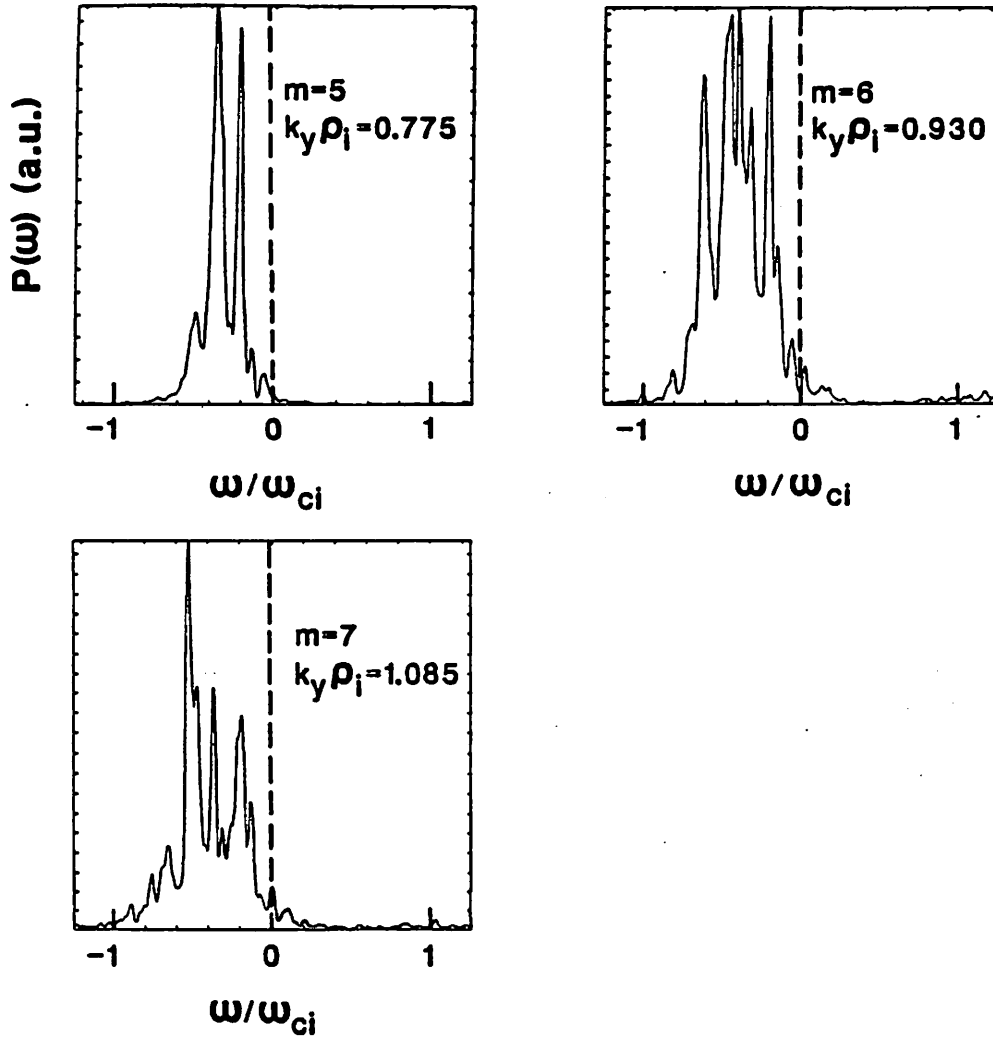


Figure 20: (continued from the previous page) Power spectra in Run 1, time-averaged over $0 \leq \omega_{ci}t \leq 1500$, for Fourier modes $m = 5$ to 7 ; all data is taken along the y cross-section at $x = L_x/2 = 16$.

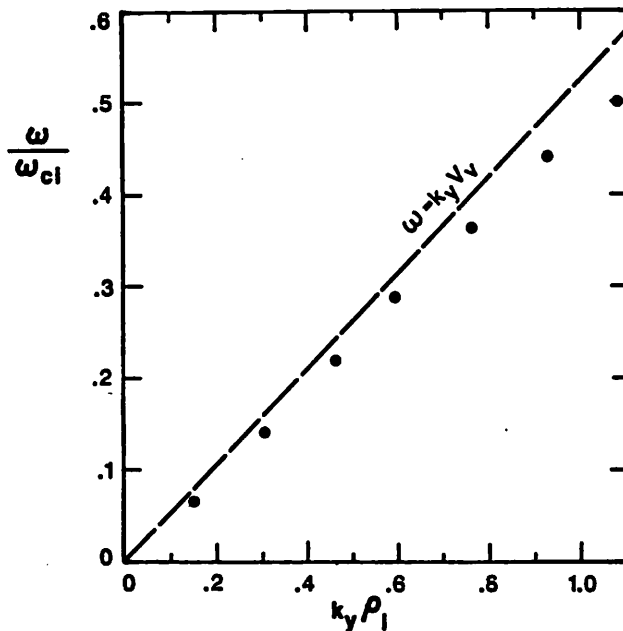


Figure 21: Dispersion relation obtained from Figs.(20); the dashed line denotes the linear dispersion relation $|\omega| = k_y |v_0|$ where $v_0 = -0.44v_{ti}$ is the vortex velocity.

2. There is also a “turbulent” component of the fields, with $|k_y| \rho_i \sim 1$ and $|\omega| \sim \omega_{ci}$, corresponding to the small, short-lived fluctuations. This component arises out of a forward cascade of wavenumbers, which we shall qualitatively discuss in the next section.

The partition scheme outlined above is based on qualitative considerations which we have adopted in the absence, on our part, of a more precise theoretical understanding. In Section 7.5, we shall nonetheless use this scheme to estimate diffusion coefficients, thereby obtaining at least semi-quantitative results. We leave to future research the development of a more quantitative understanding of the mechanisms underlying the edge turbulence.

6.6 Source of the Short-Wavelength Fluctuations

What are the mechanisms underlying the partition of the edge turbulence into a spectrum with a mixture of coherent and turbulent components? The answer is related to that of general problems in two-dimensional turbulence,

in particular to the organization of forward and inverse cascades of energy in wave-number space. Thus, we fear that a quantitative answer to the question probably requires a range of investigation largely outside the scope of the present paper. However, in keeping with the spirit of the analysis of the previous sections, we shall at least suggest some mechanisms by which the short wavelength, “turbulent” components can arise in the system.

Our point of view is that the quasi-stable vortex state observed in the simulations can be regarded in a first approximation as a completely stable steady-state of the form given by Eq.(51). The problem is then to predict how short-wavelength ($k_y \rho_i \sim 1$), high-frequency ($\omega \sim \omega_{ci}$) fluctuations can arise from such a nonlinear equilibrium state. The analysis is complicated by at least two general factors. The first is that the equilibrium state is itself a nontrivial, nonlinear solution to the cross-field equations, and, for instance, linearizing about this state is a procedure greatly complicated by the specific vortex geometry. The second factor of complication arises because we are considering a regime for which the fluid equations are no longer valid, and thus the full kinetic description is presumably necessary. At the very least, an equation of the form of Eq.(38) (but with a rigorous derivation of FLR effects to order $(k\rho_i)^2$) will have to be considered.

Within the general context just outlined above, we shall be content to suggest the following mechanisms for the excitation of the short-wavelength fluctuations:

1. Instabilities in the shear layer outside of the vortex: As we saw in Figs.(4), every now and then “satellite vortices” are generated at some distance from the main vortex and subsist for a time period $\omega_{ci}t \sim 100$. This suggests a continuous generation of small-wavelength modes at some distance from the main vortex; presumably these modes are then convected up and down the shear layer relative to the main vortex, and eventually merge with it.
2. Instabilities inside the main vortex: In viscous hydrodynamics, large eddies are rarely absolutely stable, and are seen to generate smaller eddies through viscous shear. This suggests that we investigate the stability of the vortex to radial eigenmodes with angular dependences of the form $e^{im\theta}$. As we shall see in Section 7.1, the bounce frequency of electrons at the bottom of the potential well of the vortex is of order

$\omega_B \approx 0.5\omega_{ci}$. The excitation of modes at harmonics of this frequency could account for the presence of the high frequency fluctuations.

3. Trapped-electron instabilities: The presence of trapped electrons in the vortices suggests the possibility of sideband instabilities as studied by Kruer and Dawson[35] in connection with large-amplitude plasma waves.
4. General parametric instabilities: Rather than consider the stability of a linearization around the vortex equilibrium, we can consider the more general question of the stability of arbitrary three-wave processes. In particular, there is the possibility of three-wave coupling to the $k_y = 0$ mode, a process analysed in connection with drift waves[36].

7 Transport

An essential feature of the dynamics of the cross-field sheath is the existence of an outward, ambipolar transport of particles. In the steady-state, this transport is nearly constant in time, and equal to the net influx due to pair creation. What is the driving mechanism of this transport? In the previous section, we saw that the power spectrum could be roughly partitioned into two qualitatively different contributions: a long-wavelength, “coherent” component, which is associated with the long-lived vortices; and a short-wavelength “turbulent” component, associated with the short-lived fluctuations which satisfy the condition $|k_y| \rho_i \sim 1$. To this spectrum, we must add an overall thermal background, due to the excitation of waves by the discrete particles. In the present section, we shall estimate the contribution to transport from each of these components.

The “coherent” component of the fields is composed of the large, long-lived vortices. Its representation is that of a uniformly drifting, constant-amplitude vortex of the form:

$$\phi^{coh}(x, y, t) = \Phi(x, y - ut) \quad (66)$$

where $u = -v_0$ is the vortex drift-velocity. Let us consider the effect of (66) on transport. First, because of the functional dependence of Φ , we can transform to a reference frame co-moving with the vortex, in which the potential becomes strictly static. Thus, we need only consider the effect of the time-independent potential $\Phi(x, y)$.

Let us first consider the effect of $\Phi(x, y)$ on the ion motion. On account of their large gyro-radii, the ions would appear to be *a priori* the least well-confined species. Furthermore, a potential such as (66) can in principle create outward transport, by moving the ions in intrinsically stochastic orbits. This judgment is based on the observation that the ion gyroradius is an appreciable fraction of the vortex size ($\rho_i/l_x \sim 1/5$), suggesting that the adiabaticity of the ion $\mathbf{E} \times \mathbf{B}$ drifts is destroyed in the presence of the vortices, with stochastic motion as a result. Of course, a quantitative analysis of such a transport mechanism requires rigorous Hamiltonian methods, as for instance in [37]. However, we would like to argue that such an analysis of ion transport is not immediately necessary, because, without a concomitant outward electron flow, whatever outward ion flow

might occur through intrinsic stochasticity is strictly self-limiting. This is because, as the ions are driven to the wall, they build-up a positive charge on its surface, which eventually forms an impassable potential barrier. It is not hard to estimate that the required electric field for stopping almost all ions is of order $E_x/B_0 \sim v_{ti}$ (see Eq.(104)).

Now, for the electrons, there is almost no outward transport in the presence of the potential $\Phi(x, y)$. If $\Phi(x, y)$ is rigorously time-independent, then the electron orbits will remain regular (because $\rho_e \ll l_{vortex}$). Through their $\mathbf{E} \times \mathbf{B}$ motion the electrons will closely follow the equipotentials $\Phi(x, y)$ at all times, and the great majority of electrons will remain forever confined, by being locked onto a given equipotential. The exception will be for those electrons on equipotentials which come close to the wall, within a layer of width ρ_e , within which the finite electron gyro-radius enables them to strike the wall. However, this class of equipotentials defines a "scrape-off" layer which is still very narrow compared to the system size, and whose existence does not explain the outward transport of electrons which are at a distance $x > \rho_e$ from the wall.

Thus, we must conclude that by itself, the "coherent" component of the spectrum is unable to induce transport. Furthermore, the arguments given above suggest that this situation is primarily due to the lack of electron mobility. While it appears that the ions might have an intrinsic diffusion tied to their stochastic orbits, the requirement of ambipolarity automatically suppresses their outward transport, whenever the electrons themselves remained confined. Thus, the electrons form a "bottleneck" in transport. In what follows, we shall therefore concentrate on the electron diffusion as the dominant transport mechanism, inducing loss of particles of both species: we shall assume that the ions easily "follow the electrons", and that their outward flux is simply equal to the independently determined electron flux.

The failure of the coherent part of the spectrum to induce transport suggests that the turbulent component of the spectrum plays the central role, by creating an effective collisionality, resulting in a diffusion. Because of the short-wavelength nature of the fluctuations, we suspect that this diffusion coefficient is of a local nature, resulting from scattering events over a length scale of order ρ_i or smaller. However, we should note that in such a situation, the coherent spectrum might still have a sizeable effect. This consideration arises because though the coherent spectrum does not induce transport by itself, it might enhance this diffusion, by behaving as

a convection cell. In this latter scenario, transport is enhanced because the vortex can ferry particles from the interior to regions much closer to the wall, on a time-scale shorter than the global diffusion time in the presence of only the fluctuations.

An important question to be first decided is whether the dominant source of transport is due to the turbulent collective modes, or whether it is a consequence of collisional effects. We shall consider this question in Section 7.4, where we show that the scaling of transport in the system is not collisional. However, we shall first present some numerical measurements of transport as obtained in Run 1.

7.1 Orbits of Test Particles

In order to gauge the rate of transport of particles across the system, we set up a numerical experiment in which we followed the motion of a set of test particles, composed of five electrons and five ions which were initially placed at the bottom of the vortex. In Fig.(22a), we show the initial particle positions at $\omega_{ci}t = 1075$. We followed the motion of the particles over the time interval $1075 \leq \omega_{ci}t \leq 1575$, the final positions being shown in Fig.(22b). The test particles moved in response to the electric fields in the simulation region, but were completely passive, in that they did not in turn affect the fields through Poisson's equation. Thus, their presence did not modify the dynamics of the system. Furthermore, in order to follow as closely as possible the guiding-center motion of the electrons, we introduced an unphysical damping in the mover of the test electrons[38], which suppressed gyro-motion, and retained only the guiding-center motion. As we shall see, a consequence of this modification of the mover is that the test electrons remain in the system much longer than the field electrons, because they have to move closer to the wall to be scraped-off. A rough indication of the better confinement of the test electrons can be seen in Fig.(22b), which shows that while by $\omega_{ci}t = 1575$ most of the ions have impacted into the wall, most of the electrons are still confined. Without the damping of their gyro-motions, the test electrons are lost at the same rate as the test ions.

In Figs.(23), we show the time histories of the x coordinates of the five test electrons, with a blow-up of the motion of Electron 1 shown in Fig.(24). The plots show that all electrons are initially trapped at the

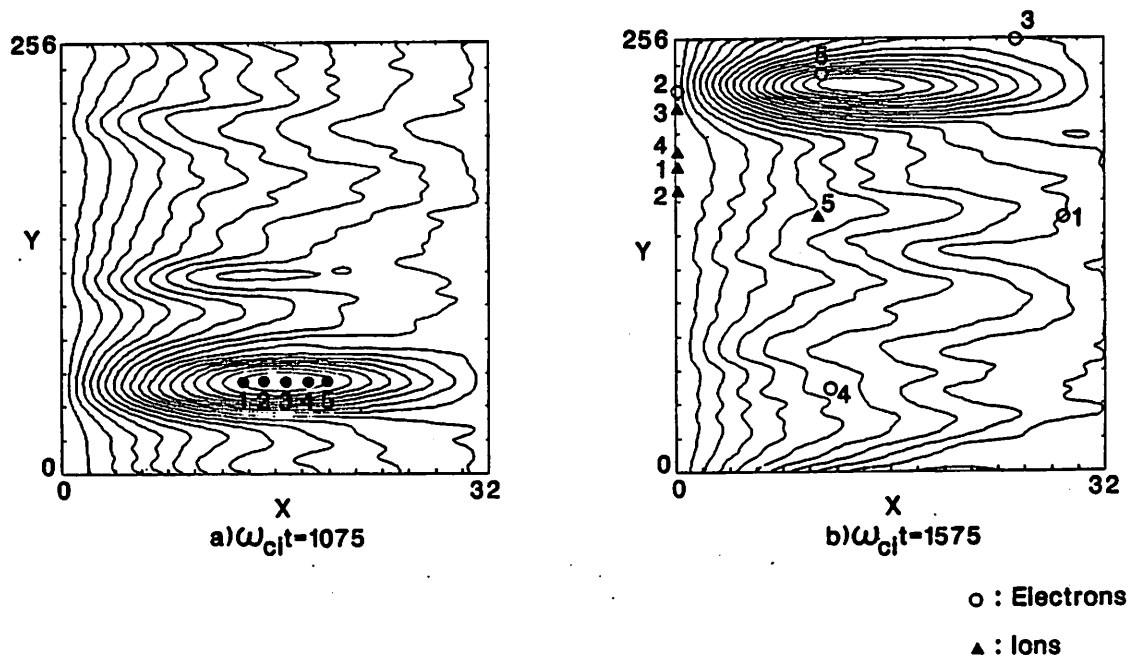


Figure 22: Positions at two different times of a set of test particles, five electrons and five ions, in Run 1. These are superposed on the corresponding equipotential contours; (a) $\omega_{ci}t = 1075$, initial positions of the particles, with electrons and ions superposed; (b) $\omega_{ci}t = 1575$; final positions, including the particles which have impacted into the wall.

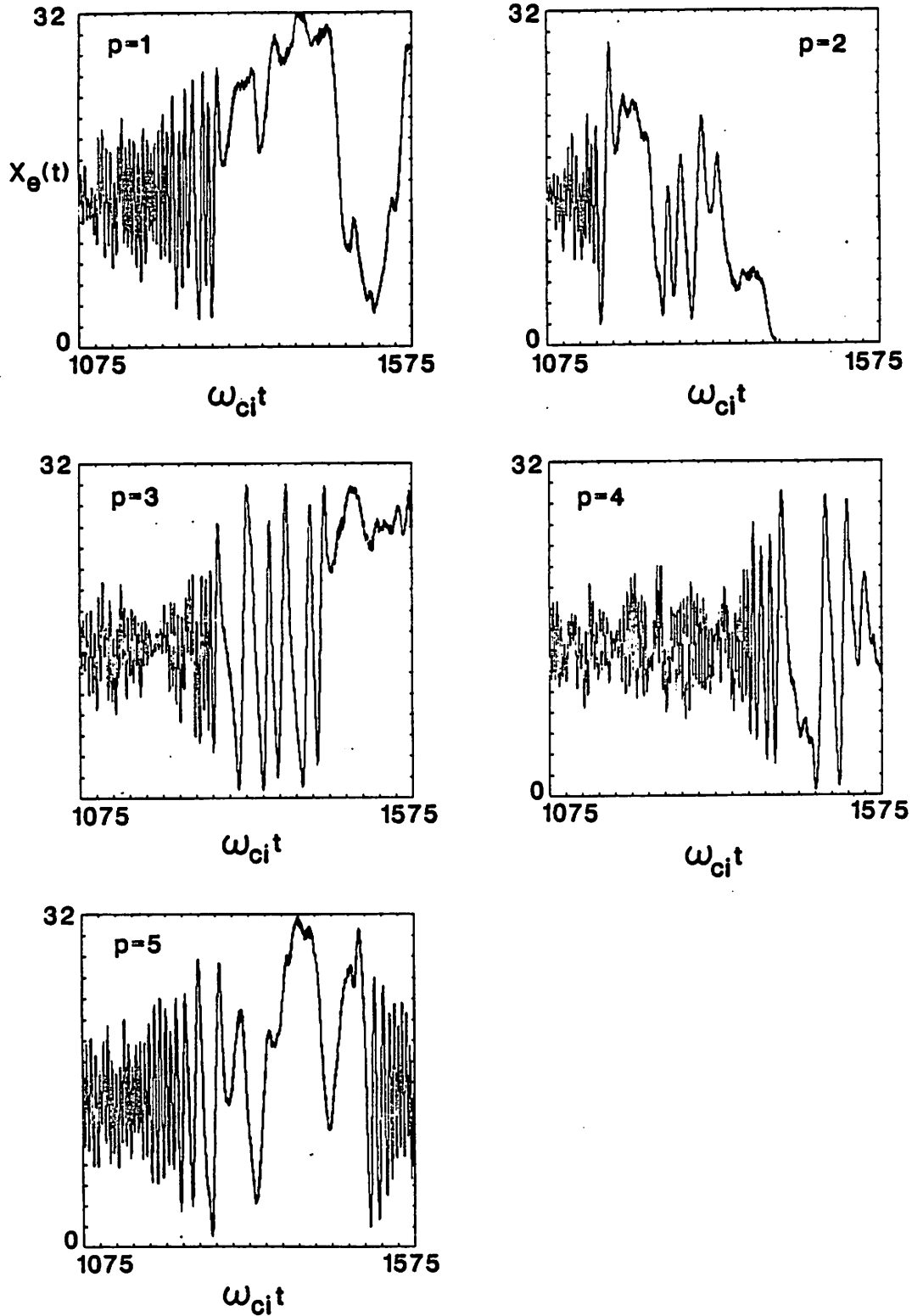


Figure 23: Histories of $x_e(t)$ for the five test electrons of Fig.(22) (labelled $p = 1, 2, \dots, 5$); $1075 \leq \omega_{ci}t \leq 1575$, Run 1.

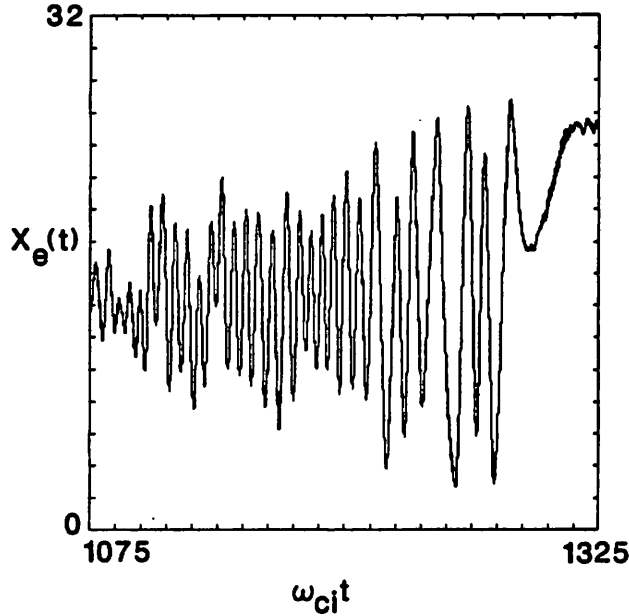


Figure 24: Enlargement of the time-history of $x_e(t)$ for electron 1 of Fig.(23); $1075 \leq \omega_{ci}t \leq 1325$, Run 1.

bottom of the vortex, and remain trapped for a considerable number of bounce oscillations. From Fig.(24), we can estimate the bounce frequency of the electrons near the bottom of the vortex; it is found to be:

$$\omega_{B2} = 0.5\omega_{ci} \quad (67)$$

This estimate is to be compared with that of Eq.(40), $\omega_{B1} = 0.25\omega_{ci}$, in which we evaluated ω_B from the measured values of the $\mathbf{E} \times \mathbf{B}$ drift inside the vortex. As ω_{B1} was evaluated for a particle roughly half-way up the potential well, it is not surprising that $\omega_{B2} > \omega_{B1}$, indicating faster bounce oscillations at the very bottom of the vortex.

Figs.(23) show that over many bounce oscillations, the electrons become progressively untrapped, by migrating toward the separatrix of the vortex. Thus, $x_e(t)$ exhibits larger vertical excursions as time progresses, and the bounce oscillations slow down towards the end of the duration of the trapped orbits. After reaching the separatrix, the electrons become untrapped, and then undergo several kinds of motion: for instance, Electron 1 begins to execute large excursions across the system, over a time-scale $\omega_{ci}t \sim 100$; Electron 2 is almost immediately driven to the wall; Electron 5

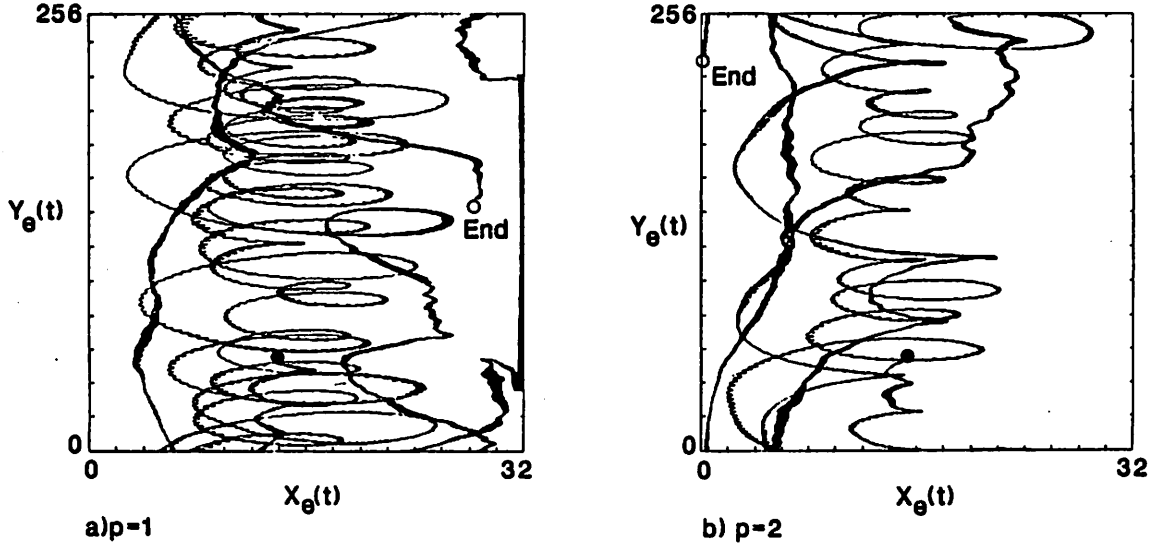


Figure 25: Parametric plots of $(x_e(t), y_e(t))$ for electrons $p = 1, 2$ of Figs.(23); $1075 \leq \omega_{ci}t \leq 1325$, Run 1.

first behaves as Electron 1 and displays large excursions across the system, but is eventually retrapped by the vortex at $\omega_{ci}t \approx 1450$. Note that in almost all cases, the electrons are driven within a distance ρ_e of the wall, and without the damping of their gyro-motion would have been scraped-off from the plasma.

In Figs.(25) we show parametric plots of the electron position $(x_e(t), y_e(t))$, so as to give a general feeling for the electron motion. In these figures, one can distinguish the trapped, oscillating orbits, from the relatively straight, untrapped trajectories.

In Figs.(26), we show the motion of test Ion 1, by plotting the time histories of $x_i(t)$, $y_i(t)$ and $(x_i(t), y_i(t))$. Though the ion is initially trapped in the vortex, as can be seen in Fig.(26a), its motion when trapped is less distinctive than for the electrons. Thus, in Fig.(26c) we do not see the great loops that were seen in Figs.(24). This is because the large gyro-orbit of the ion blurs the motion of the guiding-center, and also, presumably destroys its exact $\mathbf{E} \times \mathbf{B}$ drift. A distinctive feature of Fig.(26c) is the repeated repulsion of the ion by the strong electric field in the sheath; this is seen as a set of almost point-like reflections of the ion orbit.

While Figs.(23) will provide us in Section 7.3 with an estimate of the

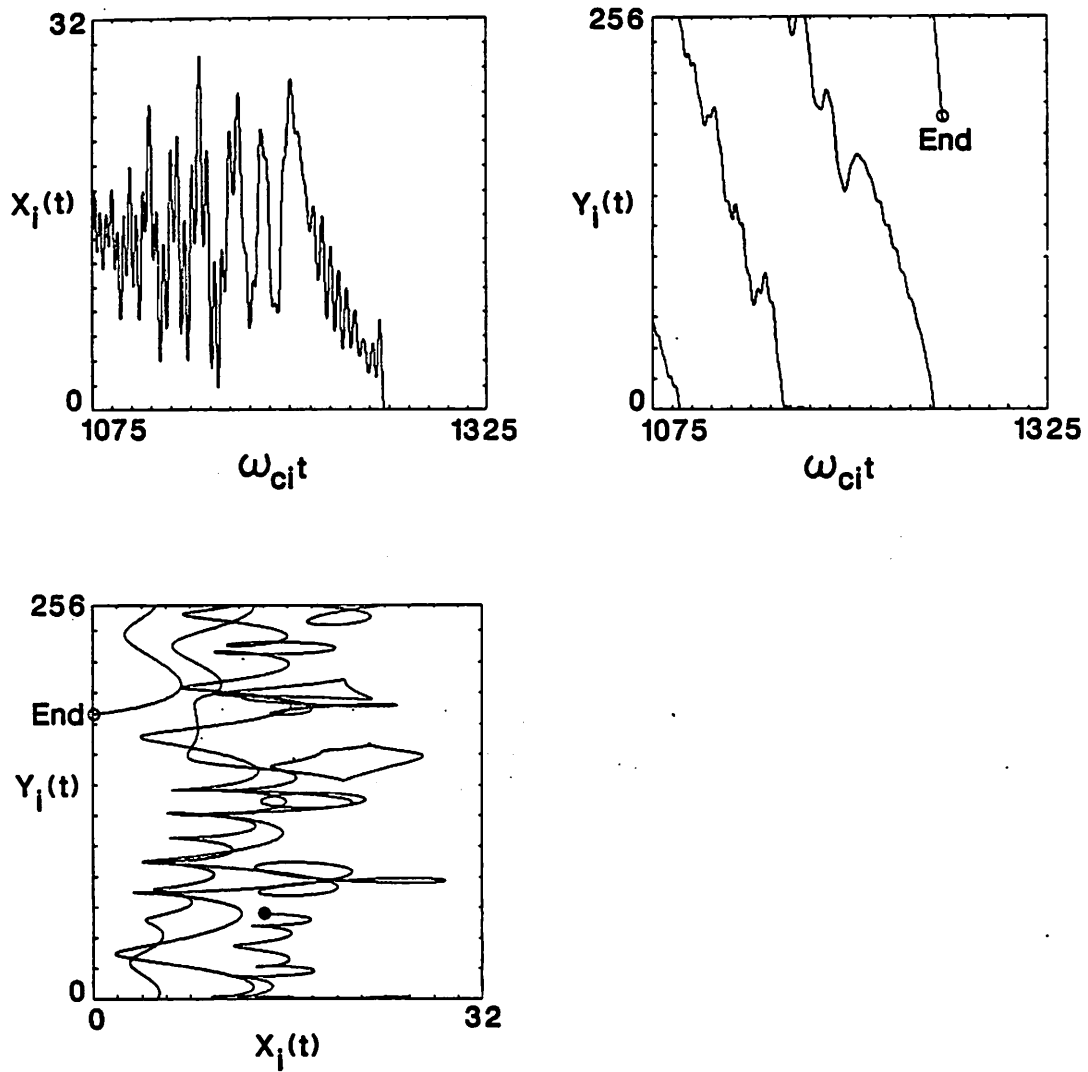


Figure 26: Orbits of test Ion 1 of Figs.(22); $1075 \leq \omega_{cit} \leq 1325$, Run 1.

average global diffusion time, they do not indicate in which specific regions transport is greatest. We can, however, obtain an indication of this from the scatter plots of Figs.(16). A striking feature of these scatter plots is the existence of a large region on the underside of the vortex, which is almost evacuated of particles, and which lies along the vortex separatrix. We believe that the evacuated regions in Figs.(16) are formed when particles which are $\mathbf{E} \times \mathbf{B}$ drifting counter-clockwise around the vortex impact into the wall, at a point at the level of the vortex center. The result is a depletion of the region on the underside of the vortex: thus, the evacuated regions can be considered to be the “wake” inside the plasma, of the scrape-off of particles right at the wall. Not surprisingly, the existence of the evacuated regions indicates that particle orbits are most unstable on the separatrix, a generic feature of dynamical systems[39]. This is also qualitatively confirmed in Figs.(23): we can see that an electron moving right on the separatrix will have, at intervals of a bounce period, many opportunities for grazing the wall (this is particularly clear for Electron 3).

7.2 Dynamics without Electron Gyromotion

The results of the previous section, in which we saw that by itself, the $\mathbf{E} \times \mathbf{B}$ motion of the test electrons can lead to diffusion and loss of confinement, suggested that we run a simulation in which the gyro-motion of *all* electrons was suppressed, so as to demonstrate that only the $\mathbf{E} \times \mathbf{B}$ motion of the electrons is important. This notion is certainly reasonable, in view of the low-frequency nature of the spectra shown in Figs.(20), in which the spectra were confined to frequencies $|\omega| \ll \omega_{ce}$.

To run a simulation with suppressed gyromotion, and yet maintain a steady-state loss of electrons to the wall, we had to re-introduce an effect of the finite gyroradius by creating an artificial scrape-off layer, defined by requiring that all electrons within a fixed distance $x < \rho_e$ be immediately absorbed by the wall. With this modification, we ran a simulation of a system half as long as in Run 1, with $L_y = 128$ and half the injection rate, but with otherwise identical parameters. The results were qualitatively very similar to those of Run 1, with the system establishing large-amplitude, steady-state vortices ($e|\delta\phi|/T_i \sim 2$), and with a transport which maintained the particle densities at values very close to those in Run 1 ($n_{e,i} \approx 2.1$ peak densities, with similar density profiles). The structure of

the shear layer was also very similar to that found in Run 1.

These results indicate that $\mathbf{E} \times \mathbf{B}$ motion dominates the electron dynamics, and suggest that future simulation studies incorporate an electron mover which entirely ignores the gyromotion and follows only the $\mathbf{E} \times \mathbf{B}$ motion of the guiding centers. This modification should result in a considerable reduction in the computation times (in the simulation above, we merely damped the gyromotion, and were still limited by constraints of the explicit time step).

7.3 Numerical Estimates of the Diffusion Coefficient

We shall now estimate the diffusion coefficient using several different measures of transport. Our approach is qualitative, and aims for an estimate of the average diffusion rate across the system.

From Figs.(23), we can estimate a characteristic, “diffusive” time τ_{diff} for the diffusion of an electron inside the vortex. We define τ_{diff} as the time required for an electron to migrate to the separatrix. Averaging over the five test electrons, we find:

$$\omega_{ci}\tau_{diff} = 215 \quad (68)$$

Note that this is the time for the diffusion of an electron across the vortex radius, or a distance roughly $L_x/2$. We can now compare τ_{diff} to a global “confinement time” τ_{loss} , where we define τ_{loss} to be the average time any one electron spends in the system. Thus, in the steady-state, where rate of creation equals outward flux, we must have $s = N_e/\tau_{loss}$, where s is the electron-ion pair creation rate, and N_e the total number of electrons. With the known steady-state values $N_e = 16400$ and $s = 1.005$, we immediately find:

$$\omega_{ci}\tau_{loss} = 410 \quad (69)$$

Thus, we find that τ_{loss} is comparable to τ_{diff} , but somewhat greater, with $\tau_{loss}/\tau_{diff} = 1.9$. This disparity is not surprising, insofar as τ_{loss} accounts for the migration of particles across the entire system, while τ_{diff} was an estimate for their diffusion across roughly half the distance (and only in the well of the vortex).

From the diffusion time given in Eq.(68), we can in turn estimate the diffusion coefficient. Since τ_{diff} is the time for diffusion across a distance $L_x/2$, we have the estimate:

$$D_x^{diff} = \frac{(L_x/2)^2}{2\tau_{diff}} \approx 0.015 \quad (70)$$

where the superscript indicates an estimate based on test-particle diffusion. How does the value given above compare to the Bohm diffusion coefficient? The latter coefficient is given by:

$$D_x^B = \alpha \frac{T_i}{eB} = \alpha \frac{v_{ti}^2}{\omega_{ci}} \quad (71)$$

where $\alpha \approx 1/16$ [40]. With the values given in Table 1, we find that $D_x^B \approx 0.0625$, so that $D_x^{diff}/D_x^B \approx 1/4$.

We can independently estimate the diffusion coefficient by requiring that the solution of the diffusion equation be compatible with the observed density profile. The diffusion equation is given by:

$$\frac{\partial}{\partial t} n(x, t) = D_x \frac{\partial^2}{\partial x^2} n(x, t) + \sigma \quad (72)$$

where $\sigma = s/L_x L_y$ is the distributed source term and $n(x, t)$ the y -averaged particle density. We solve Eq.(72) in the steady-state ($\partial n/\partial t = 0$), with boundary conditions $n(x=0) = 0$ and $\partial n(x=L_x)/\partial x = 0$. The resulting solution is the parabolic profile:

$$n(x) = \frac{\sigma}{2D_x} x(2L_x - x) \quad (73)$$

With the peak density known from the simulation ($n(L_x) \approx 2.4$ at $\omega_{ci} t = 700$, see Fig.(15)), we find the diffusion coefficient:

$$D_x^{dens} = \frac{\sigma L_x^2}{2n(L_x)} \approx 0.026 \quad (74)$$

where the superscript indicates that D_x^{dens} is derived from the density profile. The rough agreement between the estimates of Eqs.(70) and (74) indicates that our calculations are consistent. The result $D_x^{dens} > D_x^{diff}$ suggests that particles injected at random in the system diffuse outward

faster than those injected right in the center of the vortex, but that the disparity in diffusion times is not very large.

7.4 Estimate of Discrete-Particle Effects

We shall now gauge the importance of collisional effects in the cross-field transport.

Like real particles, the numerical particles undergo scattering and diffusion from two sources of discrete-particle interactions: short-range binary collisions, and transport by long-wavelength, thermal fluctuations. In our range of parameters, it can be estimated that the $\mathbf{E} \times \mathbf{B}$ motion induced by the thermal background is the dominant contribution to the electron diffusion[41] (this is because $\rho_e \ll \lambda_{de}$). The resulting two-dimensional diffusion coefficient is, in physical units[42,41]:

$$D_x^{coll} = \beta \frac{(T/eB)}{(n\lambda_D^2)^{1/2}} (1 + \omega_{pi}^2/\omega_{ci}^2)^{-1/2} \log(k_{max}L/2\pi) \quad (75)$$

In Eq.(75), the numerical value of the constant β remains uncertain. The factor β is a constant which accounts for precise definitions of correlation times, and for numerical smoothing effects, factors which are not accurately determined in the analytic derivation of Eq.(75). The essential feature of Eq.(75) is, however, the strong dependence of the collisional diffusion coefficient on $n\lambda_d^2$. If the transport in Run 1 is mostly collisional, then changing the plasma “graininess” parameter $n\lambda_d^2$, while keeping the other plasma parameters fixed, should result in strong changes in the diffusion coefficient, and hence in markedly different steady-state conditions: thus, we have a test for determining whether the transport predominantly collisional.

With the steady-state parameters of Run 1, $\omega_{pi}/\omega_{ci} = 1.2$, $T_i/eB = 1$, and a numerically imposed $k_{max} = 0.23\pi/\Delta y$, we find the estimate for the collisional diffusion coefficient:

$$D_x^{coll} = \frac{2.24\beta}{\sqrt{n\lambda_d^2}} \quad (76)$$

where we have left $n\lambda_d^2$ a variable parameter. In order to test the applicability of Eq.(76), we performed a series of simulations in which we varied $n\lambda_d^2$, but kept ω_{ce} and ω_{ci} fixed, and in which we also kept the same creation

of charge per unit time from one simulation to the next. This was done by changing the electric charge and mass per numerical particle (which were made bigger to decrease $n\lambda_d^2$), while keeping e/m_e , m_e/m_i and the rate of injection of charge $e \times s = (\text{Charge per particle}) \times (\text{Rate of pair creation})$ fixed. In each simulation, we determined the diffusion coefficient from Eq.(74):

$$D_x^{num} = \frac{\sigma L_x^2}{2n(L_x)} \quad (77)$$

where $n(L_x)$ is the central, y -averaged steady-state density. The results are shown in Fig.(27) (Run 1 corresponds to $\sqrt{n\lambda_d^2} = 7.5$). In Fig.(27), it can be seen that the observed diffusion coefficient does not have the collisional dependence implied by Eq.(76). In fact, despite strong variations in $n\lambda_d^2$, we obtained steady-states with very similar final density profiles and very similar values of the density-dependent parameters ω_{pe} and ω_{pi} . Only at the smallest value of $n\lambda_d^2$, $n\lambda_d^2 = 4$, do we begin to see indications of enhanced diffusion. The vortex structures also remained qualitatively the same, but became noisier at the smaller values of the plasma parameter. These results lead us to believe that collisional effects are not the dominant transport mechanism in our simulations.

7.5 Analytic Estimate of the Diffusion Coefficient

In the previous sections we have argued that the large vortices cannot account directly for transport in the system, and that this transport does not scale as would be expected from collisional effects. These results suggest that the *turbulent* component of the edge spectrum is the main source of transport, and, in this section, we shall estimate its contribution to the diffusion coefficient.

We shall make several simplifying assumptions. We assume that in the steady-state the sheath organizes itself so as to have a thickness l_x , and that the vortices have an average spacing in y of l_y , with diameter l_v . We write:

$$l_y = c_1 \rho_i \quad (78)$$

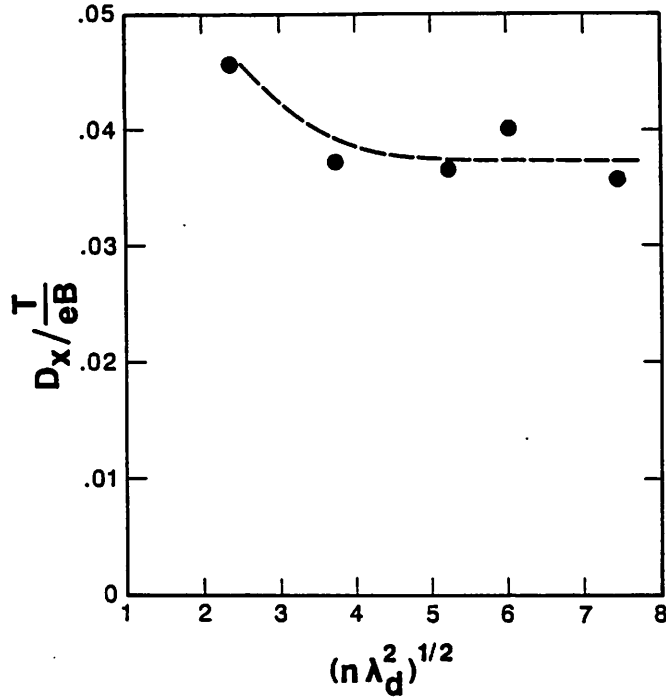


Figure 27: Dependence of the diffusion coefficient on the plasma parameter $n\lambda_d^2$; Run 1 has $(n\lambda_d^2)^{1/2} = 7.5$.

$$l_v = c_2 \rho_i \quad (79)$$

where c_1 and c_2 are dimensionless constants. We have already seen that $l_v \approx l_x \approx 5\rho_i$, so that $c_2 \approx 5$, and we expect that l_y will be somewhat larger than the system length in Run 1, so that $c_1 \geq 40$. We also assume that each vortex has an average depth $-\phi_{max}$, such that:

$$\phi_{max} = c_3 \frac{T_i}{e} \quad (80)$$

where c_3 is another dimensionless constant, with $c_3 \approx 2$. In what follows, we shall assume that the edge turbulence is independent of the edge density, at least when $\omega_{pi} \geq \omega_{ci}$. This assumption is motivated by the observation that the cross-field equations (17,18) appear to be weakly dependent on density when either $\omega_{pi} \gg \omega_{ci}$ or $\omega_{pi} \ll \omega_{ci}$, because in both limits we recover the two-dimensional Navier-Stokes equation. As a consequence, we take the constants c_1 , c_2 and c_3 , as well as other parameters characterizing the edge turbulence, to be density-independent. Note also that by scaling all lengths to the gyro-radius as in Eqs.(78,79), and the peak amplitudes to the ion

thermal energy as in Eq.(80), we have essentially stated all dependence on magnetic field and temperature as well.

Let us now consider the edge spectrum at some fixed x , say $x = l_x/2$. We shall assume that the spectrum has a universal dependence on wavenumber which is expressed by:

$$\langle |\tilde{\phi}(k_y)|^2 \rangle = A(k_y \rho_i) \langle |\tilde{\phi}(0)|^2 \rangle \quad (81)$$

where A is a continuous function, with $A(0) = 1$, which decreases rapidly when $|k_y| \rho_i > 1$. In Eq.(81), we have the Fourier transform:

$$\tilde{\phi}(k_y) = \int_0^{l_y} \phi(y) e^{-ik_y y} dy \quad (82)$$

In particular, we have the estimate:

$$\langle |\tilde{\phi}(0)|^2 \rangle = \langle \left[\int_0^{l_y} \phi(y) dy \right]^2 \rangle \approx (\phi_{max} l_y)^2 = \left(\frac{c_2 c_3}{c_1} \right)^2 \left(\frac{T_i}{e} \right)^2 l_y^2 \quad (83)$$

Now the diffusion coefficient for turbulent x -directed transport is given by the integral over the velocity autocorrelation function:

$$D_x^{turb} = \int_0^\infty \langle v_x(0) v_x(t) \rangle dt \quad (84)$$

where $v_x(t)$ refers to the velocity of a test particle. At a given (y, t) , the x -component of the electron velocity is given by:

$$v_x(y, t) = -\frac{E_y}{B} = \frac{1}{l_y} \sum_{k_y} i k_y \tilde{\phi}(k_y, t) e^{ik_y y} \quad (85)$$

Introducing (85) into Eq.(84), we can then decompose the diffusion coefficient into a sum over the contributions from separate modes. In evaluating (84), we simplify the integration over time by introducing a correlation time for the interaction of an electron with a given wavenumber:

$$\tau_c(k_y) = \omega_{ci}^{-1} T(k_y \rho_i) \quad (86)$$

where once again we have isolated the essential physical parameters, and introduced a dimensionless function $T(k_y \rho_i)$, such that $T(1) \approx 1$, and

$T(k_y \rho_i) \rightarrow 0$ as $k_y \rho_i \rightarrow \infty$. We also introduce a low-wavenumber cut-off for the turbulent spectrum, by excluding from the contributions to the diffusion coefficient those wavenumbers with:

$$k_y \rho_i < \beta \quad (87)$$

where, say, $\beta \approx 1/2$. Introducing (85) into Eq.(84), we obtain:

$$D_x^{turb} = \frac{1}{l_y} \sum_{k_y \rho_i > \beta} k_y^2 < |\phi(k_y)|^2 > \tau_c(k_y) \quad (88)$$

Using the various normalizations (78,79,80), we obtain:

$$D_x^{turb} = c_0 \frac{T_i}{eB} \quad (89)$$

where c_0 is the dimensionless constant defined by the expression:

$$c_0 = \left(\frac{c_2 c_3}{c_1} \right)^2 \frac{1}{\pi} \int_{\beta}^{\infty} dK K^2 A(K) T(K) \quad (90)$$

Taking $c_1 \approx 40$, $c_2 \approx 5$ and $c_3 \approx 2$, and assuming the integral to be of order 1, we find an estimate for c_0 :

$$c_0 \approx 0.02 \quad (91)$$

a value somewhat smaller than implied by Eq.(74), but of the right order of magnitude.

Eq.(90), which predicts a Bohm-type of diffusion, is also consistent with the general result of Taylor and McNamara[43], who found that in two-dimensions, $\mathbf{E} \times \mathbf{B}$ transport will always lead to a $1/B$ scaling of the diffusion coefficient. Our assumption that the edge turbulence is density-independent must then result in a diffusion coefficient which, dimensionally, can only have a Bohm-like dependence on B and T_i .

For the specific case of Run 1, we can estimate the diffusion coefficient from the discrete sum of Eq.(84). Assuming that $\beta = 0.5$, $\tau_c(k_y) = \omega_{ci}^{-1}$, and using the numerical values of the spectra as obtained in Fig.(19), we find the estimate:

$$D_x^{turb} = 0.04 \quad (92)$$

a very rough estimate, which nonetheless is in accordance with the numerical value obtained in Eq.(74). We shall now consider the density dependence of the diffusion coefficient, as measured in our numerical simulations, thereby qualifying the range of validity of Eq.(89), which assumes density-independence.

7.6 Scaling of the Diffusion Coefficient with Density

We shall now consider the effect of particle density on the diffusion coefficient, as measured in the numerical simulations. We performed a series of numerical simulations which were variations of Run 1 (but in a smaller system, with $L_y = 128$), over which we studied the effect of varying the final ω_{pi}/ω_{ci} ratio. We achieved this by varying the creation rate s (the rate of creation of electron-ion pairs per time step) over the range $0.157 \leq s \leq 5.02$, which resulted in a range of average steady-state densities such that $0.63 \leq \omega_{pi}^2/\omega_{ci}^2 \leq 8.07$. We then estimated the diffusion coefficient using Eq.(74):

$$D_x = \frac{\sigma L_x^2}{2n(L_x)} \quad (93)$$

where $\sigma = s/L_x L_y$ is the injection rate per unit area. The results are shown in Fig.(28), where we plot D_x against $\omega_{pi}^2/\omega_{ci}^2$. The figure indicates that at lower densities, in the range $\omega_{pi}^2/\omega_{ci}^2 \leq 3$, the diffusion coefficient has an approximately linear dependence on the density. At higher densities, with $\omega_{pi}^2/\omega_{ci}^2 > 3$, the diffusion coefficient levels off, and assumes what appears to be a density independent value of:

$$D_x = 0.04 \frac{T_i}{eB} \quad (94)$$

The density-independence of the diffusion coefficient is consistent with the derivation of the previous section, where we argued that provided $\omega_{pi}^2/\omega_{ci}^2 \gg 1$, the diffusion coefficient should be density independent.

In the simulations leading to Fig.(28), we were able to explore only a limited range of densities, amounting to an order of magnitude. This limitation occurred because we desired to keep $\omega_{pe}^2/\omega_{ce}^2 < 1$, while running the simulation with the small numerical mass ratio $m_i/m_e = 40$. To reach higher steady-state densities, while maintaining $\omega_{pe}^2/\omega_{ce}^2 < 1$, would have

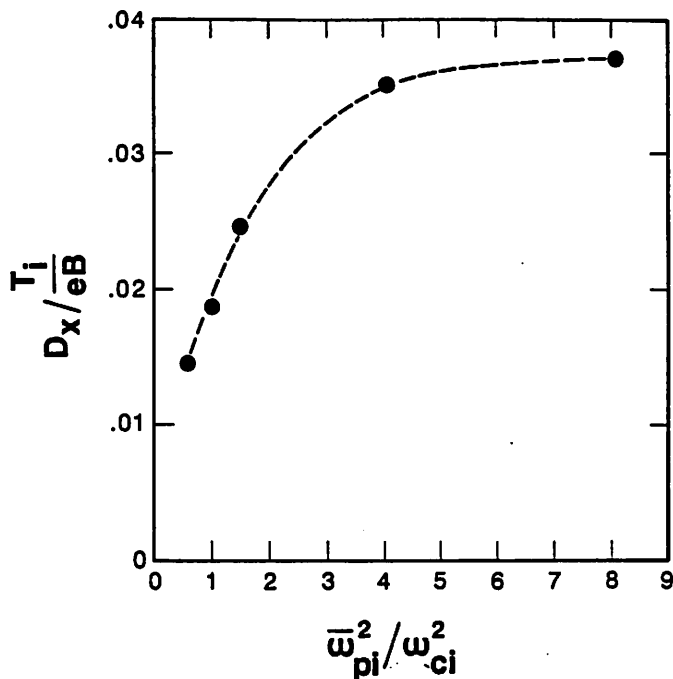


Figure 28: Dependence of the diffusion coefficient on the steady-state density.

required using larger mass ratios, and, with the explicit scheme used in ES2, would have resulted in prohibitively long computer runs. As noted in Section 7.2, these limitations should be overcome in a future modification of ES2, incorporating an electron $\mathbf{E} \times \mathbf{B}$ mover.

Notwithstanding the limitations in the range of densities explored, we expect that the levelling-off of the diffusion coefficient with larger densities reflects a general trend, and should be applicable at considerably higher densities, for instance in a fusion environment, where one might have $\omega_{pi}^2 / \omega_{ci}^2$ as large as 10^3 .

We should also note that while the diffusion coefficient appears to be rather insensitive to the steady-state density, the nature of the edge turbulence does appear to be modified by the larger injection rates. In Figs.(29), we compare potentials for two different injection rates, which result in steady-state densities such that $\omega_{pi} / \omega_{ci} = 2.1$ and $\omega_{pi} / \omega_{ci} = 2.8$. The qualitative difference in these plots suggests that for $\omega_{pi} / \omega_{ci} > 2$ there occurs a transition to a more turbulent regime, in which the long-lived vortices seen in Run 1, $\omega_{pi} / \omega_{ci} = 1.3$, are replaced by less stable structures.

Finally, we should emphasize that the diffusion coefficient of Eq.(89) is an average for diffusion in the sheath, and is meant to be nonzero only in a

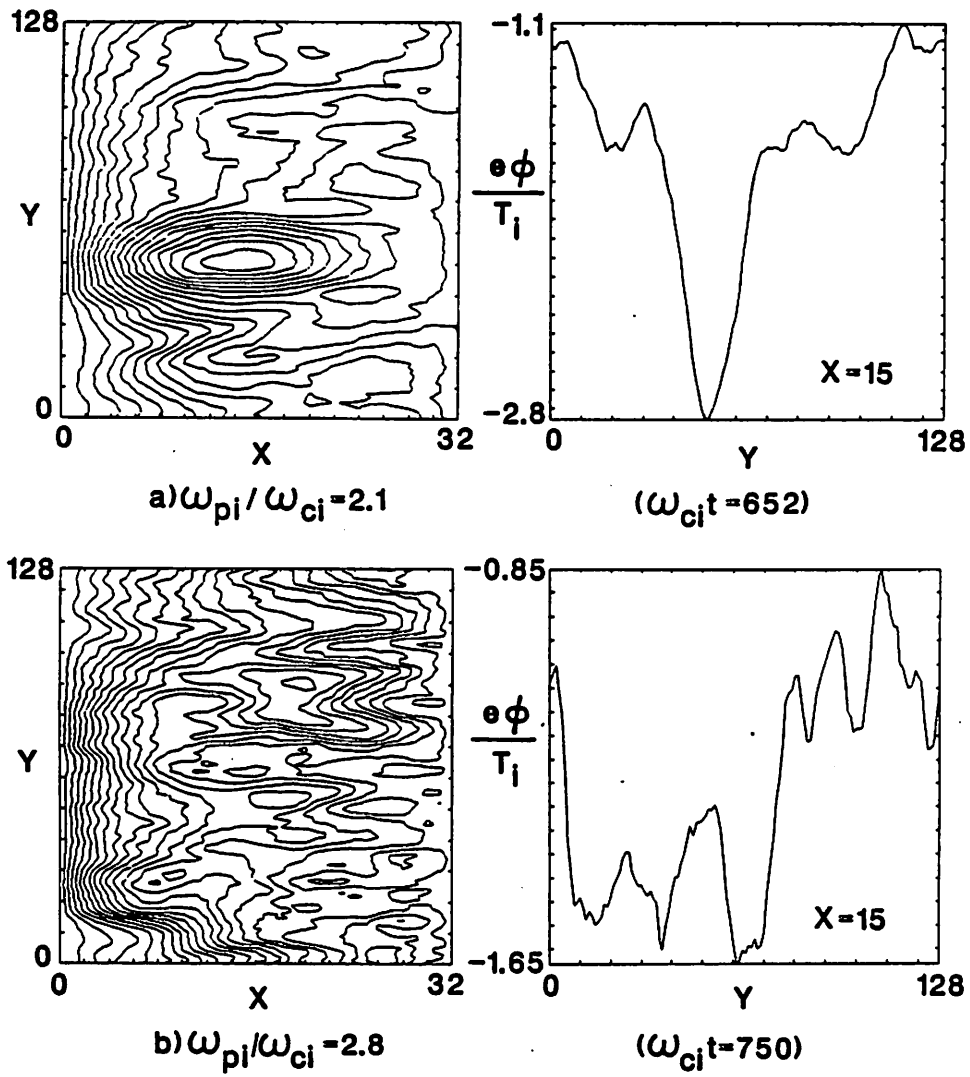


Figure 29: Effect of higher densities on the potential structures in the edge turbulence.

layer of thickness of order $l_x \sim 5\rho_i$. Beyond this boundary layer, transport is predominantly collisional. Thus, in order to solve for the density profile in a system with $L_x \gg l_x$, we should write $D_x(x) = D_x^{turb} + D_x^{coll}$, where the diffusion coefficients are given, respectively, in Eqs.(89) and (76), and then solve the diffusion equation (72), with appropriate boundary conditions ($n(x=0) = 0$ and $\partial n(x=L_x)/\partial x = 0$).

What is the actual particle flux to the wall induced by the sheath? Assuming an edge density n_0 , we can estimate the flux Γ_x through:

$$\Gamma_x \approx D_x^{turb} n_0 / l_x \quad (95)$$

where D_x^{turb} is given in Eq.(94) and $l_x \approx 5\rho_i$ is the sheath thickness, which establishes the edge density gradient. We find (for $\omega_{pi} \geq 2\omega_{ci}$):

$$\Gamma_x = 10^{-2} v_{ti} n_0, \quad (96)$$

Of course, in the steady-state, the outward flux predicted by Eq.(96) must be matched by a collisional or turbulent flux from the inner regions of the plasma. Eq.(96) then provides a boundary condition for the analysis of transport in the interior of the plasma.

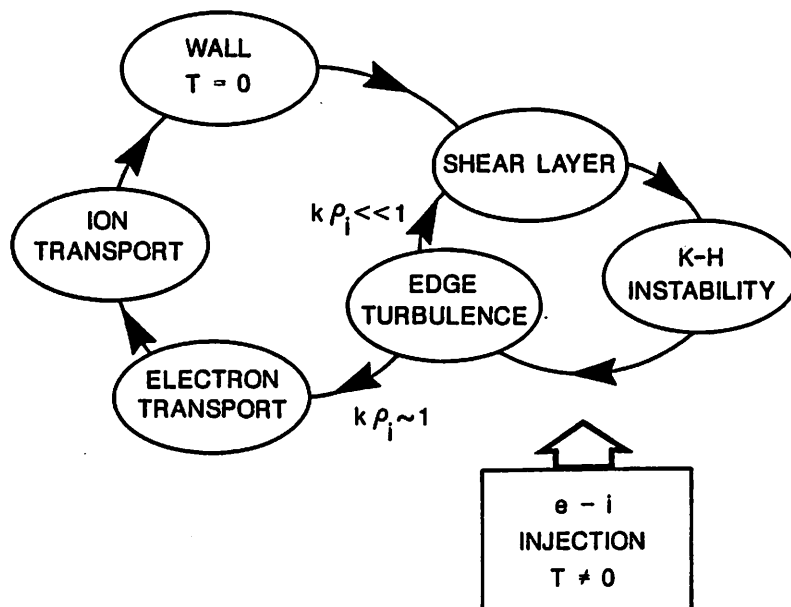


Figure 30: Global scenario for steady-state turbulence and transport in the sheath.

8 Summary

In Fig.(30), we have summarized the interacting mechanisms which according to our scenario, drive the turbulent, steady-state cross-field sheath. The scenario proceeds as follows. The presence of the wall imposes the formation of the initial edge shear layer, which is unstable to the Kelvin-Helmholtz instability. This instability is in turn the source of the edge turbulence, which after a transient phase, reaches a steady-state. In this new, dynamic equilibrium, the long-wavelength components of the turbulence, the vortices, modify the edge conditions, by broadening the edge layer, and by maintaining large-amplitude, drifting potential structures. Furthermore, the short-wavelength components of the turbulence create a cross-field transport, by diffusing the electrons out of the system. As a result, an ambipolar, outward flux of electrons and ions is set in motion, with a diffusion coefficient which scales as the Bohm diffusion coefficient.

Thus, with a constant injection of electron-ion pairs, the system maintains a steady-state, in which the linear edge instability, the nonlinear dynamics of the turbulence, and the outward particle diffusion all balance each other.

Our principal results can be summarized as follows:

1. The y -uniform cross-field sheath is linearly unstable to the Kelvin-Helmholtz instability, with growth rates predicted by fluid theory in the range $|k_y|\rho_i \ll 1$.
2. The turbulent cross-field sheath has an equilibrium thickness of order $l_x \sim 5\rho_i$.
3. The edge turbulence principally consists of large-amplitude vortices, with $|\delta\phi| \sim 3T_i/e$, and with a spacing of at least $l_y \sim 40\rho_i$.
4. The drift velocity of the vortices parallel to the wall is of order $v_{ti}/2$, leading to a turbulent spectrum with dispersion relation at small wavenumbers $|\omega| \approx |k_y| v_{ti}/2$.
5. The edge spectrum extends in wavenumber to $|k|\rho_i \approx 1$, beyond which it rapidly decreases; the shorter-wavelength components have a broad spectrum in frequency, with maximum width $|\delta\omega| \sim \omega_{ci}$.
6. Transport in the sheath is Bohm-like, and is consistent with a model in which the electrons are driven-out by the short-wavelength turbulence, with a subsequent, ambipolar diffusion of the ions. An estimate of the diffusion coefficient is:

$$D_x^{turb} = 0.04 \frac{T_i}{eB}, \quad \omega_{pi} \geq 2\omega_{ci} \quad (97)$$

At lower edge densities, such that $\omega_{pi} < 2\omega_{ci}$, the expression for the diffusion coefficient has an additional factor, which is approximately proportional to the density.

7. For a given edge density n_0 , the sheath induces a particle flux to the wall which is of order:

$$\Gamma_x = 10^{-2} v_{ti} n_0, \quad \omega_{pi} \geq 2\omega_{ci} \quad (98)$$

Finally, let us say a few words regarding similarities and differences between our model and that of Horton et al.[16]. In [16], an implicit particle code is used to explore the evolution of an initially symmetric velocity shear layer. The evolution of the Kelvin-Helmholtz instability in this configuration is similar to that which we found for the cross-field sheath: the instability grows, saturates into large-amplitude vortices, which then undergo multiple coalescence, and finally merge into one large vortex. There are nonetheless basic differences between the model of [16] and our model:

1. In our model, the primary concern is plasma-wall interaction; in ES2 the boundary is fully absorbing, while the boundaries in [16] are purely reflecting, and are placed far from the shear layer.
2. Because of the presence of the wall, the cross-field sheath and its vortices form in a completely spontaneous and self-consistent manner. On the other hand, the model of [16] requires an external electric field in order to initiate the shear layer.
3. There is a basic difference in space and time scales. Horton et al. consider a shear layer with width $a \gg \rho_i$, and their implicit particle code is intrinsically limited to low frequencies, $\omega \ll \omega_{ci}$. On the other hand, our model includes much shorter space and time scales: the sheath develops a thickness of a few gyro-radii across, and the turbulence extends to frequencies with $\omega \approx \omega_{ci}$.
4. In our model, the cross-field sheath exhibits strong density variations, whereas [16] considers a shear layer with a constant density.

Thus, despite overlap with our model, especially as regards the fluid evolution of the Kelvin-Helmholtz instability, the model of [16] nonetheless applies to a very different range of physical parameters.

9 Conclusions

Our numerical simulations have shown that the cross-field sheath between a wall and a plasma is not a static structure, but is in fact a turbulent boundary layer, with strong potential fluctuations and anomalous particle transport. The driving mechanism for this turbulence is the Kelvin-Helmholtz instability which arises from the sheared particle drifts created near the wall by the strongly nonneutral sheath. Provided it is replenished by an internal flux of particles, coming for instance from a central bulk plasma or from a diffuse ionization of neutrals, the sheath will maintain itself in a dynamic equilibrium, in which the linear edge instability, the nonlinear dynamics of the particles and the outward particle diffusion all balance each other. It is important to emphasize that the turbulent behavior of the sheath is a completely spontaneous phenomenon, which arises from the plasma-wall interaction, and which does not require the imposition of external fields for its sustenance.

We have found that the cross-field sheath assumes an equilibrium thickness of order $l_x \sim 5 \rho_i$, and that it maintains large vortices, with amplitudes $\delta\phi \sim T_i/e$, which drift parallel to the wall at roughly half the ion thermal velocity. The sheath also maintains a large, spatially-averaged potential drop from the wall to the plasma, with $\Delta\phi \approx -1.5T_i/e$, in sharp distinction with the unmagnetized sheath, where the plasma potential is *higher* than at the wall. The average velocity shear profile remains linearly unstable at all times, a feature which shows that the saturation mechanism is not quasilinear (relaxation of the space-averaged shear profile), but strongly nonlinear.

A central result of this paper is that the sheath induces an anomalous transport of particles, which is due to short-wavelength turbulence, and which scales very much like Bohm diffusion, at least when $\omega_{pi} \geq 2\omega_{ci}$. At lower densities, such that $\omega_{pi} < 2\omega_{ci}$, the diffusion coefficient is found to have an additional factor, proportional to the density. These results enable us to model the entire cross-field sheath by a simple boundary condition, which relates the particle flux through the sheath to the edge density. This boundary condition, which simply measures the sheath's "impedance" to particle flow, should be very valuable as input in any model designed to obtain the bulk plasma properties, and in which the detailed sheath dynamics are unimportant.

We believe that future numerical simulations of the cross-field sheath should explore a larger range of parameters, in system size and in density, than were feasible in the present work, in order to verify the scaling laws that we found to be valid for a more limited range of parameters. For instance, we were limited to systems in which a single vortex survived in the steady-state, while we believe that longer systems should be able to accommodate many vortices. Similarly, we were limited to exploring a range of plasma densities such that $\omega_{pi}^2/\omega_{ci}^2 < 10$, while we would like to explore values as high as $\omega_{pi}^2/\omega_{ci}^2 = 10^3$, representative of a fusion environment. A relatively straightforward modification of our simulation code ES2, to allow for an $\mathbf{E} \times \mathbf{B}$ electron mover, should make all of these extended studies feasible at a reasonable cost in computer time.

Other avenues of research on cross-field dynamics might involve studying the behavior of a free plasma boundary, far from the wall, in order to observe the relaxation of the edge layer. A central question here is whether the Kelvin-Helmholtz turbulence can induce transport over very many ion gyro-radii, or whether it is limited to a “natural” boundary layer, of thickness comparable to the plasma wall sheath, that is roughly $l_x \sim 5\rho_i$. Let us also note that in connection with active plasma devices, one might study the behavior of the cross-field sheath when an external electrostatic potential is applied: the resulting dynamics should bear much resemblance to those of the one-species magnetron, but with the distinct physics of a two-species plasma. Finally, we note that our simulation results also raise more fundamental questions regarding the nature of the edge turbulence, which was only partially explained by the fluid theory. This suggests further analytical research, applying a fully kinetic treatment to the problem, with perhaps specially designed simulations to verify, for instance, vortex stability and the mechanisms for generating short-wavelength fluctuations.

Acknowledgments

The author wishes to thank Prof.C.K.Birdsall for his contributions to this research, through various discussions, and especially for initiating this work, by suggesting the possibility of the Kelvin-Helmholtz instability in the two-dimensional, cross-field sheath. The author also wishes to thank Dr.Liu Chen for many detailed and stimulating exchanges, and Dr.M.J.Gerver and Prof.A.J.Lichtenberg for various illuminating discussions. Finally, thanks go to Mr.O.Garcia of the Electronics Research Laboratory, for his assistance with the graphical work. This research was supported by U.S. Department of Energy Contract No.FG03-86ER53220, by U.S. Office of Naval Research Contract No. N14-80-C-0507 and by a MICRO grant with a gift from the Varian Corporation.

Appendix

A The One-Dimensional Sheath

In this appendix, we study the structure of the sheath when the geometry is restricted to a single spatial dimension, the perpendicular distance from the wall. This analysis is conceived as an initial value problem: we consider the sheath that forms from the scrape-off of particles in an initially uniform plasma, which is put into contact with the wall at some $t = 0$. The result, for $t \gg 2\pi/\omega_{ci}$, is a static sheath which extends some distance ρ_i into the plasma. In our discussion of this initial-value problem, we omit treating the effects of collisionality and of a distributed source of particles, even though it is only in the presence of these processes that the one-dimensional sheath can maintain a steady-state transport to the wall. Such an analysis has been undertaken by several authors[44,45]. In the present Section, our goal is less ambitious. We consider the formation of the one-dimensional sheath as a transient prelude to two-dimensional behavior, and as such restrict our analysis to the initial sheath formation. The results of our study make analytically plausible the values of y -uniform edge potential drop and of the shear layer which almost instantaneously appear in the two-dimensional simulations.

A.1 Analytic Expressions for the Electric Field

We should stress that the analysis in this Section is semi-quantitative. This is because, despite the apparent simplicity of the formulation of the initial-value problem, we have not been able to obtain a fully self-consistent solution for the formation and structure of the cross-field sheath. This difficulty is linked to the multi-dimensional nature of the problem, where we have to solve for the time-evolution of a distribution function $f(x, v_x, v_y, t)$ which is three-dimensional in phase space. Furthermore, the wall boundary condition is such that if f is Maxwellian far from the wall, it is nonetheless strongly non-Maxwellian in the edge layer, and thus a perturbation approach is not feasible. Another complication arises because the sheath thickness is of the same order as the gyroradius, and this implies that f has a strong dependence on all of its independent variables (f varies a length

scale of order ρ_i , over a velocity scale v_{ti} and over a time-scale ω_{ci}^{-1}). In short, there is no small parameter to facilitate an analytic solution, except, as we shall see, for the ratio ω_{ci}/ω_{pi} , which can be considered small in a fusion environment. Paradoxically, some aspects of the two-dimensional behavior of the sheath are more amenable to analysis than in the one-dimensional configuration.

In what follows, we shall assume that the electron gyro-radius is negligible and take $\rho_e \rightarrow 0$. Thus, the electrons are "frozen" onto the magnetic field lines, and their density remains constant in space and time. With this approximation, we need to consider only the evolution of the ion distribution function, $f_i(x, v_x, v_y, t)$, in the presence of a self-consistent electric field $E_x(x, t)$, taking into account the loss of ions by impact to the wall. Furthermore, we shall consider only the time-asymptotic state of the sheath, when $t \gg 2\pi/\omega_{ci}$.

With the wall at $x = 0$, we assume an initially uniform and Maxwellian ion distribution function:

$$f_i(x, v_x, v_y, t = 0) \equiv \frac{1}{2\pi v_{ti}^2} e^{-(v_x^2 + v_y^2)/2v_{ti}^2}, \quad 0 \leq x < \infty, \quad (99)$$

To bring out the essential dependencies in the problem, we normalize all variables according to:

$$t' = \omega_{ci} t \quad x' = x/\rho_i, \quad (100)$$

$$f' = v_{ti}^2 f_i \quad E' = E_x/B_0 v_{ti}, \quad (101)$$

where $\rho_i = v_{ti}/\omega_{ci}$ is the ion gyro-radius. With these normalizations, the Vlasov-Poisson system can be written (dropping the primes for convenience):

$$\frac{\partial f}{\partial t} + v_x \frac{\partial f}{\partial x} + [E(x, t) + v_y] \frac{\partial f}{\partial v_x} - v_x \frac{\partial f}{\partial v_y} = 0 \quad (102)$$

$$\frac{\partial E}{\partial x} = Q \left(\int f(x, v_x, v_y, t) dv_x dv_y - 1 \right), \quad (103)$$

with the initial condition, $f(x, v_x, v_y, 0) = \exp[-(v_x^2 + v_y^2)/2]/2\pi$. The system of Eqs.(102,103) is to be solved for $0 \leq x < \infty$. In Eq.(103), we

have defined $Q \equiv \omega_{pi}^2/\omega_{ci}^2$ where ω_{pi} is the plasma frequency of the uniform plasma far from the wall. The parameter Q is the only remaining independent parameter in the problem, which now consists in finding $f(x, v_x, v_y, t)$ and $E(x, t)$ for $t \rightarrow \infty$, as a function of Q . For fusion applications, we have $Q \gg 1$, and this will afford some simplifications in our analysis of the sheath structure.

Despite their apparent simplicity, Eqs.(102,103) have no obvious analytic solutions. This has led us to resort to a semi-qualitative approach in solving them. Our basic assumption is to make what might be termed a "local" approximation, in which the ion density at any one point is an explicit function of the electric field evaluated at the same point. We first assume that at any distance x , the ion density can be calculated by assuming that the electric field at that point has been constant in both space and time since $t = 0$. With a constant electric field, an ion initially at a distance x and with velocity (v_x, v_y) will not collide with the wall provided that its velocity lies in the region:

$$v_y \geq -E + \frac{1}{2x}(v_x^2 - x^2) \equiv g(x, v_x), \quad (104)$$

We shall now approximate the local "free" ion density by an integral which removes all particles which are not in the region specified by (104):

$$n_F(E, x) = \int_{v_y \geq g(x, v_x)} f_M(x, v_x, v_y) dv_x dv_y, \quad (105)$$

Eq.(105) does not embody consistent approximations, and in fact assumes two opposite physical limits, one for the ions which have impacted into the wall, and another for the "free" ions which have remained in the plasma. For the unconfined ions, finite orbit effects are implicitly taken into account by assuming that they have indeed impacted into the wall, and thus must be removed from the integration in Eq.(105). On the other hand, we have neglected finite orbit effects for the confined ions, because in Eq.(105) we take the integrand to be the initial Maxwellian, without considering the mixing of contributions from different areas of phase space, as would be required in a calculation using the full ion orbits. Despite these simplifications, we believe that the spirit of the calculation is correct, in that it should bring out the proper space scales and field amplitudes.

Using Eq.(109), one obtains an expression for the local free ion density:

$$n_F = \frac{1}{(2\pi)^{1/2}} \int_{-E-x/2}^{\infty} dv_y e^{-v_y^2/2} \text{erf} \left[(x(E + v_y) + x^2/2)^{1/2} \right] \quad (106)$$

where “erf” denotes the error function. For the analysis that follows, Eq.(106) is a rather untractable expression for n_F , and, in the spirit of the previous approximations, we shall greatly simplify this equation. We first make the hypothesis that the fields in the sheath are such that we can everywhere assume that either $E \gg 1$ (near the wall, with $x < 1$), or that $x \gg 1$ (in the tail of the sheath, where $E < 1$). We deliberately neglect the transition region, where $E \sim 1$ and $x \sim 1$, hoping that the essential behavior comes from the asymptotic regions near and far from the wall. As we shall see, these approximations are plausible provided $Q = \omega_{pi}^2/\omega_{ci}^2 \gg 1$.

With the simplifying assumptions of the previous paragraph, we can uniformly neglect the v_y -dependence in the argument for the error function, and furthermore, we set the lower limit of the integral in Eq.(106) to $-\infty$. The result of these simplifications is:

$$n_F = \text{erf} \left[(xE + x^2/2)^{1/2} \right] \quad (107)$$

We now impose another sweeping approximation, by replacing the error function in Eq.(107) by the expression:

$$\text{erf}(z) \sim 1 - e^{-z^2}, \quad (108)$$

an approximation which incorporates the vanishing of the error function at $z = 0$ (albeit with the wrong dependence on z), and the correct exponential dependence for $z \rightarrow \infty$.

Given $n_F(E, x)$ as defined by Eq.(105), we then introduce it into Poisson's equation:

$$\frac{dE}{dx} = Q(n_F - 1), \quad (109)$$

Using (108) in Eq.(107), and introducing the resulting n_F into Poisson's equation, we obtain:

$$\frac{dE}{dx} = Q \exp \left(-(xE + x^2/2) \right) \quad (110)$$

This equation is to be solved with the sole boundary condition that $E(x)$ vanishes for large x , a condition which uniquely determines the solution with Q as a parameter. In particular, Eq.(110) uniquely determines the value of the electric field at the wall, $E(0)$ as a function of Q .

Despite all our manipulations, Eq.(16) is not yet analytically solvable. However, one can extract important information on the nature of the sheath by examining the scaling of the variables on Q . Let us write $\xi = Q^{1/2}x$ and $\hat{E} = E/Q^{1/2}$. We then have:

$$\frac{d\hat{E}}{d\xi} = \exp(-(\xi\hat{E} + \xi^2/2Q)) \quad (111)$$

We now see that if we have $Q \gg 1$, there exists an edge layer extending to some $\xi \sim 1$ where Eq.(111) is independent of Q , and has the form:

$$\frac{d\hat{E}}{d\xi} = \exp(-\xi\hat{E}) \quad (112)$$

In physical units, this edge region extends to $x \approx \rho_i/Q^{1/2} = \lambda_{di}$, and the electric field has an amplitude $E_x \sim Q^{1/2}v_{ti} = (\omega_{pi}/\omega_{ci})v_{ti} \gg v_{ti}$. With the requirement that the electric field vanishes far from the wall, we can roughly estimate $\hat{E}(0)$ from Eq.(112) by assuming that in the right-hand side of the equation, we can take the electric field to be constant and equal to its value right at the wall. Integrating from 0 to ∞ , we then have the identity:

$$\hat{E}(0) = \int_0^\infty e^{-\xi\hat{E}(0)} d\xi \quad (113)$$

which immediately yields $\hat{E}(0) = 1$. In physical units:

$$E_x(0) \sim B_0 v_{ti} \frac{\omega_{pi}}{\omega_{ci}}, \quad (114)$$

The solution of Eq.(111) must be connected to the ‘‘outer solution’’ of Eq.(112), in the region $\xi \geq 1$. The scaling of Eq.(111) breaks-down when $\hat{E}(\xi)$ becomes so small that it becomes comparable to the second term in the exponential in Eq.(111). This occurs when $x \sim 1$ and $\hat{E} \sim 1/Q$, or in physical units, we have $E_x(\lambda_{di}) \sim B_0 v_{ti}$. Beyond this point, Eq.(16) predicts the decay of the electric over a length comparable to the gyro-radius ρ_i .

To summarize the results of our approximations, we have found that with $\omega_{pi}/\omega_{ci} > 1$, Poisson's equation predicts the existence of a "composite" sheath, with an inner and an outer layer. There is a first region, an "inner sheath", extending up to a Debye length λ_{di} , for which the peak electric field was given by Eq.(114), $E_x \sim B_0 v_{ti} (\omega_{pi}/\omega_{ci})$. Beyond this inner sheath, there is a boundary layer extending to roughly a gyro-radius ρ_i from the wall, with a peak electric field of order $E_x \sim B_0 v_{ti}$.

A.2 Comparison with one-dimensional particle simulations

We now briefly compare the analytic results of the previous Section with those of one-dimensional particle simulations. In Fig.(31a,b), we show the electric fields obtained one-dimensional particle-in-cell simulations of the cross-field sheath, for $\omega_{pi}/\omega_{ci} = 1.9$ and 6.3. In effect, the simulation algorithm exactly solves Eq.(102), to within the bounds imposed by the thermal noise induced by the finite particles. In Figs.(31a,b), we can see that the strict division of the sheath into inner and outer layers, as was implied by the considerations of the previous subsection, is not observed in the simulation electric fields $E_x(x)$. On the other hand, the overall sheath is indeed an ion gyro-radius in thickness. Furthermore, we have found that the scaling for the peak electric field at the wall does obey Eq.(??) remarkably well, whenever we have $\omega_{pi}/\omega_{ci} > 1$. This can be seen in Fig.(32), where we plot the value of the electric field at the wall as a function of the parameter ω_{pi}/ω_{ci} . Note that for $\omega_{pi}/\omega_{ci} < 1$, the electric field appears to scale as $E_x(0)/B_0 v_{ti} \sim \omega_{pi}^2/\omega_{ci}^2$.

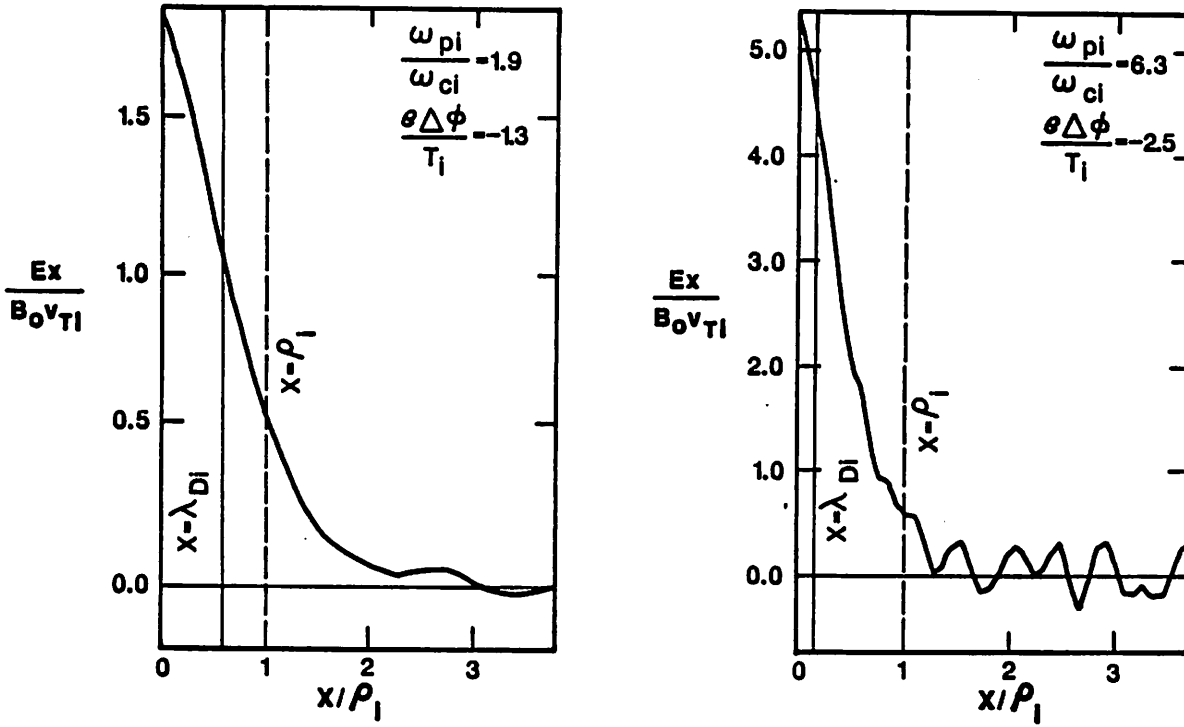


Figure 31: Profiles of the cross-field sheath in one-dimensional simulations.

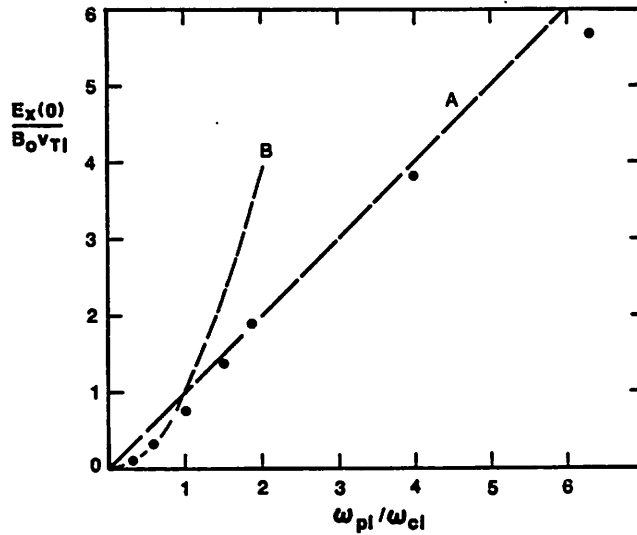


Figure 32: Scaling with density of the electric field at the wall in a one-dimensional simulation (full dots). Line A denotes the dependence ω_{pi}/ω_{ci} , line B the dependence $\omega_{pi}^2/\omega_{ci}^2$.

References

- [1] K. Theilhaber, "ES2 User's Manual - Version 1", Memorandum No. UCB/ERL M87/23, Electronics Research Laboratory, College of Engineering, University of California at Berkeley, May 11 1987.
- [2] G. Nicolis, I. Prigogine, *Self-Organization in Nonequilibrium Systems*, Wiley-Interscience, New York, 1977.
- [3] H.J. Kreuzer, *Nonequilibrium Thermodynamics and its Statistical Foundations*, Clarendon Press, Oxford, 1981; Chapter 6.
- [4] K. Theilhaber, Bull. of the A. P. S., **32**, 9, October 1987, 8I6.
- [5] K. Theilhaber, "Movie Script: Dynamics of a cross-field sheath", Plasma Theory and Simulation Group, Electronics Research Laboratory, U. of California, Berkeley, Feb 10 1987.
- [6] I. Langmuir, "The interaction of electron and positive ion space charges in cathode sheaths", Phys. Rev. **33**, June 1929, 954.
- [7] U. Delbelge, B. Bein, "Electric sheath between a metal surface and a magnetized plasma", Phys. Fluids **24** 1190 (1981).
- [8] R. Chodura, "Plasma-wall transition in an oblique magnetic field", Phys. Fluids **25** (9) 1982, 1628.
- [9] O. Buneman, C.V.D. Report Mag. **37** (1944); and J. Electronics, **3**, 1 (1957).
- [10] R. W. Gould, "Space-charge effects in beam-type magnetrons", J. of Applied Physics, **28**, 5 (1957).
- [11] W. Knauer, "Diocotron instabilities in plasmas and gas discharges", J. of Applied Physics, **37**, 2 (1966).
- [12] S. Chandrasekhar, *Hydrodynamic and Hydromagnetic Stability*, Oxford, at the Clarendon Press, 1961; Chapter 11.
- [13] J.A. Byers, Phys. Fluids, **9**, 1038 (1966).

- [14] A. Miura and P.L. Pritchett, *J. of Geo. Res.*, **87**, A9, 7431 (1982).
- [15] P.L. Pritchett and F.V. Coroniti, *J. of Geo. Res.*, **89**, A1, 168 (1984).
- [16] W. Horton, T. Tajima, T. Kamimura, *Phys. Fluids*, **30**, 11, Nov. 1987, 3485.
- [17] C.K. Birdsall, A.B. Langdon, *Plasma Physics via Computer Simulation*, McGraw Hill, 1985, page 308.
- [18] *Idem*, page 322.
- [19] R.B. White, "Resistive reconnection", *Rev. of Mod. Phys.*, **58**, No. 1, Jan 1986, 183.
- [20] G.M. Corcos, F.S. Sherman, "Vorticity concentration and the dynamics of unstable free shear layers", *J. Fluid Mech.* **73**, part 2 (1976) 241.
- [21] G.M. Corcos, F.S. Sherman, "The mixing layer: deterministic models of a turbulent flow. Part 1: introduction and the two-dimensional flow", *J. Fluid Mech.* **139** (1984) 29.
- [22] P.C. Patnaik, F.S. Sherman, G.M. Corcos, "A numerical simulation of Kelvin-Helmholtz waves of finite amplitudes", *J. Fluid Mech.* **73**, part 2 (1976) 215.
- [23] H. Lamb, *Hydrodynamics*, Dover, New York, 1945.
- [24] R.T. Pierrehumbert, S.E. Widnall, "The two and three-dimensional instabilities of a spatially periodic shear layer", *J. Fluid Mech.* **114** (1982) 59.
- [25] R.Z. Sagdeev, V.D. Shapiro, V.I. Shevchenko, "The Great Red Spot as a synoptic vortex in the Jovian atmosphere", *Sov. Astron. Lett.* **7**, Jul-Aug 1981, p. 279.
- [26] T.H. Dupree, "Theory of two-dimensional turbulence", *Phys. Fluids*, **17**, 1 (1974) 100.

- [27] W. Horton, J. Liu, J.D. Meiss, J.E. Sedlak, "Solitary vortices in a rotating plasma", *Phys. Fluids* **29** (4), April 1986, 1004.
- [28] Baron Rayleigh (J.W. Strutt), *Scientific Papers*, vol. 1, Cambridge University Press, 1899; see Chap. 66, "On the stability, or instability, of certain fluid motions".
- [29] S. Chandrasekhar, *Hydrodynamic and Hydromagnetic Stability*, Oxford, at the Clarendon Press, 1961, p. 494.
- [30] J.D. Meiss, W. Horton, "Solitary drift waves in the presence of magnetic shear", *Phys. Fluids* **26** (4), April 1983, 990.
- [31] G.K. Batchelor, *An Introduction to Fluid Dynamics*, Cambridge University Press, 1974, p.536.
- [32] H. Lamb, *Idem*; see Chap. VII on vortices, p. 246 for the derivation of doublet vortices.
- [33] G.M. Jenkins, D.G. Watts, *Spectral Analysis and its Applications*, Holden-Day, 1969, p.243.
- [34] C.K. Birdsall, A.B. Langdon, *Plasma Physics via Computer Simulation*, McGraw Hill, 1985, page 261.
- [35] W.L. Kruer, J.M. Dawson, "Sideband instability", *Phys. Fluids*, **13**, 11, Nov. 1970, 2747.
- [36] R.A. Smith, J.A. Krommes, W.W. Lee, "Saturation of drift instabilities by electron dynamics", *Phys. Fluids*, **28**, 4, April 1985.
- [37] C.F.F. Karney, "Stochastic ion heating by a lower hybrid wave", *Phys. Fluids* **21**, 9, Sep. 1978, 1585.
- [38] D.C. Barnes, T. Kamimura, "Implicit particle simulations of magnetized plasmas", Eq.(9), *J. Comp. Phys.*, **52**, 1983, 480.
- [39] A.J. Lichtenberg, M.A. Lieberman, *Regular and Stochastic Motion*, Springer-Verlag, 1983, p.45.

- [40] N.A. Krall, A.W. Trivelpiece, *Principles of Plasma Physics*, McGraw-Hill, 1973, p.21.
- [41] H. Okuda, J.M. Dawson, "Theory and numerical simulation of plasma diffusion across a magnetic field", *Phys. of Fluids*, **16**, 3 (1973) 408.
- [42] J.M. Dawson, H. Okuda, R.N. Carlile, "Numerical simulation of plasma diffusion across a magnetic field in two dimensions", *Phys. Rev. Letters*, **27**, 8 (1971) 491.
- [43] J.B. Taylor, B. McNamara, "Plasma diffusion in 2 dimensions", *Phys. Fluids*, **14**, 2 (1971) 1492.
- [44] D. Holland and B. D. Fried, "Cross-field sheath in a magnetized plasma", *Bull. of the A. P. S.*, **32**, 9, October 1987, Poster 9P12.
- [45] R. Gerwin, "The magnetized anode sheath", *Bulletin of the American Physical Society*, **32**, 9, October 1987, Poster 9P13.